Stanford-HEP-98-03
Tohoku-RCNS-98-15

KamLAND

a Liquid scintillator Anti-Neutrino Detector at the Kamioka site.

July 1998

P. Alivisatos[2], S. Berridge[13], N. Bokor[12], C. Britton[9], W. Bryan[9], W. Bugg[13], J. Busenitz[1], T. Chikamatsu[6], H. Cohn[13], L. DeBraeckeleer[4], B. Dieterle[7], Yu. Efremenko[13,9], S. Enomoto[14], K. Furuno[14], S. Frank[9], C.R. Gould[8], G. Gratta[11], H. Hanada[14], E. Hart[13], S. Hatakeyama[14], G. Horton-Smith[11], T. Itoh[14], T. Iwamoto[14], Yu. Kamyshkov[13,9], S. Kawakami[14], M. Koga[14], J. Kornis[12], K.B. Lee[3], H.L. Liew[11], K. Mashiko[14], L. Miller[11], M. Nakajima[14], T. Nakajima[14], A. Nemeth[12], V. Novikov[3], H. Ogawa[14], K. Oki[14], P. Pacher[12], A. Piepke[3], S. Riley[7], N. Sleep[10], J. Shirai[14], F. Suekane[14], A. Suzuki[14], O. Tajima[14], K. Tagashira[14], T. Takayama[14], K. Tamae[14], H. Tanaka[11], D. Takagi[14], T. Taniguchi[5], W. Tornow[4], D. Tracy[11], P. Vogel[3], Y-F. Wang[11], H. Watanabe[14], A. Wintenberg[9], J. Wolf[1] J. Wolker[9]

[1] Physics Department, University of Alabama, Tuscaloosa AL
[2] Chemistry Department, University of California, Berkeley, CA
[3] Norman Bridge Lab., Caltech, Pasadena CA
[4] Physics Department, Duke University, and TUNL, Durham NC
[5] KEK, Tsukuba, Japan
[6] Miyagi Gakuin Women's School, Miyagi, Japan
[7] Physics Department, University of New Mexico, Albuquerque NM
[8] Physics Department, North Carolina State, Raleigh NC and TUNL, Durham NC
[9] Oak Ridge National Laboratory, Oak Ridge TN
[10] Department of Geophysics, Stanford University, Stanford CA
[11] Physics Department, Stanford University, Stanford CA
[12] Physics Department, Technical University, Budapest, Hungary
[13] Physics Department, University of Tennessee, Knoxville TN
[14] Neutrino Physics Institute, Tohoku University, Sendai, Japan

ABSTRACT

We present the initial design of a very large 1 kton liquid scintillator detector to be installed in the underground cavity where Kamiokande used to be. The experiment is optimized to detect low-energy anti-neutrinos and it will perform unique measurements in the fields of neutrino physics, geophysics and astrophysics. One of the initial goals will be to perform a very long baseline oscillation experiment using a large number of nuclear reactors. Such an experiment will be sensitive to neutrino masses as low as $\Delta m^2 \simeq 7 \times 10^{-6}$ eV^2 attacking, for the first time with a laboratory measurement, some of the possible solutions to the "solar neutrino anomaly". This can be considered the "ultimate" neutrino mass test using the oscillation technique. The observation of neutrinos from the Earth, supernovae, atmosphere and nucleon decay will also be part of a very rich initial program, while in a later stage the observation of solar neutrinos and other channels requiring ultra-low background will become the main focus. KamLAND is conceived as a "scalable" detector that will be able to start in a very short time to deliver results on a number of essential physics issues that only require present-day technology. This first running period will also establish backgrounds and detector requirements for a second ultra-low background running phase.

Contents

1 Introduction

1.1 Project Overview

The study of neutrinos has recently become a central issue in many disciplines of fundamental science, including particle physics, cosmology and astrophysics. A number of experimental hints seem to suggest neutrino flavor oscillations and, while in some of these cases other phenomena may account for the anomalies observed, the chances are high that neutrinos may provide us with surprises and ultimately point us toward the understanding of elementary particles and interactions. At the same time it is believed that the observation of neutrinos coming from stars and galaxies may not only complement optical astronomy but also open new horizons of qualitatively new data about the Cosmos.

We describe here a detector that will be able to substantially add to our ability to study neutrinos, making possible a number of unique new measurements while improving many others. As shown in Figure 1 the detector will consist of 1,000 tons of liquid scintillator housed in the old Kamiokande cavern. The availability of the Kamiokande site makes possible the construction of a very ambitious detector at a comparatively modest cost, since there will be little civil engineering required.

The use of liquid scintillator producing substantially more light than a Čerenkov radiator will allow lower detection thresholds while, at the same time, will give good neutron detection efficiency, providing a clear signature for inverse-beta-decay anti-neutrino capture. The clear signature of anti-neutrinos, together with the capability of obtaining equally clear signals for neutrino scattering on carbon, allows KamLAND to do first-rate science using currently available technology and liquid scintillator purification levels. Furthermore the detector design follows a very attractive "scalable" approach in that KamLAND could become one of the best detectors for studying solar neutrino physics with essentially no modifications once the purification technology for scintillators will reach the levels needed for this purpose.

The detector will have as initial goal the study of electron anti-neutrinos. The presence of many large nuclear reactors in the 140 to 210 km range makes it ideally suited to study $\bar{\nu}_e - \bar{\nu}_X$ oscillations with an extremely long baseline. Such experiment will essentially represent the "ultimate" reactor neutrino oscillation experiment and will reach the smallest neutrino mass differences that can be probed with any laboratory experiment in the foreseeable future.

Anti-neutrinos from β-decay in the Earth's crust would also be measured for the first time, providing useful geophysical information, while the anti-neutrino and flavor identification capabilities of KamLAND will substantially add, from the beginning of running, to the field of supernova neutrinos. Measurements of specific channels for nucleon decay and atmospheric neutrinos will also be carried-out.

The experience in running the detector gained in this first period, together with the new technological advances gained in dealing with ultra-pure materials, will subse-

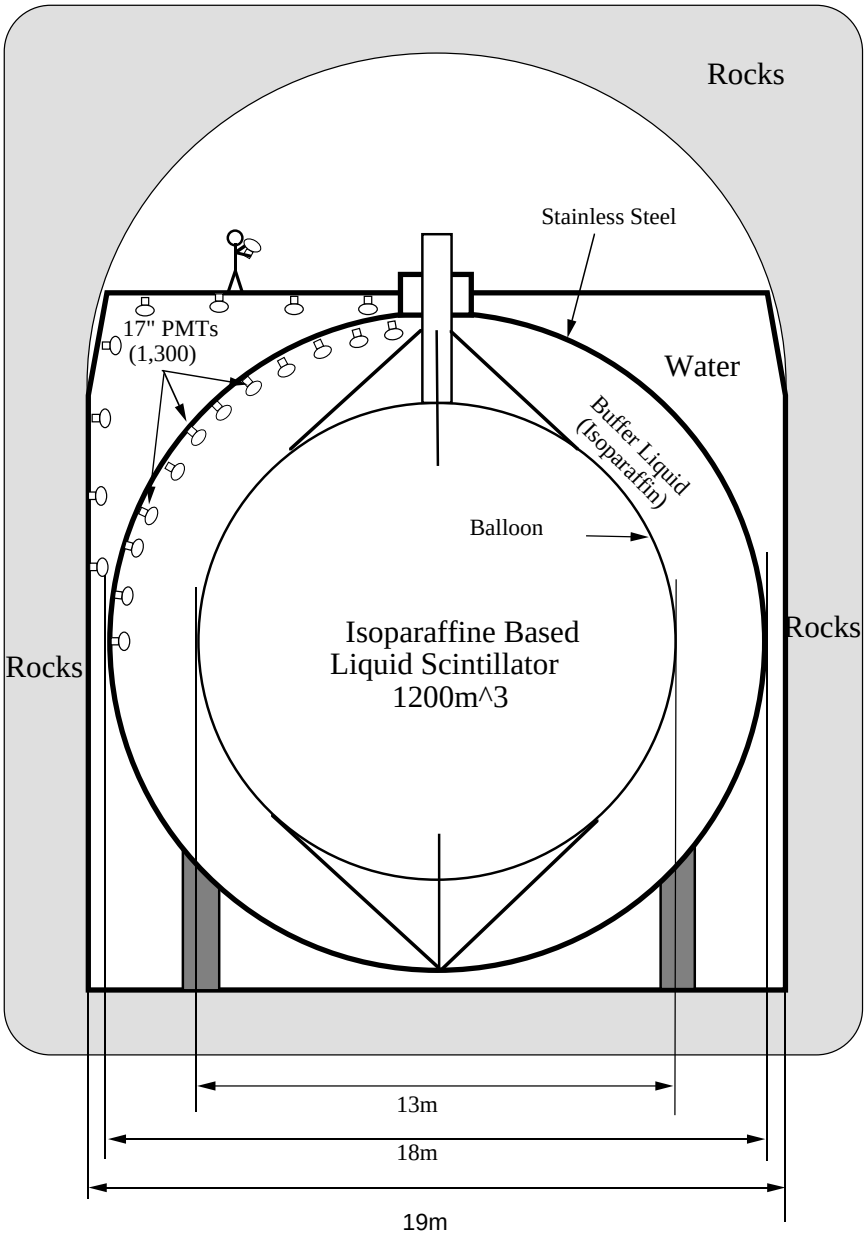

Figure 1: Schematic view of the KamLAND detector.

quently allow us to move in the most effective way to a new phase when solar neutrino spectroscopy with low threshold will represent the first priority. In this second phase other measurements requiring ultra-low backgrounds, such as a search for neutrinoless double-beta decay, may be implemented by properly doping the scintillator.

While the civil construction in the Kamiokande vault has already started, the US collaboration is planning to take over a number of important tasks in the construction of the experiment, ranging from the manufacturing of the plastic balloon that contains the scintillator, to the official simulation of the detector, to the design and construction of most front-end electronics, to the detector calibration system, to the radioactive qualification of the construction materials. Scintillator formulation and blending will be done jointly by Japanese and US scientists. In parallel to this we have initiated a vigorous long-term scintillator development program that will allow us to gradually improve the detector performances.

We also believe that the presence under the same mountain of the highly successful SuperKamiokande detector, also built and operated by a US-Japanese team, will strengthen our enterprise from the logistic and cultural standpoints.

1.2 Comparison with other Projects

KamLAND belongs to a new generation of low-background detectors generally built to study particle physics and astrophysics. All these experiments derive from the realization that a great wealth of fundamental science can be done in a very cost effective manner by studying naturally produced cosmic radiation.

A few points, however, set KamLAND in a very special category of projects. First, this experiment is not only observing natural phenomena but, in fact, will initially focus on a laboratory style experiment, using neutrinos produced in reactors. No other experiment has access to this physics. Second, KamLAND represents a new qualitative step in obtaining detailed low energy information from an unprecedented mass of material. In this respect our detector will have several times the mass of Borexino that is supposed to start data-taking in a similar period and it will therefore have access to a number of phenomena (like supernova neutrinos) that will produce marginal rates in other experiments. Finally, our detector is conceived in a unique scalable architecture that will allow us to start performing exciting measurements while improving the detector for future measurements. This allows us to propose a detector that will eventually rely on technology of the future but will need virtually no time for R&D before obtaining the first physics results.

2 Physics Considerations

Qualitatively new tools often lead to fundamentally new results in physics, some of them predicted, and others unexpected. In accelerator-based particle physics, which involves man-made phenomena created by interaction of accelerated particles with targets, and observing the reaction products, this statement is usually taken nearly for granted. However, the same is true in fields where one observes naturally occurring phenomena, such as in astrophysics. The extension of the observable wavelength range from visible to radio-waves, micro-waves, x-rays and gamma rays made possible by new telescopes both ground-based and on spacecrafts, led to the revolution in astrophysics in the last several decades. The emergence of large underground neutrino detectors in a similar way led to an unprecedented progress in the study of neutrinos, and objects emitting neutrinos. This is an ongoing development with a great promise. The proposed KamLAND detector, one of just a handful of devices specifically designed as neutrino detectors, will undoubtedly continue the tradition of its predecessor, Kamiokande, which was the first detector to prove that the solar neutrinos are indeed coming from the Sun, and with the IMB became the first detectors to observe supernova neutrinos and the atmospheric neutrino anomaly. Below, as an overture to the description of the KamLAND detector and its physics goals, we give a brief overview of the present status of neutrino physics.

2.1 Overview of Neutrino Physics

Neutrinos have the distinction of being the first elementary particles whose existence was predicted by a theorist in order to explain seemingly unrelated phenomena. Pauli made such prediction in 1930 in his famous letter in order to explain the continuous electron energy distribution in nuclear beta decay. It became immediately clear (thanks to Bethe and Peierls) that neutrinos will be difficult to observe, because the corresponding cross sections are so tiny. But in a series of experiments in 1953-56 Cowan, Reines and collaborators were able to prove convincingly that electron anti-neutrinos from nuclear reactors are able to cause the inverse neutron beta decay, $\bar{\nu}_{\rm e} + {\rm p} \rightarrow {\rm e}^+ + {\rm n}$, and hence that they are real particles. Shortly afterwards, in 1962, the separate identity of the muon neutrinos, ν_μ, was demonstrated. Another decade later, in 1975, the tau lepton was discovered by Perl *et al.*, and the observation of its decay properties implied the existence of the third neutrino, ν_τ. More recently the precise measurements of the decay width of the Z have shown that just three neutrino flavors participate in the weak interactions (at least for neutrinos with masses less than $1/2M_{\rm Z}$).

Ironically, while our knowledge of intrinsic neutrino properties remains quite poor, these particles have been used as tools to understand other phenomena. The tradition of underground detectors began thirty years ago when Davis and his collaborators were first able to detect neutrinos from the Sun. This was, and still is, the only clear

proof that the basic energy generation in stars is understood. We already mentioned the birth of neutrino astronomy with the observation of the neutrino burst from the supernova 1987A. Neutrino-induced reactions also played an important role in establishing what is now known as the Standard Model of electroweak interactions when in 1973 the neutral currents were discovered via the observation of the $\nu_\mu + e \to \nu_\mu + e$ scattering as well as the neutral current scattering of neutrinos on nucleons. Finally, neutrinos have been extensively used in deep inelastic scattering experiments at CERN and FNAL, exploring the quark structure of nucleons.

The main problem in neutrino physics today is the question whether neutrinos, like the charged fermions, have a mass. What are the theoretical aspects of this question? When the Standard Model of electroweak interactions was established, there was no experimental reason to introduce neutrino mass, and hence the model postulated that neutrinos are massless. This assumption was consistent with the observation that the individual lepton flavors seem to be conserved (and, naturally, the total lepton number as well). In addition, since the upper limits on neutrino masses are so much smaller than the masses of the corresponding charged leptons (or quarks) it was "natural" to assume that, in fact, neutrinos are massless, hence avoiding the unnaturally small mass ratios. However, at present there is a consensus among theorists that the Standard Model cannot be applicable at arbitrarily high energies, and that the requirement of renormalizability is not an absolute one. Rather, most theorists consider the Standard Model an effective field theory which should be a good description of nature only up to some energy limit where new physics will manifest itself. This point of view naturally leads to the expectation that neutrino masses acquire a value which is of the order $\langle\Phi\rangle^2/M$, where $\langle\Phi\rangle$ is the Higgs vacuum expectation value ($\approx$250 GeV), and M is the energy scale of new physics. As long as $\langle\Phi\rangle \ll M$ the neutrino masses will be naturally small.

One can come to a similar conclusion from a rather different viewpoint as well, as in the see-saw mechanism. In it, within the general framework of the Standard Model, one simply assumes the existence of new particles, the heavy neutrino electroweak singlets. The see-saw mechanism then results in the light Majorana neutrino mass of the order M_f^2/M_R, where M_f is the mass of a generic Dirac fermion (quark or lepton) and M_R is the mass of the heavy singlet neutrino. Again, as long as $\langle M_f\rangle \ll M_R$ physical neutrinos will be very light Majorana fermions. Thus, various reasonable extensions of the Standard Electroweak Model typically predict the existence of neutrino mass. They do not predict, however, how large or small this mass will be. Most of such extensions, moreover, lead to the expectation that the massive neutrinos are Majorana particles, and that the phenomenon of mixing, analogous to the Cabibbo-Kobayashi-Maskawa mixing among quarks, will govern their weak interactions.

At present there is no well established, and independently confirmed evidence that the scenario sketched above exists in nature. But the evidence for neutrino mass is being pursued in studies involving neutrinos created in astrophysical objects (Sun,

supernovae), in the earth atmosphere, in accelerators and nuclear reactors, in weak decays of nuclei and elementary particles, and in studies of reactions and decays where neutrinos appear as virtual particles, such as the neutrinoless double beta decay. This is a field in flux, with several experimental findings that can be interpreted as evidence for neutrino mass and mixing. Indeed, many of these findings, in particular the recent results from SuperKamiokande on atmospheric neutrinos, do not have any other likely explanations.

What values of the neutrino mass can one expect? An important upper limit can be established by arguments based on cosmology. If neutrinos are stable, or at least have lifetimes longer than the age of the Universe ($\simeq 10^{10}$y), one confidently expects the existence of the primordial neutrino sea, analogous to the well established 2.7 K background microwave radiation. If these primordial neutrinos are massive, their mass is constrained by the phenomenon of universal expansion. There is some flexibility in such a constraint, related to the uncertainty in the value of the Hubble constant, but a conservative upper limit for the *sum* of masses of all flavors of the stable neutrinos is about 100 eV. This limit can be further reduced if one accepts the often made claim that the so-called hot dark matter originates from massive neutrinos and it cannot contribute more than a fraction of the critical density ($\Omega = 1$) of the Universe. While these considerations do not mean that neutrinos are necessarily massive, they clearly show that if masses of the order of few eV were experimentally established, the consequences for cosmology and astrophysics would be very significant.

Conceptually, the simplest way to search for the neutrino mass is based on the kinematic studies of the particles produced in the weak decays such as ^{3}H $\rightarrow ^3$He $e^-\bar{\nu}_e$, $\pi \rightarrow \mu\nu_\mu$ and $\tau \rightarrow n\pi\nu_\tau$. The latter two processes result in limits for the mass of ν_μ and ν_τ well above the cosmological bound. The limit on the $\bar{\nu}_e$ mass from the tritium beta decay, however, is in the few eV range. Unfortunately, the interpretation of the tritium beta decay experiments is plagued at the present time by (apparently) systematic uncertainties leading to the best fit in the unphysical range $m_\nu^2 < 0$.

Another conceptually simple neutrino mass determination is based on the time-of-flight method with the supernova neutrinos. In particular, for a Galactic supernova, determining the time delay between the neutral current signal caused by the ν_μ and ν_τ neutrinos, and the charged current signal caused by the $\bar{\nu}_e$ neutrinos, one can reach sensitivities well below the cosmological bound. KamLAND will be particularly well equipped to perform such a measurement.

Before describing the concept and results of the search for neutrino oscillations, let us note that the neutrinoless double beta decay is another source of information on the neutrino mass. This process, in which a nucleus of charge Z and mass number A (A, Z are both even) decays as $(Z, A) \rightarrow (Z + 2, A) + 2e^-$ (no neutrino in the final state), is possible only when the corresponding neutrino is a massive Majorana particle. The quantity constrained by the limit on the lifetime of neutrinoless double beta decay, $\langle m_\nu \rangle = \sum m_i U_{e,i}^2$, is the sum over all massive neutrino flavors i and may involve cancellations caused by phases in the mixing matrix $U_{e,i}^2$. The best limit on

the quantity $\langle m_\nu \rangle$ comes at the present time from the Heidelberg-Moscow experiment in Gran Sasso with about 10 kg of ^{76}Ge as a source, and restricts this quantity to 0.5-1.0 eV, depending on the value of the corresponding nuclear matrix element. In some advanced stage of the KamLAND detector we might be able to perform a search for the neutrinoless double beta decay with much larger quantities of the source material, reaching a considerably better sensitivity to the neutrino Majorana mass.

The experimental hints for neutrino mass are at present based on the phenomenon of neutrino oscillations. If, as suggested above, neutrinos are massive particles which behave in analogy to quarks, the states with a definite mass (i.e., the "mass eigenstates" which propagate as plane waves in a vacuum) are not necessarily the partners of the charged leptons that couple to the vector bosons $W^{\pm}$ in doublets (i.e., the weak eigenstates)

$$\left(\begin{array}{c} \nu_{\rm e} \\ {\rm e}^- \end{array} \right) \, , \left(\begin{array}{c} \nu_\mu \\ \mu^- \end{array} \right) \, , \left(\begin{array}{c} \nu_\tau \\ \tau^- \end{array} \right) \, . \tag{1}$$

The weak eigenstates $|\nu_l\rangle$ will be in such a case linear superpositions of the mass eigenstates $|\nu_i\rangle$

$$|\nu_l\rangle = \sum_i U_{l,i} |\nu_i\rangle \, , \tag{2}$$

where the coefficients $U_{l,i}$ form the leptonic mixing matrix. If we assume that only three neutrinos can contribute in the Eq. (2) above, then U is a unitary 3×3 matrix.

If Eq. (2) is valid, we encounter the phenomenon of neutrino oscillations in which a neutrino which was initially in the weak eigenstate l can be spontaneously transformed, at least in part, into another weak eigenstate neutrino of flavor l'. To see how that happens, consider the time development of the mass eigenstate $|\nu_i\rangle$

$$|\nu_i(t)\rangle = e^{-i(E_i t - p_i L)} |\nu_i(0)\rangle \simeq e^{-i(m_i^2/2E)L} |\nu_i(0)\rangle \, , \tag{3}$$

where L is the flight path and in the last expression we assumed that the laboratory momenta and energies are much larger than the neutrino rest masses m_i. Let us consider now the propagation of a neutrino which was created at $L = 0$ as a weak eigenstate $|\nu_l\rangle$. At a distance L this state is described by

$$|\nu_l(L)\rangle \simeq \sum_i U_{l,i} e^{-i(m_i^2/2E)L} |\nu_i\rangle \; \simeq \; \sum_{l'} \sum_i U_{l,i} e^{-i(m_i^2/2E)L} U^*_{l',i} |\nu_{l'}\rangle \, . \tag{4}$$

Thus, the neutrino of flavor l acquired components corresponding to other flavors l'. This is a purely quantum mechanical effect, a consequence of the coherence in the superposition of states in Eq. (2). The probability that the "transition" $l \to l'$ happens at L is obviously

$$P(\nu_l \to \nu_{l'}, L) = |\sum_i U_{l,i} U^*_{l',i} e^{-i(m_i^2/2E)L}|^2 \, . \tag{5}$$

This is an oscillating function of the distance L. The oscillation length depends on the neutrino masses m_i (actually on the differences of mass squares), and the oscillation amplitude depends on the mixing matrix U.

Neutrino oscillation experiments are often analyzed in a simplified way by assuming that only two neutrino flavors mix, e.g. e and μ. The mixing matrix U then depends only on one mixing angle θ, and the oscillation probability, Eq. (5), is also simplified

$$U = \begin{pmatrix} \cos\theta & \sin\theta \\ -\sin\theta & \cos\theta \end{pmatrix} \ , \ P(\nu_{\rm e} \to \nu_\mu, L) = \sin^2 2\theta \sin^2(\Delta m^2 L/4E) \ . \qquad (6)$$

Here $\Delta m^2 \equiv m_1^2 - m_2^2$. The probability that $\nu_{\rm e}$ remains $\nu_{\rm e}$ is obviously $P(\nu_{\rm e} \to \nu_{\rm e}, L) = 1 - P(\nu_{\rm e} \to \nu_\mu, L)$.

In this two-flavor scenario the oscillation amplitude is $\sin^2 2\theta$ which vanishes if $\theta = 0$ or 90^o and is maximum if $\theta = 45^o$. The oscillation length is

$$L_{osc} = 2\pi \frac{2E_\nu}{\Delta m^2} = \frac{2.48 E_\nu({\rm MeV})}{\Delta m^2({\rm eV}^2)} {\rm meters} \ . \qquad (7)$$

To test for oscillations, one can perform either an *appearance* search in which one looks for new neutrino flavor, or a *disappearance* test in which one looks for a change in the flux normalization. In either case, tests performed at distance L are only sensitive to the values of Δm^2 for which $L \geq O(L_{osc})$.

So far we have considered only propagation of neutrinos in a vacuum. When neutrinos propagate in matter, such as in the solar interior, the oscillation pattern may be modified. This happens because electron neutrinos can forward scatter on electrons by charged current interactions, and other neutrino flavors cannot. Under favorable circumstances a resonance enhancement of the oscillation amplitude, the so-called Mikheyev-Smirnov-Wolfenstein (MSW) effect[1], can take place.

Numerous searches for neutrino oscillations were performed during the last two decades. Most of them resulted in an "exclusion plot", i.e., based on them certain ranges of the parameters Δm^2 and $\sin^2 2\theta$ can be excluded from further considerations as shown in Figure 2 for the case $\nu_\mu - \nu_{\rm e}$. However, at the present time there are three groups of measurements that suggest the existence of neutrino oscillations. (And, at the same time, the parameter ranges suggested by them are not excluded.) Only these *positive* results will be discussed here. (Details can be found in the latest edition of the Review of Particle Physics.)

The most prominent group of measurements which are interpreted as evidence for neutrino oscillations deals with the "missing" solar neutrinos. The Sun produces an intense flux of electron neutrinos as a byproduct of the fusion reactions which generate solar power. It is believed that the solar structure is understood sufficiently well so that the flux and energy spectrum of the solar neutrinos can be confidently predicted. The solar neutrino fluxes have been measured in five experiments so far. All of them report a deficit, i.e., the measured flux is less than the expected one. Moreover, the reduction depends on the neutrino energy, inferred experimentally from the thresholds of the individual detectors. The only viable explanation of the deficit appears to be neutrino oscillation (ν_e disappearance). By contrast to the attempts to explain the

deficit by modification of the solar model, which are unsuccessful, all existing data can be simply and elegantly explained by invoking neutrino mass. In particular, the solution based on the MSW effect offers the most popular scenario. Treating the problem in the two-flavor framework explained above, one arrives at two isolated islands in the Δm^2 – $\sin^2 2\theta$ plane. Both solutions correspond to $\Delta m^2 \approx 10^{-5}$ eV^2. One of them has rather small $\sin^2 2\theta \approx 10^{-2}$. The other one has much larger mixing angle, $\sin^2 2\theta \geq 0.5$. This solution also spans a larger interval of Δm^2 extending up to 10^{-4} eV^2. The KamLAND experiment will be able to exclude or confirm this "large angle" solution of the solar neutrino puzzle independently of extraneous effects.

The second set of measurements that can be interpreted as evidence for neutrino oscillations is the "atmospheric neutrino anomaly". Primary cosmic rays impinging on the nitrogen and oxygen nuclei at the top of the earth's atmosphere produce mostly pions, which subsequently decay via $\pi \to \mu\bar{\nu}_\mu, \mu \to \mathrm{e}\bar{\nu}_\mathrm{e}\nu_\mu$. The resulting atmospheric neutrinos therefore are expected to follow the $\nu_\mu : \nu_\mathrm{e} = 2 : 1$ ratio, which is essentially independent of the details of the complicated process that created them. In addition, in an underground detector, one can deduce the direction of the incoming neutrinos from the direction of the leptons (e and μ) created by the charged current interactions, at least at high enough energies. Again, one is reasonably confident that this zenith angle distribution can be accurately predicted. If the ν_μ and/or ν_e neutrinos oscillate, one expects deviations from the 2:1 ratio mentioned above. Also, since the zenith angle is simply related to the neutrino path length, one expects deviations from the expected zenith angle dependence of the lepton yield.

Both signatures of neutrino oscillations were in fact observed. The ν_μ/ν_e ratio is noticeably smaller, only about 60% of the expected value. This result has been confirmed in four detectors thus far, while contradicted by one (Frejus) with less statistics. The anomalous zenith angle dependence was first observed in Kamiokande, and has been now confirmed, with much better statistical significance, by SuperKamiokande. If these effects indeed signify neutrino oscillations (and we do not have another viable explanation) then the corresponding mixing angle is large, $\sin^2 2\theta \approx 1$. The value of the mass parameter Δm^2 remains uncertain, but is clearly in the range 10^{-2} - 10^{-4} eV^2. While the preferred scenario involves $\nu_\mu \to \nu_\tau$ oscillations, it is not clear that $\nu_\mu \to \nu_e$ oscillations are impossible. Again, KamLAND will be able to convincingly confirm or reject the latter possibility with a "laboratory" measurement.

Finally, the only indication for oscillations involving man-made neutrinos comes from the LSND experiment which finds evidence for the $\bar{\nu}_\mu \to \bar{\nu}_\mathrm{e}$ and, with more limited statistics, also for $\nu_\mu \to \nu_\mathrm{e}$. The former channel uses neutrinos from the pion and muon decay at rest, with energies less than $m_\mu/2$. The latter channel uses neutrinos from the pion decay in flight which have somewhat higher energies. These are appearance experiments; the observed signal should be absent if neutrinos do not oscillate. The well determined quantity is the oscillation probability, which has the value of about 3×10^{-3}. This result has not been independently confirmed but it is not contradicted by other evidence either.

As we can see from this brief discussion, the last decade brought us a number of clues. With the exception of the LSND evidence, they all came from large underground detectors. A number of new experiments is in various stages of planning or building. It is very likely that the next decade will bring the resolution of the neutrino mass puzzle and KamLAND will play an essential role in this enterprise.

2.2 Reactor Oscillation Experiment

2.2.1 Laboratory Neutrino Oscillation Experiments

As we have described in the previous section most of the evidence for neutrino oscillations derives from experiments performed with neutrinos produced by natural phenomena outside the direct control of the experimenter. Although we now have reasonable confidence in our understanding of these sources, "laboratory style" experiments are essential to conclusively separate the intrinsic neutrino physics from other phenomena.

Historically, neutrino oscillation experiments have been performed using both nuclear reactors and accelerators as sources. The regions of Δm^2 and $\sin^2 2\theta$ covered by different experiments are shown in Figure 2 for $\nu_e - \nu_\mu$ oscillations.

From Equation 7 it is clear that in order to probe sufficiently small Δm^2, long baselines have to be combined with low energy neutrinos. On the other hand small mixing parameters $\sin^2 2\theta$ are generally accessible only to appearance experiments where few events of the right flavor are statistically very significant. As a consequence, accelerator-based experiments with appearance signatures and lower backgrounds are naturally suited to explore regions of small $\sin^2 2\theta$, while, reactor-based ones, with low energy neutrinos, can only perform disappearance measurements but naturally excel in the exploration of small Δm^2 values. This general concept can be see at work in Figure 2 where the parameter space is carved in the two directions by the different types of experiments.

Since theory does not give precise hints on what neutrino masses should be, the first generation of neutrino oscillation experiments, triggered by the original hypothesis of Pontecorvo [2], was targeted at whatever range of parameters was accessible at that time. The situation changed in the last decade mostly due to the inputs from astrophysics and cosmology described above. As a consequence, recent experiments concentrated until now on two regions, motivated by the atmospheric neutrino anomaly and by the neutrino mass range that would produce a substantial contribution to the dark matter in the universe. The last case corresponds, as shown in Figure 2, to $\approx$ 1eV masses and possibly very small mixing angle. This region is well adapted to accelerator experiments and a number of groups are presently probing it: Chorus [3] and Nomad [4] at CERN, Karmen [5] at RAL and LNSD [6] at Los Alamos. This last experiment has in fact presented evidence [7] for oscillations and a number of new experiments have been designed to investigate this region further. Such experiments include an upgrade of the Karmen experiment running now, the

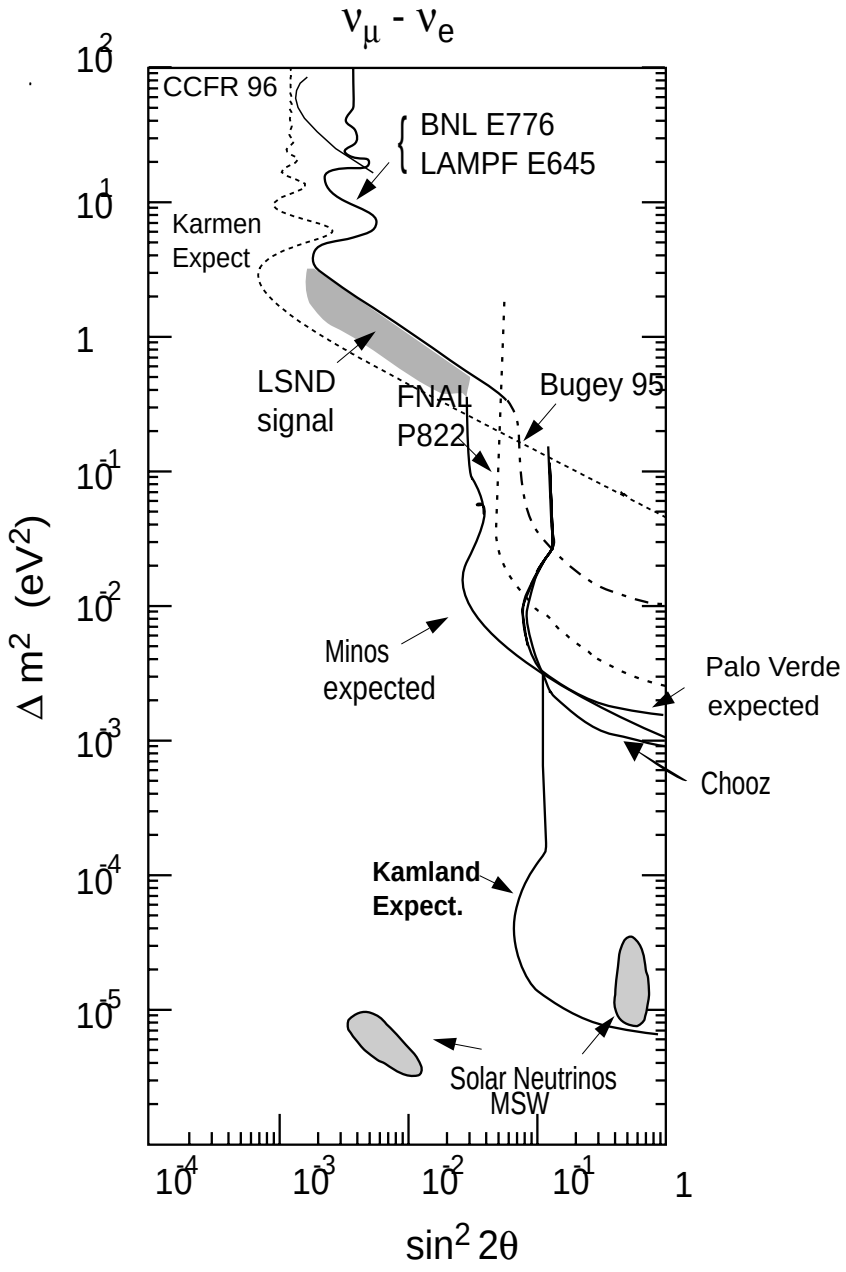

Figure 2: Phasespace for $\nu_e - \nu_\mu$ oscillations. The existing limits are compared with current and future experiments and the region obtained by interpreting the solar neutrino anomaly as due to oscillations. The MSW mechanism is used in plotting the solar neutrino regions. We do not show here, for simplicity, the different regions spanning the range $2 \times 10^{-4} < \Delta m^2 < 2 \times 10^{-2}\text{eV}^2$ and large mixing-angle that results from different interpretations of the atmospheric neutrino anomaly. The sensitivity of reactor experiments is the same for $\nu_e - \nu_\tau$ oscillations. Limits are at 90% CL.

Boone experiments [8] at FNAL and the TOSCA experiment [9] at CERN.

The region in parameter space suggested by the atmospheric neutrino anomaly is under investigation by reactor experiments like Chooz [10] and Palo Verde [11], by Minos [12], K2K [13] and by a possible new set of experiments performed between CERN and Gran Sasso in Italy. We note here that, while Chooz and Palo Verde are only sensitive to $\bar{\nu}_{\rm e} - \bar{\nu}_{\rm X}$ oscillations, the accelerator experiments will be able to measure any mixing between the three neutrino flavors.

The region of parameter space relevant to the solar neutrino anomaly has not been accessible until now to terrestrial experiments and KamLAND represent the first opportunity to perform this unique physics. The low energy of the reactor neutrinos, together with the formidable baseline available for the measurement (≈ 170 km) will give us access to a qualitatively different region of the $\Delta m^2 - \sin^2 2\theta$ plane, with a minimum Δm^2 sensitivity of $7 \times 10^{-6}\mathrm{eV}^2$, 100 times smaller than what is presently available or expected at Minos and other accelerator experiments. Since the solar neutrino anomaly concerns oscillations with electron neutrinos, a reactor experiment is perfectly suited to this study. In addition KamLAND will explore any conceivable effect having to do with the atmospheric neutrino anomaly in the $\bar{\nu}_{\rm e} - \bar{\nu}_{\mu}$ channel. No other laboratory experiment has access to such a large and uncharted territory.

2.2.2 Very-Long Baseline Oscillations with KamLAND

Nuclear reactors produce isotropically $\bar{\nu}_{\rm e}$ in the β decay of the neutron-rich fission fragments. Electron anti-neutrinos are primarily captured by protons in the detector's liquid scintillator according to the reaction:

$$\bar{\nu}_{\rm e} + {\rm p} \rightarrow {\rm e}^+ + {\rm n}$$

that at lowest order has an approximate cross section[25]

$$\sigma(E_\nu) = \frac{2\pi^2\hbar^3}{m_{\rm e}^5 c^8 f \tau_n}(E_\nu - \Delta M c^2)[(E_\nu - \Delta M c^2)^2 - m_{\rm e}^2 c^4]^{1/2}$$

where ΔM is the n-p mass difference, $\tau_{\rm n}$ is the neutron lifetime, f is the Fermi function for neutron β-decay and the neutron recoil is neglected. The error in the knowledge of such cross-section is about 1% and it is dominated by the experimental uncertainty on the neutron lifetime[26].

While the positron from the final state deposits its energy in ionization and annihilates with an electron from the scintillator, the neutron is thermalized and captured in the liquid according to the reaction ${\rm n} + {\rm p} \rightarrow {\rm d} + \gamma$, where the photon has an energy of 2.2 MeV. The neutron capture time on protons is 160μs so that anti-neutrino events present a signature consisting of a delayed coincidence between the (prompt) positron signal and the (delayed) neutron one. The neutrino capture reaction has a threshold of $\Delta M + m_{\rm e} \simeq 1.8$ MeV.

For all practical purposes the reactor anti-neutrino flux and spectrum depend only on the composition of the core in terms of the four isotopes ^{235}U, ^{238}U, ^{239}Pu and ^{241}Pu being fissioned in the reactor. Neutrinos are then produced by long chains of daughter isotopes and hundreds of different β-decays have to be included to account for the observed yields. The modeling of such processes is quite a formidable task but there is nowadays a very good agreement between theoretical calculations and experimental data. Two ways can be used to experimentally cross check theoretical models. In one case the electron spectra for fission-produced chains can be experimentally measured for each of the four parent isotopes. From this data, available only for (^{235}U, ^{239}Pu and ^{241}Pu), anti-neutrino spectra can be derived without loss of accuracy[14], obtaining a total uncertainty on the flux of about 3%. Alternatively, anti-neutrino flux and spectra have been directly measured [15] in several high-statistic experiments with detectors of known efficiency at small distances. These data are usually a by-product of previous reactor oscillation experiments where the anti-neutrinos have been measured at different distances. Since these observations have been found to be consistent with a $1/r^2$ law (no oscillations at short baselines) they can now be used as a determination of the absolute anti-neutrino spectra. A total error of about 1.4% has been achieved in these measurements. The situation is illustrated in Figure 3 where the measured anti-neutrino induced positron spectrum is compared with its prediction from β-spectroscopy.

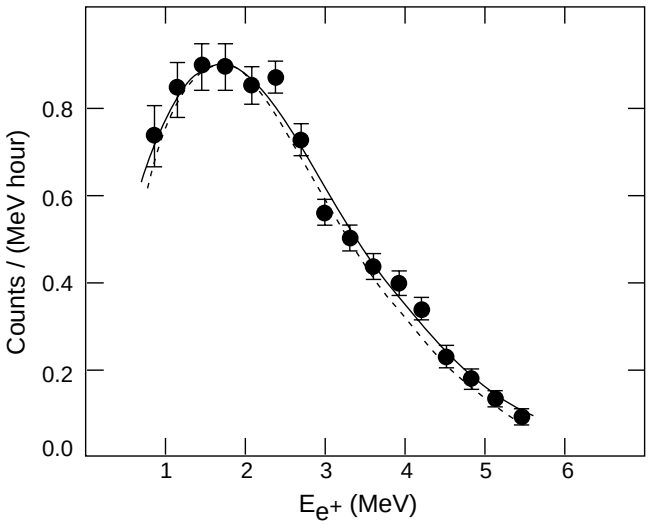

Figure 3: Positron spectrum measured at 45.9 m from the core of the Gösgen reactor[16]. Data points are obtained after background subtraction, errors are statistical only. The solid curve is a fit to the data assuming no oscillations. The dashed curve is derived by independent β-spectroscopy.

All experimental methods and calculations agree with each other within errors so that, given the history of power and fuel composition for a reactor, its anti-neutrino

energy spectrum can be computed with an error of about 3%. We note here that for this kind of experiments a "near measurement" is superfluous as, in essence, all the information needed can be readily derived from the previous generations of experiments, using their result that no oscillations take place at those shorter baselines.

Since the neutrino spectrum is only measured above the 1.8 MeV threshold, only prompt (energetic) decays contribute to the useful flux and the "neutrino luminosity" tracks very well in time the power output of the reactor. Generally, a few hours after a reactor turns off the neutrino flux above threshold has become negligible. Similarly, the equilibrium for neutrinos above threshold is established already several hours after the reactor is turned on.

There are 17 commercial nuclear power plants in Japan, supplying 1/3 (or 120 GW thermal) of the total electric power in the country[17]. At the Kamioka site there is an anti-neutrino flux of $3 \times 10^6 \mathrm{cm}^{-2}\mathrm{s}^{-1}$ (or $1 \times 10^6 \mathrm{cm}^{-2}\mathrm{s}^{-1}$ for $E_{\bar{\nu}} > 1.8\mathrm{MeV}$) from these reactors. 80% of such flux derives from reactors at a distance between 140 km and 210 km, so that there is a limited range of baselines. The total number of $\bar{\nu}\mathrm{p} \to \mathrm{ne}^+$ events expected from reactors is 750 $\mathrm{kton}^{-1}\mathrm{year}^{-1}$ for a $\mathrm{C}_n\mathrm{H}_{2n+2}$ target, the detailed sharing between the five plants giving the largest contribution being listed in Table 1.

Reactor Site	Thermal Power (GW)	Distance (km)	Rate (Events/year)
Kashiwazaki	24.5	160	273
Ohi	13.7	180	120
Takahama	10.2	190	80
Hamaoka	10.6	210	68
Tsuruga	4.5	140	65
Total	130.0		750

Table 1: Expected contribution of different reactors to the neutrino rates detected in KamLAND in the case of no oscillations. Several other reactors each giving a small contribution do not have individual entries in the table but are included in the total.

Although reactor experiments are essentially of the disappearance type, the anti-neutrino energy spectrum is modified by oscillations so that, in general, extra information is available besides the absolute neutrino count. In our case, even in the absence of one single baseline, the energy spectrum still plays an important role, at least for rather large mass differences. This is shown in Figure 4 where the energy spectrum is plotted for the case of no oscillation (original reactor spectrum) and for three different oscillation scenarios.

Since the measurement of an absolute flux is essential to reach the best sensitivity, it is customary in this kind of experiments to measure backgrounds at zero or low

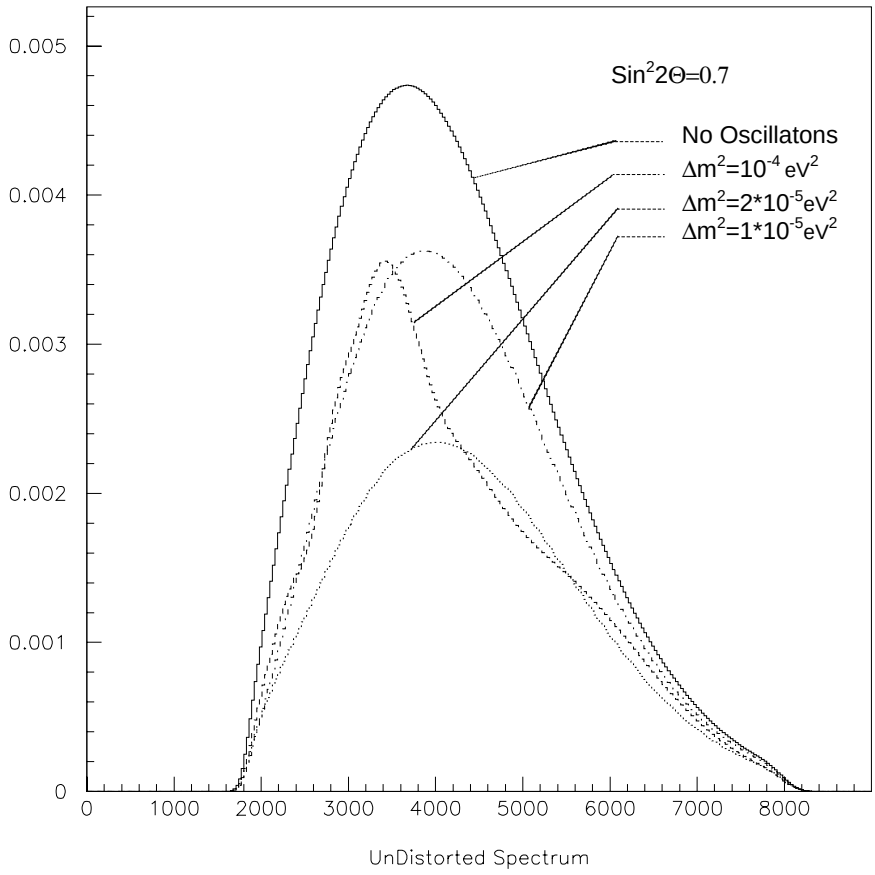

Figure 4: Energy spectrum from reactors neutrinos expected in KamLAND for different types of oscillation scenarios and for the case of no oscillations.

reactor power. In our case this is possible even in the presence of a large number of reactors since many of them are shut down for preventive maintenance in the fall and spring when the demand of electricity is lower.

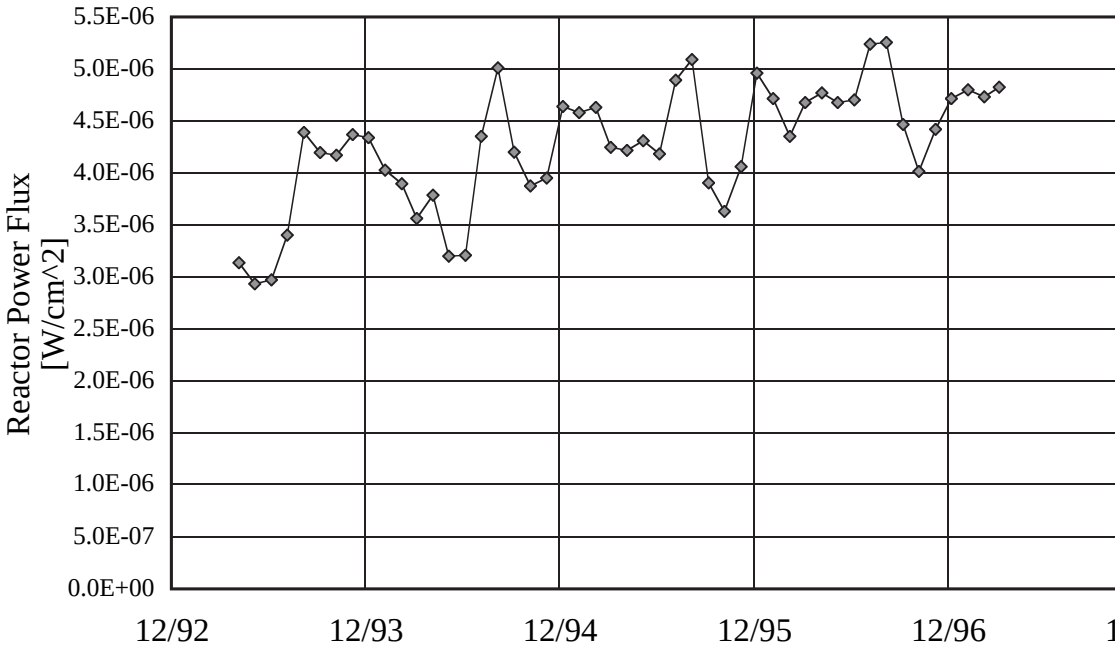

Figure 5: Power level of Japanese reactors as function of time. Low power periods in the fall season are alternated with peak high power in the summer.

Figure 5 shows the total thermal power flux at Kamioka as function of time during a typical year, where 30% variations are expected and can be used to estimate the background of the measurement.

Finally, the sensitivity of the reactor oscillation experiment that can be performed at KamLAND in three years of running is shown in Figure 2. The error due to background fluctuations is included in the solid curve. A mass-difference-squared $\Delta m^2 \simeq 7 \times 10^{-6}$ eV^2 can be reached, improving the present sensitivity by over 2 orders of magnitude and entirely covering the LMAS for the solar neutrinos.

2.3 Terrestrial Anti-Neutrinos

2.3.1 Physics of Terrestrial Neutrinos

The cooling rate of our planet and its contents of heavy elements are central issues in the earth sciences and KamLAND will provide an entirely new perspective in these fields.

The earth radiates about 40 TW of heat from its surface. About 40% of this energy (or 16 TW) is believed to have radiogenic origin with 90% of it deriving from decays of ^{238}U and ^{232}Th. Radiogenic heat is therefore an essential component of the present dynamics of our planet. As discussed by several authors[18, 19, 20] the concentration of these isotopes can be mapped, at planetary scale, by direct detection of electron anti-neutrinos deriving from the β-decay processes. Since neutrinos have a mean free path in solids many orders of magnitude larger that the size of our planet, the neutrino field is analogous, except for directionality information, to a gravitational field, where the sources are represented by radioactive density (as opposed to mass density). KamLAND will play an essential role in this field being the largest of the two detectors able to perform these kinds of measurements in the near future.

Although the total U abundance and U/Th ratio can be derived rather reliably for the solar system, different models of the earth differ in detailed predictions of the distribution of these isotopes in the planet's volume. In general[21] $\sim 50\%$ of the U and Th is assumed to be dispersed in the mantle, the rest being concentrated in a rather thin ($\sim$ 35km thick) crust under the continental plates. The thinner ($\sim$ 6.5km thick) oceanic crust is supposed to be much poorer in these two isotopes.

Terrestrial neutrino flux and spectrum measurements with 20% accuracy will therefore allow us to gain valuable insights on early processes in the formation of our planet that gave origin to the core, mantle and crust. At the same time our measurements will provide a better understanding of the present planetary dynamics and heat flows, helping in calibrating models of partial melting in the mantle.

It has been recently remarked[22, 23] that the combination of the KamLAND data with similar data collected by the Borexino[24] detector at Gran Sasso (Italy) will further advance the field by sampling two sites located in regions with rather different crustal contributions.

The first detection of terrestrial neutrinos carries the promise of opening a new field in geophysics and, as most "first detections" in neutrino physics could provide us with unexpected surprises !

2.3.2 KamLAND Sensitivity

Although the study of terrestrial anti-neutrinos was proposed as early as 1966[18] practical difficulties due to the very small cross-sections and very low energies involved have made this physics impractical until now. KamLAND has the ability to detect energy depositions of the order of 1 MeV in a unprecedented amount (1 kton) of liquid scintillator and is therefore ideally suited for this study. It is important to realize that low energy anti-neutrinos are easily detected with very low background in KamLAND thanks to their very specific signature.

Since the maximum energy carried by terrestrial neutrinos is[20] 3.27 MeV and the capture threshold is 1.8 MeV, the maximum in the energy spectrum detected in the prompt part of the event will be 2.49 MeV (including the 1.02 MeV from positron

annihilations). For energies above our threshold only the Thorium and Uranium decay chains give a detectable amount of events. ^{234}Pa from the U chain and ^{228}Ac and ^{212}Bi of the Th chain have similar endpoints (respectively 2.29 MeV, 2.08 MeV and 2.25 MeV) while ^{214}Bi from the U chain has an endpoint of 3.26 MeV. Therefore the energy spectrum observed for the prompt part of the event has a characteristic double-hump structure shown in Figure 6. Anti-neutrinos from nuclear reactors give, as described above, a similar signature, but their energy is substantially higher and, as shown in the Figure, they can be easily separated from the terrestrial anti-neutrinos. As a matter of fact, reactor neutrinos will represent a useful overall detector calibration in observing for the first time terrestrial neutrinos.

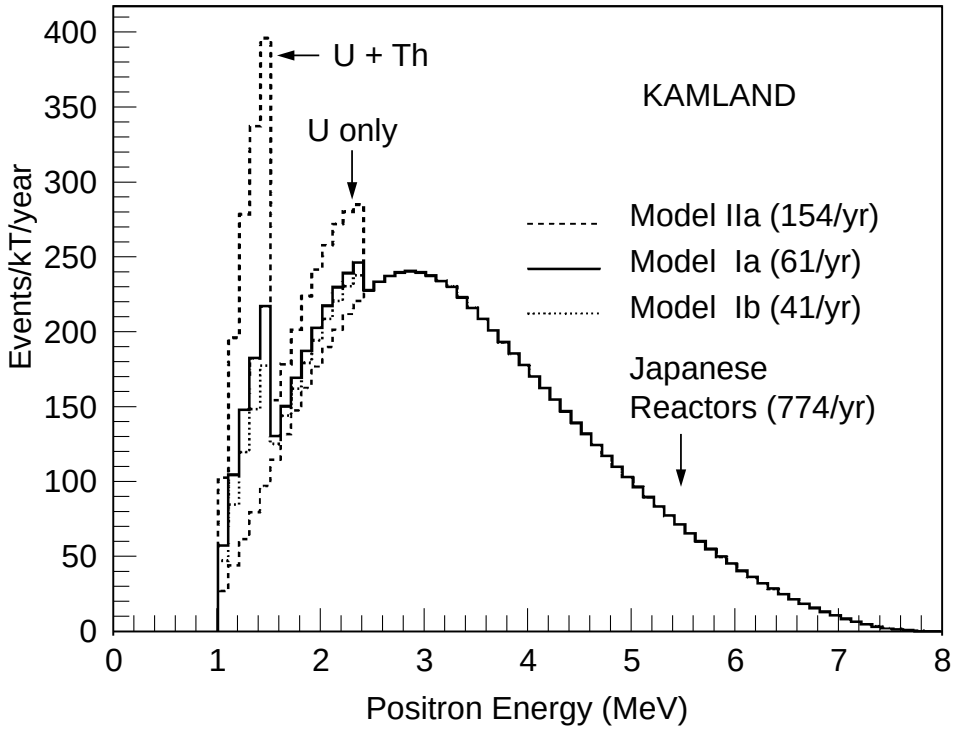

Figure 6: Energy spectrum from terrestrial anti-neutrinos compared with reactor signal as expected in KamLAND. Three different geophysical models [22] are shown for the terrestrial anti-neutrinos and no oscillations are assumed for all the spectra shown.

The two lower spectra (Ia and Ib) superimposed in Figure 6 for the terrestrial anti-neutrino component correspond to two different possible geophysical models with different heavy elements concentration in the oceanic and continental crusts[22]. The highest curve (IIa) is given as a reference and shows what the spectrum would be in the extreme case where the entire 40 TW of heat escaping from the Earth's interior was generated by the Th and U decay chains. In one year of data-taking, model Ia

would give an integral of 61 events while model Ib would give only 41 events, and a differentiation between the two at 3σ level could be obtained in five years of data-taking, taking into account the fluctuations of the background due to the reactor neutrinos.

In addition to this type of study the double-hump structure will allow us to separate the U from the Th contributions since the higher energy hump is entirely due to U.

2.3.3 Combined Measurement with Borexino

While we have shown that KamLAND will allow us to detect terrestrial neutrinos the combination of KamLAND and Borexino data will provide qualitatively different information as the two detectors are located in areas with rather different geology. In particular, while KamLAND sits at the edge between oceanic and continental crusts, Borexino is located more centrally on the continental crust. In addition Borexino, although smaller, will have a much reduced reactor background, since Italy has no power reactors in operation. This situation is shown in Figure 7.

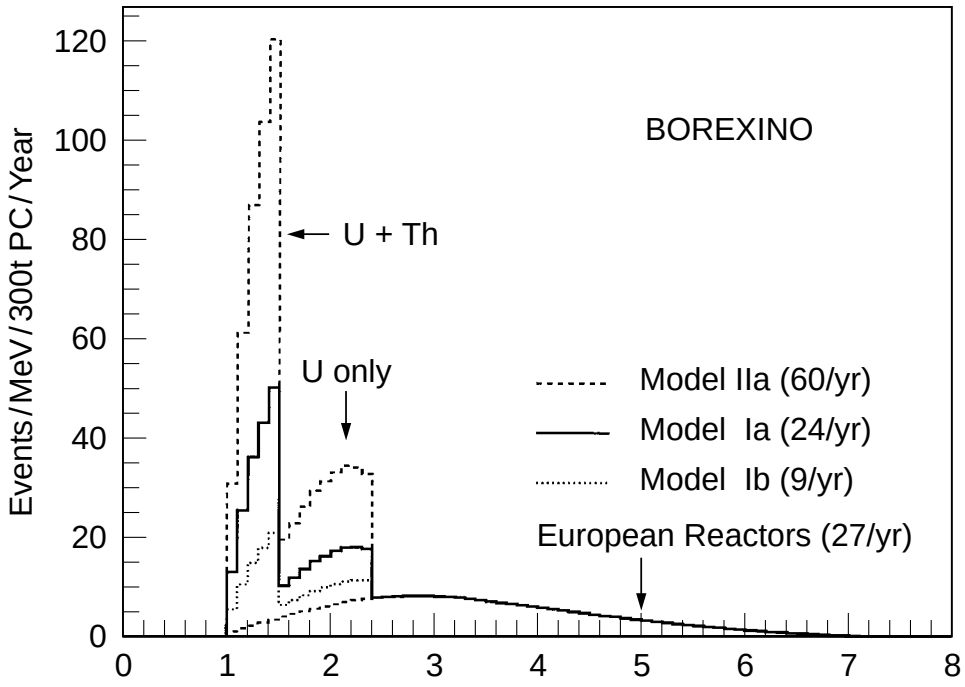

Figure 7: Energy spectrum from terrestrial anti-neutrinos compared with reactor signal as expected in Borexino. The same three geophysical models shown in Figure 6 are also represented here.

Although the statistics is much lower than in the KamLAND case, the combination of the data will allow us to separate out the amount of heavy elements in the continental crust and in the oceanic crust and mantle. If terrestrial neutrinos will indeed be discovered it is conceivable that a new dedicated detector, in a peculiar geophysical location and far away from nuclear reactors will be needed to fully separate the different contributions and fully develop this new field of science.

2.4 Supernova Detection

2.4.1 Observation of Galactic Supernovae in KamLAND

The KamLAND detector, containing a large amount of carbon nuclei, opens entirely new vistas in the detection of ν and $\bar{\nu}$ from supernovae explosions. The charged current reactions on protons, $\bar{\nu}_{\rm e} + {\rm p} \rightarrow {\rm e}^+ + {\rm n}$, and the neutrino-electron scattering, $\nu + {\rm e} \rightarrow \nu + {\rm e}$, will also be present and at least the former one will be clearly observable, but in that respect KamLAND cannot compete with the much larger SuperKamiokande. For this reason only the scattering on carbon will be discussed in this proposal.

Below we assume that there will be a supernova approximately in the center of the galaxy at the distance of 10 kpc from us. We further assume that the total energy release has the "standard" value of 3×10^{53} erg, and that this energy is emitted in neutrinos and equally divided between the six neutrino flavors[27]. However, different neutrino flavors do not necessarily have the same average energy, or temperature. This leads to the flux of neutrinos of flavor ν at Earth of

$$f_\nu = \frac{2.6 \times 10^{11}}{\langle E_\nu \rangle ({\rm MeV})} \ {\rm cm}^{-2} \ {\rm s}^{-1} \ , \tag{8}$$

where we assumed 10 seconds emission time. If we also assume that the neutrinos have Fermi-Dirac distribution[28] with the temperature T, we can use the relation $\langle E_\nu \rangle = 3.152T$ in order to further simplify the above formula.

For the purpose of the estimate we take a 1 kt detector containing 4.3×10^{31} nuclei of ^{12}C and twice as many protons. Then, for the reactions on carbon the total count rate is

$$N_\nu = \frac{35.3 \langle \sigma \rangle}{T({\rm MeV})} \ {\rm counts}, \tag{9}$$

where the thermally averaged cross section $\langle \sigma \rangle$ is in units of 10^{-42} cm^2 and the temperature is in MeV. We assume here that the detection efficiency is 100%.

There are three neutrino-induced reactions on carbon of particular interest for the supernova detection at KamLAND. They are shown in Figure 8.

The two charged current reactions

$$\begin{aligned} \nu_{\rm e} + {}^{12}{\rm C} &\rightarrow {\rm e}^- + {}^{12}{\rm N}_{g.s} \ , \\ \bar{\nu}_{\rm e} + {}^{12}{\rm C} &\rightarrow {\rm e}^+ + {}^{12}{\rm B}_{g.s} \end{aligned} \tag{10}$$

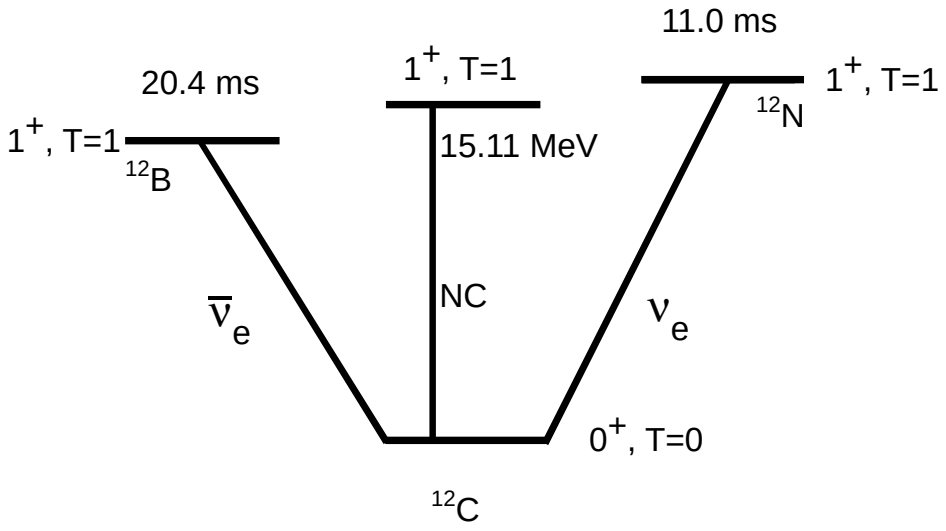

Figure 8: Schematic representation of the three neutrino reactions on carbon considered.

have thresholds of 17.3 MeV and 14.4 MeV respectively. They can be recognized by observing not only the corresponding $e^{\pm}$, but also the delayed coincidence with the $\beta^{\pm}$ decay with half-lives of 11.0 and 20.4 ms respectively. Thus, the signal for these exclusive reactions will be essentially background free.

The neutral current reaction of interest is the excitation of the $I^{\pi} = 1^{+}$, $T = 1$ state at 15.11 MeV in ^{12}C which de-excites by gamma emission,

$$\nu + ^{12}\mathrm{C} \rightarrow \nu + ^{12}\mathrm{C}(15.11\mathrm{MeV}) \ . \tag{11}$$

All neutrino flavors can excite this state; the cross section depends only on the neutrino energy or temperature (however, there is a difference between the cross section for neutrinos and anti-neutrinos as shown below).

The cross sections for these exclusive reactions on carbon have been calculated in Ref.[29]. Two of them were observed experimentally with neutrino energies comparable to the case of supernova neutrino emission [30, 31], and the measured cross sections agree with calculations very well. The thermally averaged cross sections as a function of the neutrino temperature are shown in Figure 9.

These cross section can be readily translated into the expected number of events in KamLAND using Equation 9.

First, we have to specify the temperatures of the different neutrino flavors. As a standard we use the average neutrino energies of Ref.[32]: for ν_{e} we take T=3.5 MeV, $\langle E_{\nu} \rangle$ = 11 MeV; for $\bar{\nu}_{\mathrm{e}}$ T=5 MeV, $\langle E_{\nu} \rangle$ = 16 MeV; and for ν_{μ}, $\bar{\nu}_{\mu}$, ν_{τ}, $\bar{\nu}_{\tau}$ (collectively called ν_x) T=8 MeV, $\langle E_{\nu} \rangle$ = 25 MeV. The expected number of events is shown in Table 2. There the charged current reactions are shown in columns two

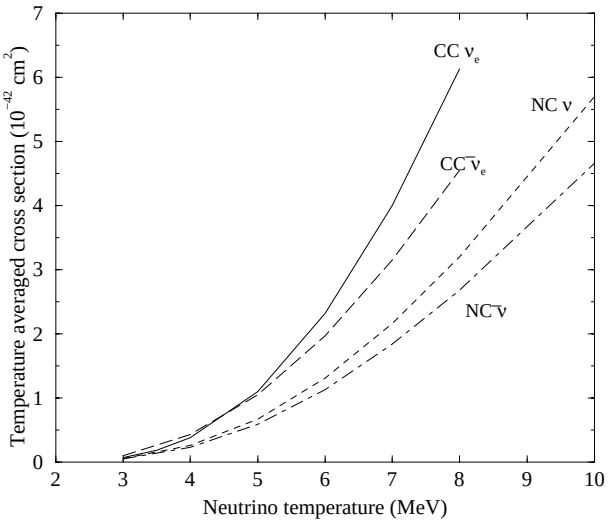

Figure 9: Cross section on carbon for the different cases of supernova neutrinos analyzed in the text as function of temperature.

and three, and the neutral current reactions in column four. The first three lines give the expected number of events expected without effects of neutrino oscillations. The fourth line gives the expected number of events when vacuum oscillations (and maximum mixing) are present. Finally, in the last line we show the number of events expected for the matter-enhanced MSW oscillations.

Temperature (MeV)	ν_e ^{12}C $\rightarrow$ ^{12}N$_{gs}e^-$	$\bar{\nu}_e$ ^{12}C$\rightarrow$ ^{12}B$_{gs}e^+$	ν_x ^{12}C$\rightarrow$ ^{12}C(15.11) ν_x
3.5 (ν_e)	1.9	-	1.5
5.0 ($\bar{\nu}_e$)	-	7.4	4.2
8.0 (ν_x)	-	-	51.9$^{a)}$
vacuum osc.	14.5	13.8	57.6$^{b)}$
MSW osc.	27	7.4	57.6$^{b)}$

Table 2: Expected rates in KamLAND for supernova neutrinos scattering on carbon. Different cases discussed in the text are presented. In $^{a)}$ we add the contribution of all ν_x and their antiparticles while in $^{b)}$ we give the total number of 15.11 MeV photons detected.

Thus, one can see that for a supernova at the nominal distance of 10 kpc, and with the standard neutrino emission parameters, the exclusive charged current reactions give only about 9 counts altogether, not enough for any quantitative conclusions.

However, using these reactions, one can exclude, or confirm, various oscillation hypotheses.

So, for example, if the "just so" neutrino oscillations are responsible for the solar neutrino deficit, we expect to see 14.5 counts in the $\nu_e^{12}C \rightarrow^{12} N_{gs}e^-$ channel, and 13.8 counts in the $\bar{\nu}_e^{12}C \rightarrow^{12} B_{gs}e^+$ channel. That would represent about 5 σ, i.e. enough to claim a discovery of this solution of the solar neutrino problem.

Another possibility is the MSW matter-enhanced neutrino oscillations $\nu_e \leftrightarrow \nu_x$. In that case we would observe 27 counts in the $\nu_e^{12}C \rightarrow^{12} N_{gs}e^-$, again a 5 standard deviations effect. No other neutrino detector offers such a sensitivity to this oscillation mode.

But most important is the neutral current excitation of the 15.11 MeV state. This mode can be recognized only by the simple signature of the corresponding γ-ray. The signal must be separated from the numerous positrons from the reaction $\bar{\nu}_e + p \rightarrow e^+ + n$, where one expects 330 events at KamLAND. In order to obtain a conservative estimate we now assume an energy resolution for γs of $\sigma = 20\%\sqrt{E}$ MeV, twice as large as the design number for our detector. The positron spectrum is shown

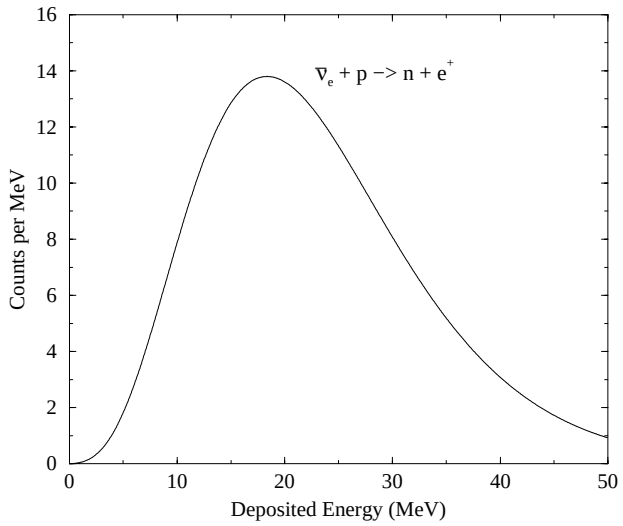

Figure 10: Positron spectrum from supernova neutrino scattering on protons.

in Figure 10. This is the time integral; it is usually assumed that the neutrino emission is a decreasing function of time, lasting for about 10 seconds. The positron signal will be very robust, exceeded only by the signal of SuperKamiokande. (The relation is 32*14/18 = 25, where the factor 32 comes from the size and 14/18 from the molecular weight.) At 15 MeV there will be about 13 positron counts per MeV. So, the statistical uncertainty for a bin of $2 \times \sqrt{2}\sigma$ width, containing 95% of the gammas, is about 4 counts. Therefore, the uncertainty in determining the rate of the

15.11 MeV gammas stemming from the positron background will be smaller than the statistical uncertainty of the signal itself (± 7 counts).

The full spectrum obtained adding positron and γ contributions is shown in Figure 11.

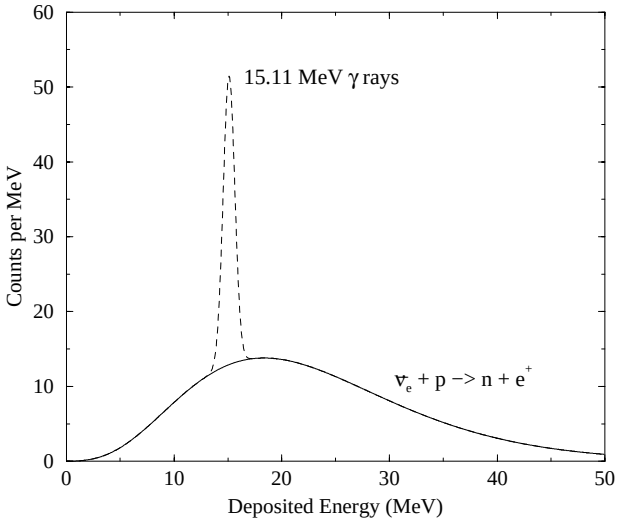

Figure 11: Energy spectrum from "standard" supernova explosion. The energy detected is the sum of the positron and γ-ray energies. A very conservative resolution of $\sigma = 20\%\sqrt{E}$ MeV, twice as large as the design number, has been used for this plot.

Thus, the signal of the neutral current, dominated ($\sim 90\%$) by the ν_x neutrinos, will be visible at more than 5 standard deviations level. If the distance and neutrino luminosity of the supernova is known, or measured from the positron yield at KamLAND or elsewhere, one can use the 15.11 MeV signal as a diagnostics of the ν_x temperature. We calculate that the signal will change by 21% if the ν_x temperature changes by 1 MeV (near $T = 8$ MeV). Thus, at KamLAND the ν_x temperature can be determined to ± 1 MeV. This would be a very significant result.

On the other hand, without the ability to determine the direction of the recoil electrons, the signal of the $\nu + \mathrm{e} \to \nu + \mathrm{e}$ electron - neutrino scattering will be weak, and probably unrecognizable. We calculate that there will be 8 events associated with ν_e scattering, 3 events associated with $\bar{\nu}_\mathrm{e}$ scattering, and 5 events associated with ν_x scattering. These 16 events will be overwhelmed by the positron signal.

To conclude we note that the supernova detection illustrated above requires the ability to detect photons up to about 50 MeV of energy. In addition we will need to be able to take a substantial event rate with little deadtime for periods of tens of seconds (the expected duration of the burst). All these constraints, as well as the ability to record the absolute time, are used in the detector design below.

2.4.2 Comparison with other Detectors

We already mentioned that in SuperKamiokande the positron signal from $\bar{\nu}_e + p \rightarrow e^+ + n$ will be about 25 times stronger; there will also be about 300 events from the $\nu + e \rightarrow \nu + e$ neutrino-electron scattering which will be recognized by the direction of the recoil electrons. KamLAND cannot compete with this signal.

The other experiment likely to be in operation will be SNO at Sudbury. That detector is similar in size to KamLAND, but contains heavy water. If and when it is equipped with the neutron detection capability, it will be sensitive to the ν_x neutrinos through the neutral current deuteron disintegration. Thus, SNO will compete with KamLAND's 15.11 MeV γ signal.

A few detectors with liquid scintillators exist, or are being built (MACRO, LVD, BOREXINO). They can all compete with KamLAND in the carbon signal in principle. MACRO is smaller, and has rather poor energy resolution at 15 MeV. BOREXINO will be comparable to KamLAND, but will be considerably smaller. The LVD detector in principle would be a serious competitor, since it was planned to contain 1.8 kt of scintillator. (The projections of supernova rates at LVD basically agree with this writeup [33].) However, only 560 tons of active scintillator are operational.

We then conclude that the target size and composition at KamLAND guarantee unique supernovae observations that will complement the higher statistics of Super-Kamiokande with a number of specific measurements.

2.5 Other Channels Requiring Moderate Backgrounds

Although the reactor oscillation search together with the measurement of terrestrial neutrinos and the detection of possible supernovae will represent the initial core of research at KamLAND, a number of other measurements, requiring modest backgrounds, will also be possible in the first phase of the experiment. These measurements, including hypothetical sources of astrophysics anti-neutrinos, nucleon decay, atmospheric neutrinos, and neutron production by muon spallation in underground detectors are discussed in this section. Although these measurements do not represent the main motivation for KamLAND they will provide an interesting complement to the main core of science for little extra effort.

2.5.1 Solar and Astrophysics Anti-Neutrinos

KamLAND will be the first large detector capable of identifying electron-anti-neutrinos from extraterrestrial sources with very small backgrounds, hence opening an entirely new window for the exploration of unknown phenomena. While for energies below $\simeq 8$ MeV reactor and terrestrial anti-neutrinos will represent a background for this physics, above this energy there are no known sources of $\bar{\nu}$, except for supernovae (discussed elsewhere in this paper) which do not really represent a background since they give short ($\approx$10 s) pulses very seldom in time ($\approx$ 1 every 30 yrs) and atmospheric

neutrinos that also have very small fluxes. The double coincidence scheme used by KamLAND to identify $\bar{\nu}_e$ provides a very effective background rejection, so that the expected instrumental background due to muon-produced neutrons and γ-rays from natural radioactivity and cosmogenic isotopes will amount to less than 0.1 event/day above 8 MeV.

While we cannot speculate here on what surprises Nature may reserve for us in this field, we will analyze briefly the sensitivity of the experiment for a possible $\bar{\nu}_e$ component in the neutrinos arriving from the sun. Since the sun burns hydrogen into helium, the conservation of electric charge and lepton number require that it emits ν_e and not $\bar{\nu}_e$. However, exotic phenomena could transform part of the flux of neutrinos into anti-neutrinos during their trip inside the sun or between the sun and earth. Such conversion could be due to a direct $\nu \to \bar{\nu}$ oscillation a la Pontecorvo, or to hybrid oscillations[34] where a magnetic/flavor transition $\nu_e^l \to \bar{\nu}_\mu^R$ is followed by a flavor oscillation $\bar{\nu}_\mu^R \to \bar{\nu}_e^R$. Alternatively, anti-neutrinos could originate from neutrino decays in matter or in vacuum[35]. While many of these models may not be particularly appealing from a theoretical standpoint, a few of them derive motivation from possible correlations claimed between the periodicity of some solar parameters and the detected neutrino fluxes[36]. Ultimately only experiment can be used to determine which way Nature really works and KamLAND is very well placed to perform decisive tests in this field.

We can compare our sensitivity to $\bar{\nu}_e$ to the present and ultimate sensitivities of SuperKamiokande, as described in[37]. Since a water Čerenkov detector can detect only the positron from the $\bar{\nu}_e$ capture, neutrinos and anti-neutrinos have essentially the same signature. In the case of neutrinos, however, the electron is mostly scattered in a direction parallel to the original neutrino. So, as shown in Figure 12, electrons from solar neutrinos point opposite to the Sun's direction in the sky, while, if there were any anti-neutrinos observed, they would lay together with the continuum of background in the figure.

The best way to search for $\bar{\nu}_e$ in SuperKamiokande data consists in using the fact that, although in the kinematics of the $\bar{\nu}_e + p \to e^+ + n$ the information of the neutrino direction is completely lost, the anti-neutrinos are fully polarized and hence the charged current matrix element prefers slightly to emit the positrons in the direction opposite to the flight direction of the $\bar{\nu}_e$. So, whereas the background is supposed to be completely flat in $cos\theta$ anti-neutrinos would have a slight (10%) slope. This feature is used in [37] to derive a limit on the anti-neutrino flux of $\phi_{\bar{\nu}_e} < 9 \times 10^4 \mathrm{cm}^{-2}\mathrm{s}^{-1}$ at 95%CL for energies above 8.3 MeV. In three years of data-taking this would give, for SuperKamiokande, a 95%CL limit of $\phi_{\bar{\nu}_e} < 3 \times 10^4 \mathrm{cm}^{-2}\mathrm{s}^{-1}$, or about 1% of the solar neutrino flux. The latter flux would produce in KamLAND a clear signal of $\simeq$ 900 events/yr in a region, above 8.3 MeV, where backgrounds for this type of events are expected not to exceed 30 events/yr. Hence in one year we could put a 95%CL upper limit on the antineutrino flux of $\phi_{\bar{\nu}_e} < 3 \times 10^3 \mathrm{cm}^{-2}\mathrm{s}^{-1}$, or 0.1% of the flux of neutrinos from the sun.

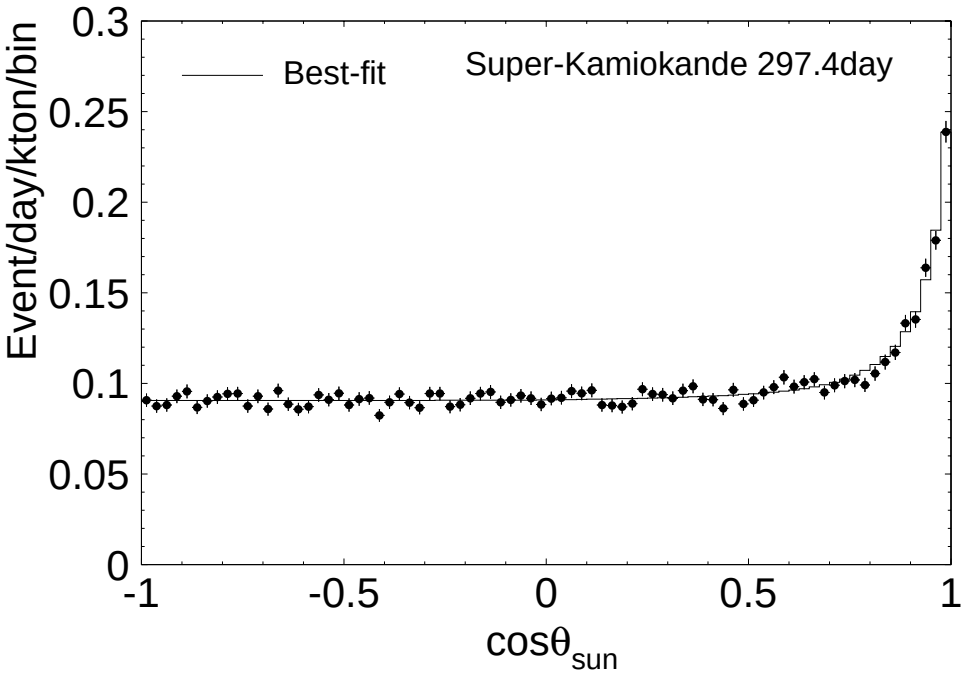

Figure 12: Angular distribution of solar neutrino candidates in SuperKamiokande (from[38]). While the neutrino events point to the sun ($cos\theta \simeq 1$) any anti-neutrino of similar energy would be in the region of continuum dominated by background.

Finally, another possible source of low energy anti-neutrinos could be given by the relics of gravitational collapses of massive stars. Such catastrophic events produced ν and $\bar{\nu}$ that accumulated in the universe. The number of such neutrinos is directly related to the amount of the baryonic matter bound in black holes and neutron stars, and their average energy is expected to be around 15 MeV. Because of the red shift, the energy spectrum carries information on the time distribution of large collapses during the history of our universe. While our ignorance on these parameters makes flux predictions generally uncertain a possible detection would be an extremely exciting feat. Following [39] we assume a constant rate of gravitational collapses and a mean density of matter in the universe of 10^{-31}g/cm^3, thus we would expect to detect about 40 $\bar{\nu}_e$/yr above 8 MeV of energy in our detector. Different flux estimates, for instance[40], give substantially more pessimistic values. We note, however, that since the energy spectrum for these neutrinos is strongly peaked around few MeV, a low energy anti-neutrino detector such as KamLAND compares well with the much larger SuperKamiokande which suffers from a substantially larger "background" from solar neutrinos.

2.5.2 High Multiplicity Physics

One remarkable feature of the KamLAND detector will be its ability to completely reconstruct, with high efficiency, complex events, with non trivial time-sequences of energy depositions, in a very large volume of scintillator. This multihit capability is required for high efficiency detection of neutrons from anti-neutrino capture and supernovae bursts. In this section we will briefly explore the physics signatures that could benefit from this property of our detector associated with its low energy sensitivity. Although the MACRO detector [41] has pioneered a similar multihit technique mainly intended for monopole detection we believe KamLAND is the first detector to apply this feature to a low-threshold, low-background, very-large-volume detector. For sake of concreteness we shall do this with two examples, based on channels that are know or hypothesized by modern particle physics. However one should bear in mind that this exercise is mainly shown to explain the possibility of our experiment and such possibilities would apply to new physics or astrophysics signals as well.

A long sought possible signal for new physics beyond the Standard Model would be the experimental evidence for nucleon instability. As a matter of fact the search for such phenomena, albeit until now unsuccessful, has played a critical role in motivating the first generation of underground detectors. While a large mass (and hence a large number of nucleons) is the first obvious figure of merit for this kind of physics, there are a few signatures that, although very important, are ill-suited for large water Čerenkov detector like SuperKamiokance that has obviously no competition in terms of size. This is the case, for instance, of the "invisible" mode n $\rightarrow \nu\overline{\nu}\nu$ that can only be searched for indirectely, either by detecting neutrinos produced in the whole Earth by such decay [45], or by observing the nuclear relaxation following the

sudden disappearance of a neutron in a nucleus. This last technique was pioneered by Kamiokande [42, 43] that has achieved the present best limit for the mode at $\tau < 4.9 \times 10^{26}$. Unfortunately nuclear relaxation generally proceeds through a multitude of channels (including n, p, α and γ emission) and only relatively high energy γ modes are visible in a water Čerenkov. The fact that the branching ratios to such modes are usually very small ($\approx 5 \times 10^{-5}$ for the case of oxygen in Kamiokande) explains why this mode is so poorly probed.

There are many reasons of principle to think that $n \to \nu\overline{\nu}\nu$ could be a very powerful indicator for new physics [44]. On one hand $n \to \nu\overline{\nu}\nu$ permits baryon-minus-lepton number violation and for this reason it is appealing from a theoretical standpoint, on the other, on more general grounds, such a mode has the largest possible phasespace available and its signature is the most general and inclusive sign for nucleon instability.

KamLAND, even with a mass substantially smaller than SuperKamiokande, will be competitive in the search for this mode, being able to detect low energy γ's as well as heavy particles and, hence, accessing substantially more nuclear relaxation modes. In addition many such relaxation modes have a specific signature in the time sequence of a cascade of processes, so that, by being able to study such sequences one can substantially reduce the background. One possible example is given by the transmutation of $^{12}C \to ^{11}C^*$ due to the disappearance of a neutron. Depending on the state of the disappearing neutron the $^{11}C^*$ nucleus may decay, for instance, to $^{10}C + n + \gamma$ followed by the β^+ decay (in $\simeq$ 20s) of ^{10}C. Although nuclear calculations are still needed (and being performed) in order to understand the sensitivity of this method, it is quite likely that the total branching ratio into modes accessible to KamLAND will be substantially higher than the above 5×10^{-5}. In this way our small (relative to SuperKamiokande !) size will be more than compensated by the "detail" we can see.

In a similar fashion our low energy, multihit capability may complement other detectors in the quest to understand the atmospheric neutrino anomaly. While until recently the study of atmospheric neutrinos has been limited to inclusive final states tagged by a lepton (charged currents, listed in the first three lines of Table 3) recently SuperKamiokande [46] has performed an analysis of modes tagged by a π^0 and no lepton in the final state. Such modes, a fraction of the events in the last two lines of Table 3, are important since, being neutral currents, they are produced by all neutrino flavors and hence give a normalization to the rest of the measurements.

KamLAND will study modes with charged pions or other mesons and, in addition, some of the modes will be detected with very little background, thanks to the tag given by de-excitation of nuclei excited by the neutrino interaction. This technique, analogous to the one used in the detection of supernovae on carbon, will allow us to investigate, with low statistics but greated detail, the atmospheric neutrino anomaly.

Process	ν_e	ν_μ	$\bar{\nu}_e$	$\bar{\nu}_\mu$	Total
$\nu N \to l^\pm N'$	20.9	42.5	6.9	15.0	85.3
$\nu N \to l^\pm N'\pi$	9.1	21.1	3.2	7.5	40.9
$\nu N \to l^\pm N'n\pi$	10.2	26.0	2.4	6.0	44.6
$\nu N \to \nu' N'\pi$	2.9	6.9	1.1	2.6	13.5
$\nu N \to \nu' N'n\pi$	2.6	6.9	0.9	2.5	12.9
Total	45.7	103.4	14.5	33.6	197.2

Table 3: The calculated neutrino event rate per kt×year in Kamioka [47]. Note that this table does not account for the atmospheric neutrino anomaly.

2.5.3 Neutron Production by Muons

The muons penetrating deep underground and interacting with the rock in the vicinity of an underground detector are sources of a significant background. This background is reduced in practical applications by an active veto shield outside the fiducial volume which tracks the most dangerous muons (those close to the fiducial volume), and also eliminates charged particles created by the muon. In addition, the flux of the neutral particles (primarily neutrons) is reduced by the passive buffers surrounding the fiducial volume.

The quantitative description of the muon interaction with the rock deep underground is largely missing. It would be very useful for the whole field of underground physics to obtain data on the different aspects of the problem: a) how many neutrons are produced per muon in different depths, b) what is the energy distribution of these neutrons, and c) what is the angular distribution of the neutron with respect to the muon (muons deep underground are essentially vertical.)

The problem a) above has been addressed in [48]. From this work it appears that the number of neutrons per muon increases approximately as the square root of depth,

$$N_{\rm n} \simeq 10^{-5}\sqrt{D}\ . \tag{12}$$

Where $N_{\rm n}$ is the neutron production probability in neutrons/(muon g/cm^2) and D is the depth in mwe. This result has been independently verified only at shallow depth [49], and an attempt to understand neutron production theoretically underestimates the rate by a factor of few at shallow depth [50] and by a bigger factor at larger depths. That suggests that the neutron production is a more complicated process, in which a sizable multiplication through a cascade mechanism takes place. There is very little direct information on the problems b) and c) despite their obvious practical importance. It would be important to investigate these phenomena with a detector large enough that its neutron efficiency be essentially independent of energy and KamLAND is ideally suited for this task.

In KamLAND, at a depth of 2700 mwe the muon flux is about $10^{-3}\mu/(\mathrm{m}^2\ \mathrm{s})$. The muon rate through the whole detector is about 0.3 Hz, of which approximately half goes through the active scintillator volume and the veto, and the other half goes only through the veto and the inert buffer. Since events with the muon traversing the active scintillator will be dominated by the very large muon energy deposition, we are planning to use the second category of events for our neutron spallation measurement. Using the formula above and keeping into account the density of fluids inside the detector, we conclude that the veto and the inert buffer produce about 0.1 Hz of neutrons by muon spallation. Although detailed MC simulation, with the correct energy and angular distribution, will eventually be needed to accurately describe the fate of these neutrons, it is safe to assume that a fraction of them of order 50% will penetrate into the active scintillator volume, be moderated and eventually captured. A simple dedicated trigger will accept and tag a fraction of the events in which muons go through the veto, allowing us to accurately test the various scenarios of the muon spallation.

Neutrons entering the scintillator will cause two kinds of signals: a prompt signal will be produced by proton recoils in the moderation process and a delayed signal from the neutron capture. The total energy in this first part of the event will give an estimate of the neutron energy, as a very large part of such energy will be deposited in this kind of processes. Finally the delayed capture signal will serve as a signature to distinguish neutrons from e.g. γs.

A rudimentary program along these lines has been recently carried out by the Soudan-2 collaboration [51]. There, contained events with the hits in the veto shield were analyzed. Some of the events (called showers) were consistent with gammas with the conversion length of about 15 cm. Other events (called tracks) were consistent with neutrons. The distance from the wall where about half of the neutrons is stopped is close to 60 cm. Taking into account the average density of 1.6 $\mathrm{g/cm}^3$ in Soudan-2 one arrives at the average neutron energy of several hundred MeV. While this crude measurement clearly shows the feasibility of such a measurement, KamLAND will be able to extract solid numbers that will benefit the entire community of underground detectors.

2.6 Future Ultra-Low Background Physics Potential

The physics considered up to this point represents a set of important measurements that can be performed by KamLAND with existing technology and, in a rather short time, will allow us to qualitatively improve our knowledge in a number of fields spanning particle physics, astrophysics and geophysics. While the relatively modest background requirements for this phase will ensure that this physics will be performed from the beginning of the experiment's life, other physics, involving single ionization events, and hence requiring substantially lower backgrounds, will be possible in a second phase of the experiment.

Although the first phase of KamLAND will by itself fully reward our efforts, we believe it is important to start exploring from the beginning the potential and detector requirements for a second phase. As will be shown in later sections the dominant backgrounds in such a large homogeneous detector derive from natural radioactivity internal to the scintillator, once reasonable efforts are made to select materials for the outside components. It is worth mentioning here that in this respect a larger size detector not only gives higher signal rates, but it allows also to further suppress external backgrounds, so that the quest for low contamination can be more safely restricted to the bulk of the scintillator fluid and to the radon suppression system. While our early study of very low background physics will ensure that appropriate precautions are taken to select low activity external components, we believe that the scintillator purity requirements for the second phase are so extraordinary that one can understand the limitations only by studying a full-size (or close to full-size) volume. In this respect the staged approach of KamLAND will be extremely powerful since, contrary to other experiments, this purity study will be performed in the full-size configuration while measuring first-rate physics. Hence, from the results of the first phase of the experiment we will decide what level upgrade of the scintillator will be needed to perform the second phase of the experiment. This approach will allow us to move towards the ultra-low background phase in a gradual fashion, committing resources to the project in a measure commensurate to the need.

At present we have identified two types of physics to be performed in the ultra-low background phase: solar neutrino detection and the search for neutrinoless double-beta decay. We will discuss these topics in the rest of this section.

2.6.1 Solar Neutrinos

Status of the Solar Neutrino Puzzle

The Sun produces an intense flux of electron neutrinos as a consequence of the fusion reactions generating solar energy, with the combined effect

$$4p + 2e^- \rightarrow {}^4\mathrm{He} + 2\nu_e + 26.73 \text{ MeV} - E_\nu \ , \tag{13}$$

where E_ν is the neutrino energy ($\langle E_\nu \rangle \simeq 0.6$ MeV). The solar neutrino spectrum consists of several components; the expected flux according to the Standard Solar Model (SSM) of [52] is shown in Figure 13. Observation of solar neutrinos tests directly the SSM, and more generally the theory of stellar evolution and structure. At the same time, it offers an important opportunity to investigate neutrino properties.

So far, five experiments published results on solar neutrino measurements, and the signal in all of them is less than the expectation. Radiochemical experiments (^{37}Cl at Homestake, threshold 814 keV; ^{71}Ga at Gran Sasso, and ^{71}Ga at Baksan, threshold 233 keV) use neutrino capture on the indicated nuclear targets to produce radioactive daughter nuclei, which are extracted and counted after exposure to solar neutrinos.

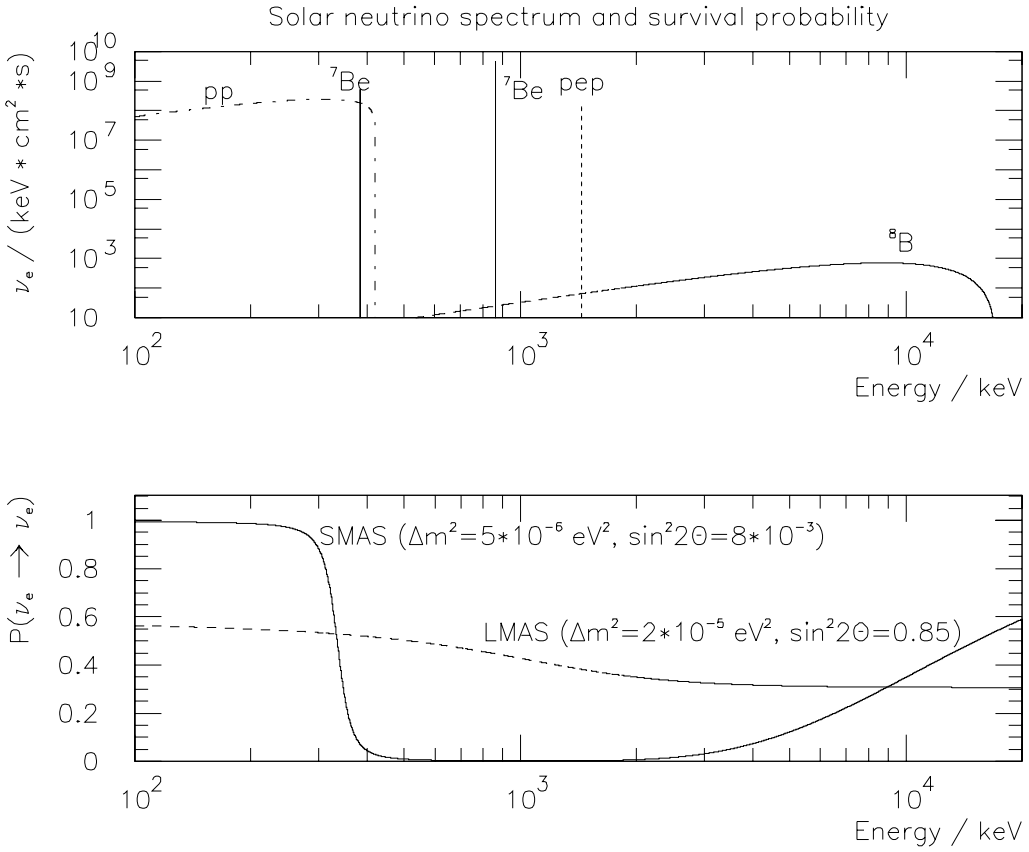

Figure 13: The upper part depicts the most important components of the solar ν_e spectrum, normalized to the flux given by the SSM. For the continuous sources the flux is given per keV. The lower part shows the neutrino survival probability for matter-enhanced neutrino oscillations.

Radiochemical experiments measure the solar neutrino flux above their respective thresholds (weighted with the energy dependence of the corresponding cross section) and so they can deduce the contribution of the individual components of the solar neutrino spectrum only indirectly. The other two experiments are real-time measurements of the electron recoil spectra caused by the $\nu - e$ scattering (Kamiokande and Super-Kamiokande). Due to their relatively high threshold these experiments observe only the high energy part of ^{8}B neutrinos.

While these experiments have convincingly shown that the Sun indeed is a source of electron neutrinos, and that the corresponding flux has the correct order of magnitude, there is a consensus that a consistent explanation of all observations is very difficult, if not impossible, in the framework of the SSM. From the Kamiokande and Super-Kamiokande measurement one is able to determine the ^{8}B flux. Combining it with the Homestake result leaves no room to accommodate the ^{7}Be solar neutrinos. This makes an astrophysical solution untenable, because ^{8}B nuclei are produced from ^{7}Be in the Sun. A similar conclusion can be reached using the ^{71}Ga measurements. Since the pp neutrino flux is essentially determined by the known solar luminosity, the ^{71}Ga measurements again leave no room for the ^{7}Be neutrinos which are expected to contribute significantly to the ^{71}Ga signal.

Thus one is led to the conclusion that:

- experiments indicate a strong suppression of the ^{7}Be solar neutrino flux,
- the observations are incompatible not only with the SSM, but also with most of its non-standard modifications.

In view of the above, it is attractive to invoke explanations based on neutrino oscillations. In particular, assuming the MSW effect to take place, one can account for all observations by assigning to the fundamental parameters Δm^2 and $sin^2 2\theta$ values in either one of the two regions shown in Figure 2. These two possibilities are usually referred to as large mixing angle solution (LMAS), and small mixing angle solution (SMAS). The corresponding survival probabilities, calculated using the Landau-Zener approximation [53], is depicted in the lower part of Figure 13.

As explained elsewhere in this proposal, the KamLAND experiment will directly test the LMAS solution of the solar neutrino puzzle with a laboratory-style measurement of reactor neutrinos. At the same time KamLAND may also complement such unique measurements with the direct and independent observation of the ^{7}Be component of the solar neutrino spectrum.

Solar Neutrinos at KamLAND

Should neutrino oscillations be discovered by KamLAND in its first period of data-taking an independent verification would be very important. On the other hand, should the reactor neutrino search yield a negative result, a measurement of the solar

neutrino flux and spectrum, as predicted by the SSM [52], would be needed to determine whether the missing solar neutrino flux is due to the SMAS or to other causes, like for instance problems in the SSM. Hence a measurement of the solar neutrino spectrum would, in any case, constitute a natural continuation of the KamLAND.

Solar neutrinos interacting with the electrons in the scintillator will scatter and the resulting recoil energy can be detected. The corresponding cross section is given by:

$$\frac{\mathrm{d}\sigma_{\nu-e}}{\mathrm{d}T} = \frac{G_F^2 m_e (\hbar c)^2}{2\pi}\left[(g_V - g_A)^2 + (g_V + g_A)^2\left(1 - \frac{T}{E_\nu}\right)^2 + (g_A^2 - g_V^2)\frac{m_e T}{E_\nu^2}\right] \ . \quad (14)$$

Here $g_V = 2\sin^2\theta_W \pm 1/2$, $g_A = \mp 1/2$ (the Weinberg angle $\sin^2\theta_W = 0.231$), and the upper sign is used for ν_e while the lower sign is used for the other flavors. For the anti-neutrinos one must make the substitution $g_V \leftrightarrow g_A$.

The electron recoil kinetic energy T is restricted from above by

$$T_{max} = \frac{2E_\nu^2}{2E_\nu + m_e} \ . \quad (15)$$

This reaction does not allow a direct measurement of the neutrino spectrum and, for instance, the discrete ^{7}Be spectrum would give rise to recoil electrons characterized by a sharp edge at T_{max}. In order to calculate the total number of events, we convolute Eq. 14 with the corresponding spectrum from the SSM [52]. The total expected rate is obtained by integrating over T and multiplying by the number of target electrons (for 1kt of scintillator we use 3.4×10^{32} electrons). The result is shown in Table 4 for the most important components of the solar neutrino spectrum.

ν source	SSM flux (10^8cm^{-2}s^{-1})	T_{max} (MeV)	events (1/kt·day)
pp	591	0.25	2033
^{7}Be	51.5	0.66	841
pep	1.4	1.22	46
^{8}B	0.066	13.7	16

Table 4: Expected rates in KamLAND for the most important components of SSM neutrino fluxes

As shown in Table 4 we expect a substantial solar neutrino event rate in KamLAND, by far exceeding that of the reactor neutrino experiment. However, the above reaction offers no experimental signature which would allow us to discriminate against background on an event-by-event basis. The few hundred keV solar neutrino signal is well within the energy range of natural and man-made radioactivity. Such calorimetric approach hence requires the reduction of the radioactivity content to a level which will allow a statistical unfolding of the background from the measured spectrum.

In the following we compare the solar neutrino spectra with the expected backgrounds for KamLAND. While more general background calculations are given elsewhere in this report, here we summarize the assumptions relevant for solar neutrino physics and present the resulting backgrounds in a way appropriate for the purpose. We assume the backgrounds to be dominated by internal activities. This is obtained by carefully selecting the external materials and especially by having a very large buffer layer that here is increased by 1 m with a fiducial volume cut that retains 615 tons of target. The U/Th concentration in the scintillator for this measurement are assumed not to exceed 10^{-16} g/g ($1.2{\cdot}10^{-3}$ and $4.1{\cdot}10^{-4}$ Bq/kt, respectively). The Rn concentration in the scintillator is assumed 1 μBq/m^3 or less ($1.3 \cdot 10^{-3}$ Bq/kt). The ^{40}K content is assumed to be better than 10^{-18} g/g ($3.1 \cdot 10^{-4}$ Bq/kt) and the ratio ^{14}C/^{12}C=10^{-18} (163 Bq/kt). These purity levels, that we will not need for the first phase of our physics program, are equivalent to the ones required by the BOREXINO collaboration. Finally, as shown below, the ^{7}Be (^{11}C) production rate by cosmic-ray muons in Kamioka is $\simeq 400$ kt^{-1} day^{-1} (< 3000 kt^{-1} day^{-1}).

As can be seen from Fig. 14, in the energy window 280-800 keV, the ν signal is dominated by the ^{7}Be solar neutrinos. Such region offers the most advantageous signal to background ratio. In table 5 we list the event rate in this counting interval for the various oscillation scenarios. While the full flux of the SSM would result in a signal to background ratio of 1, the two neutrino oscillation scenarios would correspond to a strongly suppressed neutrino rate.

Source	Rate (280-800 keV) [Counts/(kt day)]	
	$\nu_e \to \nu_{\mu,\tau}$	$\nu_e \to \nu_s$
SSM	466	
LMAS	241	207
SMAS	63	2
Background	544	

Table 5: Event rates in the energy interval 280-800 keV. ν_s denotes sterile neutrinos.

Since there is obviously no possibility to measure the background without the presence of the signal, alternative methods have to be envisaged to accurately infer the background rate. The most crucial U/Th and Rn contribution would be determined through Bi-Po $\alpha - \beta$ coincidences. In case of U/Rn the ^{214}Bi β-decay is quickly followed by the ^{214}Po α-decay ($T_{1/2} = 162\mu$s). The ^{212}Bi-^{212}Po pair in the Th decay series has a correlation time of $T_{1/2} = 0.3\mu$s. A tagged background sample would also give the measured spectral shape of these components. This technique should be complemented by a high sensitivity neutron activation analysis (NAA) to test for a broken secular equilibrium. The analysis of the spectral shape at higher energies

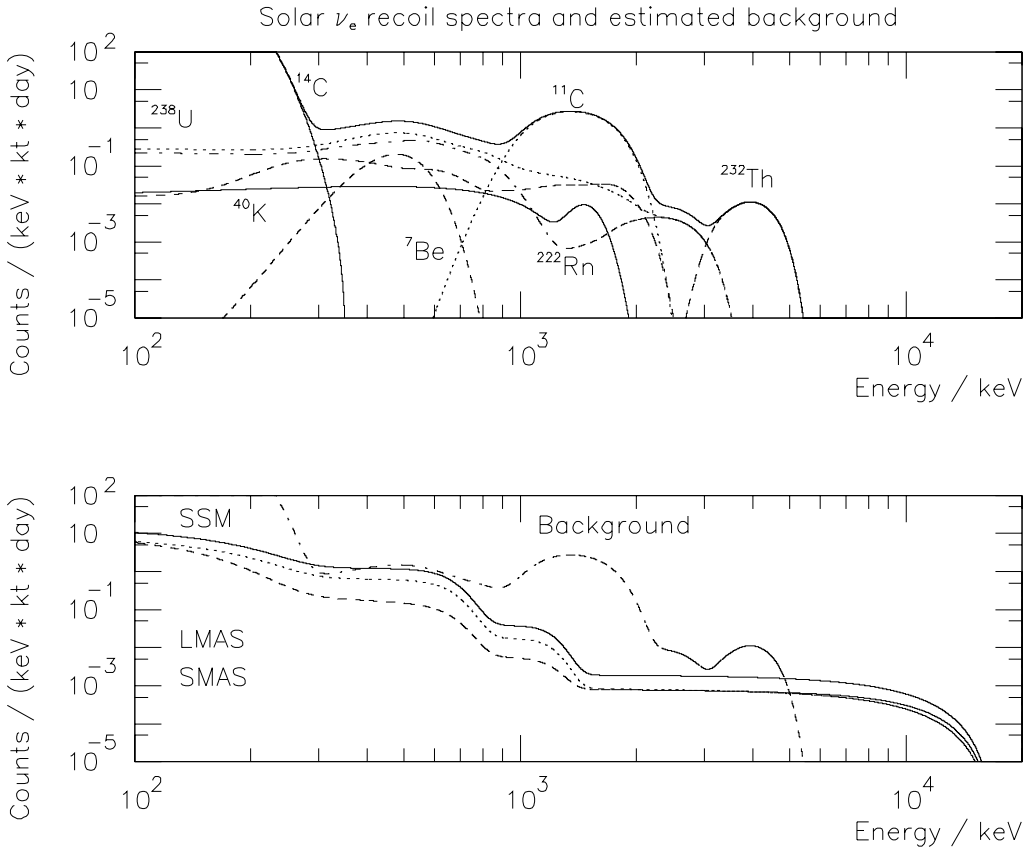

Figure 14: Signal and background for solar neutrinos in KamLAND. The upper part depicts a decomposition of the calculated background spectrum. To reflect the large detector size β and γ energies were added coherently. The quenched alpha component was added statistically. The lower portion shows the solar neutrino recoil spectrum with and without the presence of neutrino oscillations. All spectra are folded with a resolution $\sigma(E)/E = 10\%/\sqrt{E}$ (MeV)

would constrain this determination by normalizing a Monte Carlo background model. The ^{40}K activity would also be determined through NAA. The ^{7}Be production rate would be determined independently e.g. by exposing scintillator to an energetic muon beam. If we assume that the background subtraction could be done with 10% systematic uncertainty then we can estimate the power of our analysis with regards to the event rates given in Table 5. Due to the large rates the statistical uncertainty would soon be negligible. Under these assumptions the full SSM signal would have a significance of $8.5 \cdot \sigma$ after one year of data taking. The LMAS and the SMAS would have $4.3 \cdot \sigma$ and $1.1 \cdot \sigma$ significance, respectively. The LMAS flux would differ from the SSM expectation by $4 \cdot \sigma$ after a year while the SMAS would correspond to a null result. Even if neutrino oscillations would not be discovered a 10% determination of the solar ^{7}Be flux would be an important result, greatly enhancing our understanding of the stellar energy production.

Other Experiments

The existing radio-chemical experiments have only a limited sensitivity for ^{7}Be neutrinos. Their inclusive flux measurements do not allow to unfold the contributions of the different solar neutrino species. The fact that the Cl and Ga experiments have different reaction threshold energies and hence different contributions from different neutrino species puts however a strong constraint on the allowed ^{7}Be flux as explained above. SuperKamiokande and SNO are only sensitive to the energetic ^{8}B neutrinos. Due to the fact that SuperKamiokande has a factor 50 larger volume than KamLAND, however, we will not be able to compete in the field of energetic solar neutrinos. Due to the strong temperature dependence of the solar ^{8}B flux, this component is most vulnerable to a fine tuning of the solar models and an independent measurement of the ^{7}Be flux would be extremely important. The BOREXINO experiment, being build in the Italian Gran Sasso laboratory, also plans to measure the ^{7}Be solar neutrino flux via neutrino electron scattering using a liquid scintillator. The fiducial volume of this detector is 100 tons, much smaller than in the KamLAND case. The BOREXINO collaboration has pioneered the field of large volume ultra-low-background scintillators and demonstrated that such endeavor is indeed feasible. Their detector is also under construction and it can be expected that they will start data taking by 2001. Although the measurement of solar neutrinos is not the first priority in KamLAND, the time scale of our experiment is such that we could probably be competitive in this physics, providing an independent measurement that would be invaluable in such a difficult field. In fact, since KamLAND is much larger than BOREXINO, external backgrounds are further suppressed and possibly, if surface effects dominate the scintillator purity (like for dust contamination on the balloon), also internal backgrounds will be lower. To maintain this option viable KamLAND is devoting special attention to closely monitor all detector components for their radioactivity content.

2.6.2 Double Beta Decay with KamLAND

The investigation of the neutrinoless double beta ($\beta\beta0\nu$) decay is at present the most sensitive probe for a Majorana neutrino mass. As the various neutrino oscillation experiments can only determine the mass difference between different flavors, a degenerate neutrino mass pattern would still allow arbitrarily large masses. The extraordinary mass sensitivity of $\beta\beta0\nu$ could be crucial to establish the absolute neutrino mass scale, should neutrinos be Majorana particles. The most competitive limit obtained through this technique thus far is $\langle m_\nu \rangle < 0.5$ - 1.0 eV [54].

This section will discuss the potential of the KamLAND detector for a future $\beta\beta0\nu$ experiment, and define the requirements in terms of scintillator purity and isotope loading.

The B-L number violating $\beta\beta0\nu$-decay requires massive Majorana neutrinos and hence the existence of physics beyond the Standard Model. The decay rate $(T^{0\nu}_{1/2})^{-1}$ is given by (neglecting right-handed admixtures to the weak interaction):

$$(T^{0\nu}_{1/2})^{-1} = F^{0\nu} \cdot |M^{0\nu}|^2 \cdot (\frac{\langle m_\nu \rangle}{m_e})^2, \tag{16}$$

with $F^{0\nu}$ the phase space integral, $M^{0\nu}$ the nuclear matrix element, m_e the electron mass and $\langle m_\nu \rangle$ the effective Majorana neutrino mass. The effective mass is defined as:

$$\langle m_\nu \rangle = \sum_i m_i \cdot U^2_{ei} \tag{17}$$

where m_i denotes the mass of the eigenstate i and U_{ei} the mixing matrix element containing a CP eigenvalue (which can lead to destructive interference). A measured $\beta\beta0\nu$ decay rate or a limit for it allows hence to draw conclusions on the Majorana neutrino mass, once the appropriate nuclear matrix elements are calculated. The allowed $\beta\beta2\nu$-decay has been observed for 12 nuclides so far. The measured decay rates serve as an implicit verification of the nuclear structure calculations required. Agreement between measured and calculated decay rates is generally good. In this chapter we will use nuclear matrix element calculations of [55] in our rate estimates, as this theoretical model covers almost all double-beta emitters.

To search for $\beta\beta0\nu$-decay with the KamLAND detector we would need to dissolve a large quantity of a $\beta\beta$ unstable isotope in the liquid scintillator. This will allow a calorimetric measurement of the sum energy of the emitted electrons as proposed in [56]. Like for the detection of solar neutrinos in this approach $\beta\beta$-decays have no specific signature which would allow to suppress backgrounds. The two main experimental difficulties to be addressed are:

- The comparably low abundance of the decaying isotopes in the detector requires very low radioactivity concentrations in the liquid scintillator.

- The relatively poor energy resolution of liquid scintillator will scatter $\beta\beta 2\nu$-events into the analysis energy window of the $\beta\beta 0\nu$-mode thus increasing the irreducible background.

Despite these inherent difficulties the KamLAND detector does allow the use of ton quantities of $\beta\beta$-emitters to be compared to kilograms (of highly enriched ^{76}Ge) in todays most sensitive experiment. This gain of almost three orders of magnitude in source strength might allow for the first time the exploration of Majorana neutrino masses below 0.1 eV. An additional advantage of KamLAND would be that most of the background could be measured before the scintillator is loaded with the double-beta emitter. If an effect would be observed with one double-beta emitter the measurement could be repeated by loading with a different isotope. In order to alleviate the two limitations described scintillators with high loading and large light yield are essential. In our estimates we use $\sigma(E)/E = 10\% \cdot /\sqrt{E}$. In the following we will also use the same background model as in the solar neutrino section.

From all double beta emitters which have been considered for this estimate, ^{136}Xe is the most promising candidate. The noble gas Xe dissolves to up to 2% by weight in various organic solvents as benzene, cyclohexane, hexane, 2-methylheptane and dodecane [57]. In our estimate we will conservatively use a 1% concentration. We are planning to perform tests in our laboratories to determine what effect such concentrations have on light yield, transparency and stability of the scintillator. Although Xe has no radioactive isotopes, contaminations with radio active noble gases i.e. ^{85}Kr ($T_{1/2}$=10.7 y, Q_β=0.69 MeV, fission product) and ^{42}Ar ($T_{1/2}$=33 y, Q_β=3.52 MeV, atmospheric spallation) have to be carefully studied. The Caltech-Neuchatel-PSI double-beta experiment using enriched Xe gas in a TPC measures a U/Th concentration of 10^{-12} g/g in their counting gas using $\alpha - \beta$-coincidences [58]. In KamLAND we would need at least a factor 100 better Xe purity that could possibly be achieved by distillation since the three gases have quite different boiling points. The Caltech-Neuchatel-PSI TPC could probably be used in a not-too-far future to test Xe samples for radioactive contamination.

Since Xe is a gas at STP it is relatively easy to enrich isotopically by means of centrifugation. We have started to explore this possibility with the Kurchatov Institute in Russia and found that the quantities of isotope required, although very large, are not beyond the capacity of their facilities. This option will be further discussed in the future. In our estimate we will present both the case of natural Xe (8.9% ^{136}Xe) and Xe enriched to 89% ^{136}Xe.

Calculations predict a rate of $\beta\beta 2\nu$-event as high as 0.02 and 0.2 s^{-1} for the two isotopic compositions. A Majorana neutrino mass of $\langle m_\nu \rangle = 0.1$ eV would give a $\beta\beta 0\nu$-event rate of 12 and 122 events/year in the two cases. This very small signal rate defines the background requirements.

We use $[Q_{\beta\beta}, Q_{\beta\beta}+2\cdot\sigma]$ as analysis interval I for the $\beta\beta 0\nu$-decay. This asymmetric interval reduces the $\beta\beta 2\nu$ irreducible background to reasonable levels yet maintaining an efficiency of 48% for the signal. Since the dominant source of background in I

Component	Low reduction		High reduction	
	Xe^{nat} $[d^{-1}]$	Xe^{enr} $[d^{-1}]$	Xe^{nat} $[d^{-1}]$	Xe^{enr} $[d^{-1}]$
$\beta\beta 2\nu$	0.028	0.28	0.028	0.28
^{232}Th	$4 \cdot 10^{-3}$	$4 \cdot 10^{-3}$	$4 \cdot 10^{-3}$	$4 \cdot 10^{-3}$
^{238}U	1	1	0.2	0.2
^{222}Rn	1	1	0.2	0.2
^{40}K	0	0	0	0
Σ $[d^{-1}]$	2.1	2.3	0.44	0.69
$N_{\beta\beta 0\nu}$ ($\varepsilon = 0.48$) $[y^{-1}]$	73	78	33	42
$T^{0\nu}_{1/2}$ [y]	$3.7 \cdot 10^{25}$	$3.5 \cdot 10^{26}$	$8.1 \cdot 10^{25}$	$6.4 \cdot 10^{26}$
$\langle m_\nu \rangle$ [eV]	0.24	0.08	0.17	0.06

Table 6: Background rates and neutrino mass sensitivity achievable with 10 tons of natural or enriched (89% ^{136}Xe) (1% loading). The estimate is done for the "high purity" scintillator model defined in the previous section. The two left columns contain our estimate for a ^{214}Bi reduction factor of 20 ("low reduction"), while for the right two columns a reduction factor of 100 ("high reduction") was assumed to account for $\alpha - \beta$-tagging. The line "$N_{\beta\beta 0\nu}$" denotes the limit on the counting rate that one can extract from the background. $T^{0\nu}_{1/2}$ and $\langle m_\nu \rangle$ are then derived from these counting rates. Nuclear matrix elements of [55] are used.

is ^{214}Bi from ^{222}Rn and ^{238}U in the scintillator, the achievable sensitivity strongly depends on our assumption on the tagging efficiency for the ^{214}Bi-^{214}Po sequence. Assuming such tagging efficiency to be 95% (99%) we obtain the "Low reduction" ("High reduction") result summarized in Table 6. We believe that such reduction factors are quite reasonable for such a short time sequence.

It is worthwhile to mention that among the running double-β decay experiments the largest source is $\sim$10 kg of isotopically enriched ^{76}Ge [54]. This experiment, performed in the Gran Sasso underground laboratory in Italy, plans to reach a neutrino mass limit of about 0.2 eV within few years from now. The French-Russian-US NEMO project in the Frejus tunnel is in an advanced stage of preparation and will reach a sensitivity comparable to the Ge project mentioned above.

Several dedicated, very complex and expensive double-β decay experiments could handle sources of the size discussed for KamLAND. Particularly interesting are a much larger ^{76}Ge experiment at Gran Sasso ("GENIUS" [59]) and a cryogenic ^{130}Te search [60] also to be performed at Gran Sasso. Besides the acquisition of the costly enriched source material both these project require a substantial effort to build a large detector of complexity and cost comparable to our detector. In KamLAND's high purity phase we would only need to worry about the double-β source.

Our conclusion is that KamLAND in the future could be a competitive detector for

a double-beta decay search. Although it is obvious that this physics is not within the reach of a first phase of the experiment, the possibility of reaching 60 meV neutrino mass sensitivity strongly motivates the collaboration to study further the possibility of performing this type of measurements in some future. As stated above we expect to collect a wealth of information on the possible backgrounds and problems connected with double-beta decay while running the first phase of the experiment.

2.7 Summary of Physics at KamLAND

As shown above, KamLAND represents a qualitative step forward in the growing field of non-accelerator experiments. The presence of a scintillation detector with an unprecedented size and a low threshold at the Kamioka site will allow us to address a very diverse and crucial set of scientific measurements. While in a first phase, scheduled to begin before the end of the century, we will concentrate on topics that are within the reach of the present technology, a second phase will push the internal backgrounds to the minimum, opening the way to the exploration of a whole new range of phenomena.

The physics to be studied in the first phase will be characterized by temporal correlation in the physics events that will provide clear signatures and greatly suppress backgrounds. The search for very small neutrino mass differences in a ultra-long baseline reactor oscillation experiment; the measurement, for the first time, of anti-neutrinos produced by radioactive decays in the Earth's lithosphere and the detailed study of supernova dynamics and neutrino physics in the event of a supernova explosion, will represent the main focus of the first phase. At the same time KamLAND will also be performing unique measurements involving the search for non-terrestrial anti-neutrinos, nucleon decay, atmospheric neutrinos and neutron production by cosmic muon spallation underground.

This important science will be complemented, in a second phase, by the ability to study solar neutrinos and possibly to search for neutrinoless double beta decay in very large quantities of isotopes.

3 Backgrounds

Backgrounds for physics measurements at KamLAND are produced by cosmic-muon-induced processes and natural radioactivity. To study such backgrounds quantitatively we have performed a full Monte Carlo simulation using GEANT [61] for the detector geometry, materials and the electromagnetic interactions between particles and the detector materials; FLUKA [62] for hadronic interactions and GCALOR [63] for low energy neutron transport.

Schematically there are two types of physics signatures interesting for Kamland, involving double events and single events. While a detailed description of the physics signals and goals for KamLAND is given in previous sections, here we briefly review the properties of such signals and the features that distinguish them from backgrounds.

- Double events are typical for anti-neutrino detection and supernova neutrino scattering on carbon. As an example the signature for reactor anti-neutrinos consists of a prompt part for the positron and a delayed part for neutron capture. We require a minimum 1 MeV energy deposit for the prompt part and 1.8-2.7 MeV energy deposit for the delayed part (a 3σ cut for 2.2 MeV neutron capture signal). We require the delayed part of the event to happen 10-500 μs later. In addition, the neutron capture is required to be within 1 m from the vertex of the positron. The Monte Carlo simulation shows that, given the small kinetic energy for these neutron ($\sim$ 100 keV), such a cut retains more than 99% of signal events.

- Singles events, for instance from low energy neutrino scattering on electrons, are selected by only requiring a minimum energy deposition of 1 MeV.

In the following we shall analyze in detail the absolute values and relative importance of different backgrounds.

3.1 Background from Cosmic Ray Events

There are two types of background induced by cosmic muons: prompt neutrons from muon capture or muon spallation, and radioactive isotopes produced by cosmic ray activation. Since for this second class of events the decay may happen with a substantial delay with respect to the cosmic ray occurrence, vetoing is often hard or impossible. For this reason we will describe this source of background separately from the prompt neutrons. It is very important to realize that cosmogenic activation never results in a background for the first phase of our experiment, rather this first period of data-taking will be ideal to experimentally study the possible problems related with a low energy single trigger.

3.1.1 Background from Prompt Neutrons

Although there are two different neutron generating processes, muon capture and muon spallation, neutrons from the second process are more energetic and hence more dangerous. Therefore in the following study we concentrate only on the background from muon spallation. Although the details of the spallation process are not well known, the main process involved, which gives the hardest neutrons, is shown in Figure 15.

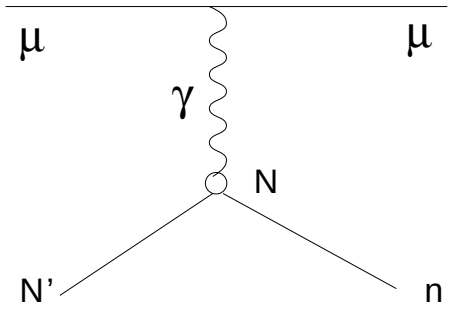

Figure 15: Cosmic-ray muon spallation process.

The total muon rate at the KamLAND site, 2700 mwe below ground, is about 5×10^{-8} cm^{-2}sr^{-1}s^{-1} [66], giving a rate of 0.3 Hz over the whole volume of the detector, as measured by Kamiokande [68]. The energy distribution of muons at KamLAND is flat from 0-100 GeV and then drops exponentially [74]. The angular distribution is given by the details of muon production in the atmosphere and their subsequent attenuation in both atmosphere and rock. At the Kamioka observatory such distribution is well approximated by a $\cos^2\theta$ distribution.

The number of neutrons produced by muons have been measured by several underground experiments [48]. Using their measurement, a total of 4×10^{-4} n/($\mu \cdot$g$\cdot$cm^{-2}) are produced at 2700 mwe. Since cosmic muons can be detected by the veto counter, we should only consider muons passing through the rock and generating neutrons there. We assume that a shell of rock of 1 m thickness contributes to such neutron production. This corresponds to a total active volume of 1.9×10^9 cm^3 producing 1.3×10^4 untagged neutrons per day (at a rock density of 2.7 g/cm^3).

Since the energy spectrum of these neutrons is not well understood we conservatively assume that all neutrons have the hard spectrum deriving from the process shown in Fig. 15. This gives an exponential behavior that can be fitted to $E_{\rm n}^{-1.86}$ as measured by several experiments [64]. The angular distribution is obtained from [65].

Using all the information above, we generated half a million neutron background events in our detector (corresponding to about 40 days of data-taking). By requiring an energy deposition of at least 1 MeV only 3 events/day are retained. This background of singles is negligible with respect to the natural radioactivity background

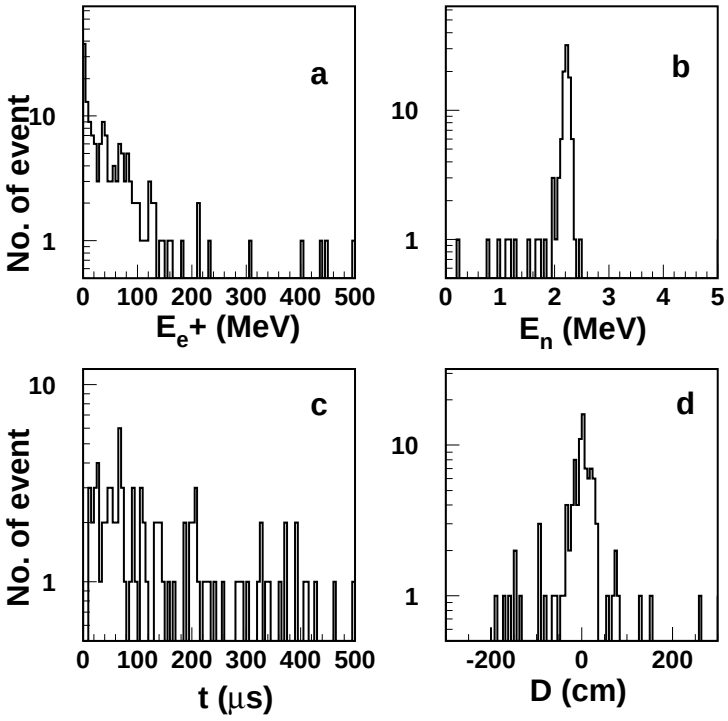

Figure 16: Simulation of cosmic muon-induced fast neutron in KamLAND. a: Energy distribution of the prompt part (fake positron); b: Energy distribution of the delayed part (neutron capture); c: time difference between prompt and delayed part; d: vertex difference between prompt and delays part.

described below. For double correlated events we apply the cuts described above and retain only 0.07 events/day, with a signature consistent with anti-neutrinos. This is to be compared to 2 events/day of signal from the reactors. For energy cuts optimized for the region of interest for terrestrial anti-neutrinos this background becomes about 0.01 events/day, an order of magnitude below the expected signal.

We conclude that cosmic-ray induced neutrons do not limit the ability to do physics at KamLAND. In Figure 16 we show, as an example, some of the variables of interest for the neutron background suppression as detected in KamLAND. Only pairs of events with energy in both the prompt and the delayed parts are plotted.

3.1.2 Background from Cosmogenic Activation

Nuclei in the scintillator materials can be excited by capturing a muon/neutron, or through muon/neutron spallation. The excited nucleus will quickly ($<$ ns) de-excite by emitting γ, neutron, proton or α, plus another nucleus which could be a radioactive isotope with lifetime from milliseconds to years. Depending on the magnitude of the lifetime involved this kind of background may or may not be reduced by using the cosmic ray veto signal. In our study we will assume the scintillator composition given below (80% Isoparaffine ($\simeq$ nCH_2), 20% Pseudocumene (C_9H_{12}) and 2g/l PPO ($C_{15}H_{11}NO$)). Since the mass of ^{14}N and ^{16}O is only 0.02% of that of the proton and carbon, we will neglect them in the following discussions.

- *Activation by neutron capture:* The total number of neutrons produced from muon spallation in the scintillator is 3000 per day using the same method as in the previous section. While most of neutrons capture on protons and, to a lesser extent on ^{12}C resulting in stable isotopes (^2H and ^{13}C), a very small fraction of them are captured on ^{13}C (about 1% of natural carbon), giving the radioactive ^{14}C. Since the capture cross section on ^{13}C is 0.2% of that on proton, and the number of ^{13}C is 0.5% of that of protons, the total number of ^{14}C produced will be 0.03 per day that represents a negligible background. From extensive studies conducted by the BOREXINO-collaboration[70] it is known that activation of ^{13}C during the scintillator production does not result in dangerous backgrounds.

- *Activation by neutron spallation:* Neutron spallation can produce many radioactive isotopes according to the reaction $N + n \rightarrow h + N'$ where h can be a neutron, proton, γ, α or π. While the prompt production of h is well described by intra-nuclear cascade plus evaporation models [69] which have been incorporated in FLUKA, more interesting for us is the understanding of the nuclear component N' that is not theoretically well understood. Hence to study these cases of activation we use the production cross sections measured in[71] and shown in Table 7.

  The number of nuclei produced per unit time is estimated by rescaling the correspondent number for elastic scattering with the appropriate measured cross

Isotopes	Life Time (s)	cross section (mb)	No. day^{-1}	background day^{-1}
^{12}B	0.02	30 [72]	< 1700	< 1700
^{11}C	1218	28.7 [71]	< 1700	< 1700
^{10}C	19.3	1.1 [71]	< 65	< 65
^{10}Be	1.5×10^6 y	2.5 [71]	<150	0
^{7}Be	53.28 d	7.1 [71]	<409	0

Table 7: Background estimate from activation by neutron spallation.

section. This can be expressed by

$$N_{\text{reaction}} = \frac{\sigma_{\text{reaction}}}{\sigma_{\text{elastic}}} * N_{\text{collision}} * N_{\text{neutron}}.$$

Since all the reactions considered have a threshold $E_f \approx 10$MeV for the energy of the neutron and above this energy the elastic cross section on carbon is an order of magnitude larger than that on protons, we can conservatively assume that the entire thermalization process happens on carbon, with elastic cross section $\sigma_{\text{elastic}} = 1.5$ barn [72]. The number of collisions in the thermalization can be calculated as

$$N_{\text{collision}} = \frac{ln(E_i/E_f)}{\epsilon}$$

where we can assume the initial energy to be $E_i \approx 1$GeV, the final energy E_f to be the threshold given above and $\epsilon = 0.16$ for carbon is the average logarithmic energy loss per collision. The average number of scatterings results to be $N_{\text{collision}} \simeq 30$ and using $N_{\text{neutron}} = 3000\text{day}^{-1}$ from the previous sections we can then calculate the number of nuclei produced in a day for the different isotopes. The total numbers of background events are then obtained using the Monte Carlo simulation with proper β spectra, and listed in the fifth column of Table 7. While most channels give no background above 1 MeV because the decays proceed through electron capture or they have very small Q value, non-negligible backgrounds arise from ^{12}B, ^{10}C and ^{11}C with a lifetime of 20 ms, 19 s and 20 min respectively. The first one can be effectively vetoed with a very small deadtime. On the other hand this simple (and probably much too conservative) estimate puts the last two processes in a critical region for the possible study of solar neutrinos. Our detector will be able to experimentally study this background during the first phase of data-taking.

- *Activation by muon capture:*

Isotope	Weight (t)	Capture rate (10^4 s^{-1}) [73]	Capture Br. (%)	Total Capture (day$^-$1)	Background (day$^-$1)
H	159.75	-	0	0	
^{12}C	833.05	3.76 ± 0.04	8	9	1
^{13}C	9.35	3.38 ± 0.04	8	0.09	0

Table 8: Estimated background from activation by muon capture.

The muon capture reaction

$$\mu + (A, Z) \longrightarrow \nu_\mu + (A, Z-1)^*$$

produce an excited nucleus $(A, Z-1)^*$ which then de-excite into radioactive isotopes. As an example, muon capture on ^{12}C will produce an excited ^{12}B, which will then quickly de-excite by the following reactions:

$$^{12}\mathrm{B}^* \longrightarrow \gamma +^{12} \mathrm{B}, \quad (17\%)$$

$$^{12}\mathrm{B}^* \longrightarrow \mathrm{n} +^{11} \mathrm{B}, \quad (78\%)$$

$$^{12}\mathrm{B}^* \longrightarrow 2\mathrm{n} +^{10} \mathrm{B}, \quad (5\%)$$

The ground state of ^{12}B is radioactive and hence a potential source of background. Table 8 summarizes the muon capture rate and the relative backgrounds induced in 1 kton of scintillator. None of the isotopes present in our scintillator produce appreciable rates.

- *Activation by muon spallation:*

  The main reactions from muon spallation are $^{12}\mathrm{C} + \gamma \rightarrow \mathrm{n} +^{11}$ C, $^{12}\mathrm{C} + \gamma \rightarrow 2\mathrm{n} +^{10}$ C, $^{12}\mathrm{C} + \gamma \rightarrow \mathrm{p} +^{11}$ B, $^{12}\mathrm{C} + \gamma \rightarrow \mathrm{np} +^{10}$ B and $^{13}\mathrm{C} + \gamma \rightarrow \mathrm{n} +^{12}$ C where the γ is a virtual quantum in the interaction with the muon. Of all the final states only ^{10}C and ^{11}C give origin to visible decays. Although an exact calculation for the rate of production of this isotope is not easy to obtain, we can easily compute an upper limit by conservatively assuming that all the neutrons created in the detector (3000 day^{-1}) come from the above spallation processes. We can then use the cross sections in[71] to compute the relative fraction of spallations proceeding via the channel we are interested in. We obtain a rate of ^{10}C and ^{11}C production of < 1800 day^{-1}.

For some of the cosmogenic activation channels recent measurements from BOREXINO [67] exist and are compatible with our upper-limit estimates.

3.2 Background from Natural Radioactivity

Backgrounds from radioactive decays in KamLAND derive primarily from three sources:

- decay chains of the long lived ^{238}U, ^{232}Th and ^{40}K naturally present in small amounts in rocks surrounding the detector and material used in the detector construction;
- decay of ^{60}Co artificially added to steel during production for quality monitoring purposes;
- decay of ^{222}Rn continuously produced in the disintegration of ^{238}U contained in rocks and detector materials. Since the radon readily diffuses into many materials and has a lifetime of a few days it effectively acts as a carrier that disperses the radioactivity through the entire detector unless special precautions are taken.

In order to study these backgrounds, we have modeled the complete decay chains of these isotopes, derived from [75], in our Monte Carlo program as shown in Tables 14-17 of the Appendix. ^{222}Rn is part of the ^{238}U chain and it is not listed separately.

For simplicity we explicitly considered only those decays with branching ratios greater than 0.5%, while the remaining modes have been lumped together in a fictitious mode marked with *. This mode has been assigned conservatively equal energy sharing among β-decay and a single γ line, resulting in a relatively large energy γs in the detector. Finally in β-decays only the three-body kinematics is simulated, disregarding modifications of the energy spectra and angular correlations due to matrix elements and coulomb corrections. Particles are then tracked by GEANT and when energy is deposited in the scintillator resolution functions for the energy and position are applied. In addition α absorption is "quenched" by multiplying the light emitted by a quenching factor $q = 0.1$. Energy depositions in a time window of $1\mu s$ are added together. The resulting energy spectra for the case of isotopes distributed in the scintillator are shown in Figure 17. ^{60}Co is not shown since it is not expected to be present in the bulk scintillator and has a trivial spectrum, while we explicitly show the ^{222}Rn spectrum since, as previously noted, Rn will have a distribution largely independent from the U sources.

Finally, to transform these distributions in a background estimate we need to assign the appropriate isotope concentrations to the different materials in the detector. In Table 9 we summarize the decay properties of the isotopes considered. Nuclear Data for the five main isotopes used in the simulation are given in Tables 14-17 in Appendix. In counting the number of decays or the number of daughters, those with $T_{1/2} < 500$ s are combined with their mother as cascade, therefore not counted. Those decays with total energy less than 100 keV are excluded.

It is clear that, while the very large volume of our detector gives us a tremendous shielding factor towards external radioactivity, radon can still travel inside KamLAND

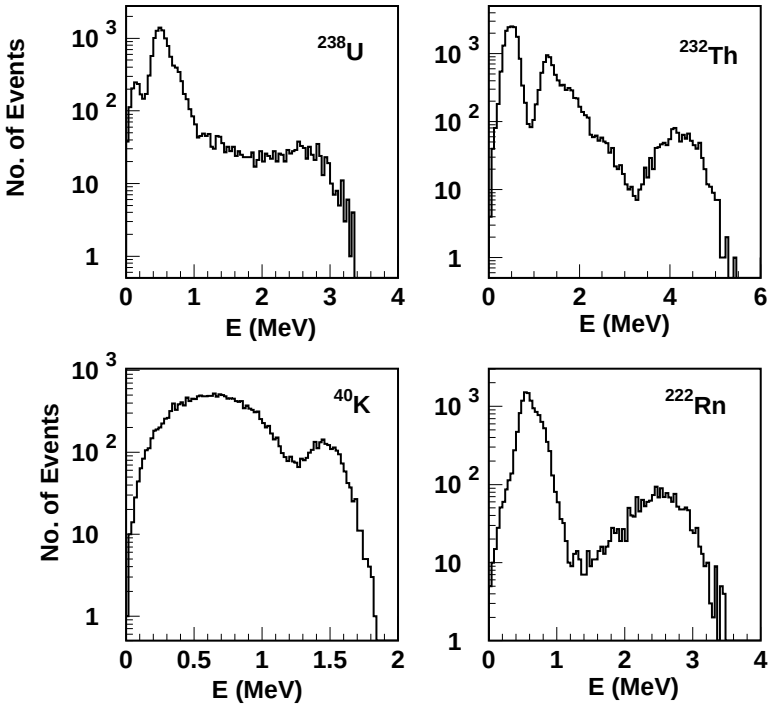

Figure 17: Energy spectra resulting from our Monte Carlo simulation of the decay chains from different isotopes distributed in the scintillator.

Isotope	$T_{1/2}$ (yr)	Natural Abundance	Activity (Bq/g)	No. of Decays (1/Bq)
^{238}U	4.47×10^9	0.993	12344	10
^{232}Th	1.41×10^{10}	1.000	4044	6
^{40}K	1.28×10^9	1.17×10^{-4}	2.5×10^5	1
^{222}Rn	3.8 day	0	5.7×10^{15}	5
^{60}Co	5.3	0	4.2×10^{13}	1

Table 9: Summary of decay parameters for the five main isotopes considered in the simulation. Only decays with $T_{1/2} > 500$ s are individually counted, while decays with shorter $T_{1/2}$ are combined with their mother as cascade. As already mentioned decays with total energy less than 100 keV are excluded. The specific activity in column 4 refers to the radioactive isotope listed only.

carried by the liquids in which it easily dissolves. Therefore the detector will be equipped with a number of barriers designed, among other things, to confine the radon outside the fiducial volume. Radon emanation rates in the same type of glass used for the KamLAND photomultipliers has been measured to be 10 mBq/PMT by the SuperKamiokande collaboration [76]. The radon specific activity in the buffer volume can then be estimated to be 10 mBq/m^3. To the purpose of background simulation we take here a conservative approach and assume that only one radon barrier film is present (balloon). Furthermore we assume the barrier to be nylon with a permeability coefficient for radon of 10 cm^3 mm m^{-2} day^{-1} atm. This reduces the specific activity into the active volume to 1 μBq/PMT. The use of two barriers should further reduce this figure.

The result of the simulation of several millions of events is shown in Table 10 together with the expected contaminations of the different parts of the detector. Contaminations in the steel tank are derived from sampling of steels used for the construction of the Palo Verde detector, while in the case of the rock surrounding the detector we use measured activities of the worst rocks sampled from the KamLAND cavity. The contamination figures for the glass are obtained by direct measurements on prototype Hamamatsu tubes.

For the scintillator we use a contamination of 10^{-14} g/g that is known to be readily achievable through continuous purification [80]. As we will see, better purities (at or below 10^{-16}g/g) will probably be required for the second phase of the experiment, and under this new assumption the table can be easily re-scaled.

The backgrounds listed in Table 10 are singles above 1 MeV; "1 kton back." is calculated in the entire scintillator volume (6.5 m radius) while "600 ton back." uses a smaller fiducial volume (5.5 m radius) that could be implemented with a software cut on the event position.

It is clear that the background for the detection of singles is dominated by the internal radioactivity of the scintillator. Substantial work on this issue will be carried

Material	Mass (tons)	Isotope	Purity (ppb)	1 kton back. (Hz)	600 ton back. (Hz)
Scint.	920	^{238}U	10^{-5}	0.287	0.191
		^{232}Th	10^{-5}	0.106	0.075
		^{40}K	10^{-5}	0.453	0.334
		radon	1 μBq/m^3	0.002	0.001
Buffer Oil	1523	^{238}U	10^{-5}	0.003	0.0
		^{232}Th	10^{-5}	0.001	0.0
		^{40}K	10^{-5}	0.009	0.0
		radon	10 mBq/m^3	0.030	0.0
Steel Tank	31	^{238}U	1	0.001	0.0
		^{232}Th	1	0.004	0.0
		^{40}K	1	0.010	0.0
		^{60}Co	10^{-9}	0.005	0.0
PMT	7.2	^{238}U	400	0.503	0.003
		^{232}Th	300	0.137	0.0004
		^{40}K	180	0.046	0.0002
Rock	627	^{238}U	73000	0.199	0.001
		^{232}Th	200000	0.059	0.0002
		^{40}K	4600	0	0
Total				1.855	0.606

Table 10: Single rates above 1 MeV for all materials and radon. The forst column of backgrounds refers to the entire detector (1 kton) while the second refers to a smaller fiducial volume.

out during the first phase of the experiment to better understand and reduce such background. On the other hand we can easily see that using only proven technology the background rate for correlated events is quite modest and sufficiently low to give us a good margin for the first phase of operation. This is illustrated by Table 11 where we summarize the backgrounds for correlated events as defined above, together with the backgrounds for singles. The natural radioactivity correlated backgrounds derive from the U and Th decay chains. Their rate is calculated using a quenching factor of 10 for the scintillation from αs but conservatively we use no Pulse-Shape Discrimination.

Backgrounds for singles	1 kton back.	600 ton back.
Prompt neutrons from muon spallation	4.0 day^{-1}	3.0 day^{-1}
Activation from neutron capture	0 day^{-1}	0 day^{-1}
Activation from neutron spallation	< 1800 day^{-1}	< 1200 day^{-1}
Activation from muon capture	0 day^{-1}	0 day^{-1}
Activation from muon spallation	< 1800 day^{-1}	< 1200 day^{-1}
Natural radioactivity	1.855 Hz	0.606 Hz
Backgrounds for doubles		
Cosmic muons induces neutrons	0.1 day^{-1}	0.07 day^{-1}
Natural radioactivity (random coincidence)	0.15 day^{-1}	0.02 day^{-1}
Natural radioactivity (correlated)	0.005 day^{-1}	0.003 day^{-1}

Table 11: Summary of background rates for singles and doubles.

4 The Site

The KamLAND detector will sit in the cavity built for the Kamiokande detector under the summit of Mt. Ikenoyama in the Japanese Alps, about 50 km east of the town of Toyama. The rock overburden is more than 1,000 m in any direction with an average rock density of 2.7 g/cm^3. The minimum (surface) energy required for a muon to reach the detector is about 1.3 TeV and, with an attenuation factor of 10^5 with respect to the surface flux the cosmic-ray muon rate is 0.3 $m^{-2}s^{-1}$.

This site is at 500 m distance from SuperKamiokande presently taking data under the same mountain. The detector location inside the mountain with its position relative to SuperKamiokande is shown in Figure 18.

Since the mine under Mt. Ikenoyama has been extensively used for cosmic ray research, much of the infrastructure for KamLAND is already in place. In addition a number of companies, including the local mining company, are familiar with the type of activities required, so that their expertise can be directly used in this project with substantial saving in money and logistics. The cavity for the experiment has been drained from the water and the old Kamiokande detector dismantling started in March 1998.

Figure 18 also shows the tunnel connections with the outside. Access to the old Kamiokande is at present possible through a small railroad tunnel from the Mozumi entrance or through a newer, large road tunnel going to SuperKamiokande from the Atotsu entrance of the mine. This last road, accessible to large body dump trucks, is being extended to the KamLAND site by enlarging one of the small size tunnels already available between the two laboratories.

As shown in Figure 19 at least four larger cavities will be provided along the access tunnels to install counting facilities, scintillator and water purification and processing

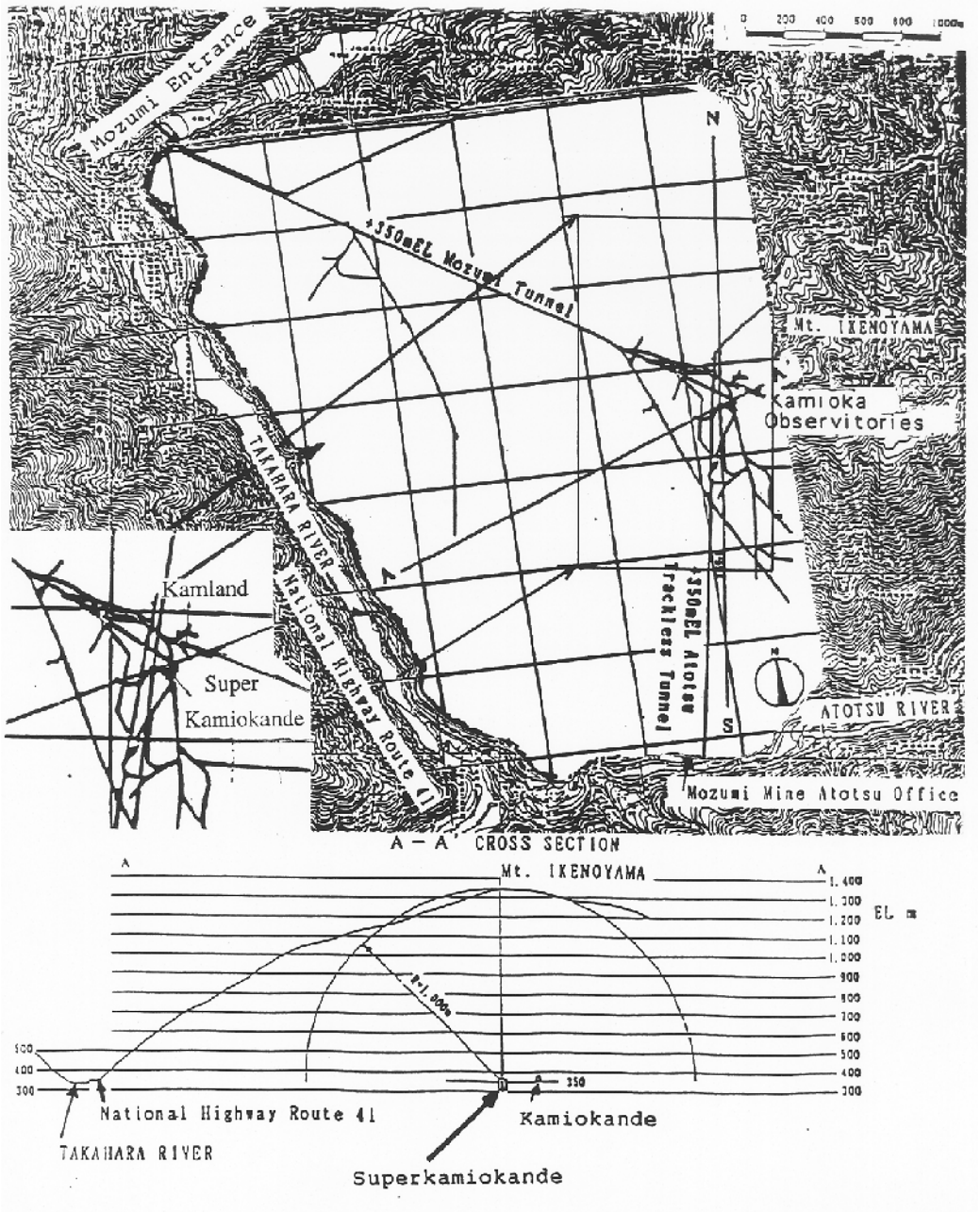

Figure 18: Partial view of the system of tunnels inside Mount Ikenoyama with the locations of KamLAND and SuperKamiokande. The Atotsu tunnel is a large road tunnel accessible to regular size trucks. A profile of the mountain along the direction of smallest extent is also shown.

equipment and the electrical sub-station. Special fire doors will completely seal the experiment from the rest of the mine during the scintillator processing. Initially a mechanical ventilation system will assist natural ventilation (used for Kamiokande and SuperKamiokande) in order to guarantee safe conditions for scintillator handling. A special ventilation system using air intake from a tunnel reaching high elevation on Mount Ikenoyama will be installed at a later time. As a first radon barrier the rock in and around the detector area will be painted with a special impermeable polyurethane coating already used for the SuperKamiokande experiment. Several more radon barriers are discussed in different sections of this Proposal.

A new 3 kV line will be brought to the KamLAND electrical sub-station. Both 110 V and 220 V will then be distributed through the different detector areas.

5 Detector Design

5.1 Overview

A cutout view of the KamLAND detector is shown in Figure 19. The fiducial volume consists of a sphere containing 1000 tons of liquid scintillator. The scintillator container, having a 6350 mm radius, is a thin plastic-walled balloon (referred to as "the balloon" in the following) and is not supposed to take the weight of the scintillator but only to isolate it from an outer layer of non-scintillating fluid. Such fluid and the liquid scintillator are contained and mechanically supported by a stainless steel spherical vessel that also provides the mechanical structure where the photomultipliers for the fiducial volume are mounted.

The sphere is solidly mounted inside the cylindrical rock cavity and the space between them is filled with water and used as a veto Čerenkov counter. Several options are under study for the scintillator and the overall goal would be to be able to detect scintillation and Čerenkov light and perform neutron (proton) γ (electron) separation using pulse shape analysis. Events will be localized inside the fiducial volume using the differences in time of flight to the different photomultipliers so that large area, fast tubes are required. The veto counter will be divided in three regions and readout using Kamiokande photomultipliers.

5.2 Mechanical Structure

The major mechanical component of the experiment is a stainless steel sphere ("the sphere") that will contain the liquid scintillator, buffer liquid and inner detector photomultipliers. The sphere has a diameter of 18 m and, with no water outside, will have to support a load of 2,500 tons. In order to achieve its structural purpose the sphere will be built out of stainless steel of thickness ranging from 6 mm (top) to 17 mm (bottom). A set of 16 columns will support the sphere at its equator via a special ring reinforcement. The detailed design and construction is being handled by The Mitsui Ship-building Company that has handled the steel construction for SuperKamiokande. It is important to realize that the sphere, besides representing the safety containment vessel for the flammable liquids, is also an essential component for the reduction of radon in the detector. Such a thick metal shell, together with appropriate seals for its only opening at the top, guarantees that no radon from the rocks and other external materials can enter the detector volume, reducing the problem of radon suppression to the relatively clean materials inside the sphere.

A cylindrical stainless steel chimney of 3 m diameter will protrude from the top of the sphere to permit access to the central detector during installation. Buffer oil and scintillator lines as well as calibration ports will be mounted in the chimney along with all the electrical cabling as illustrated in Figure 20.

A smaller diameter acrylic chimney ("stem") will be mounted inside the large chimney and will serve to position and bring services to the liquid scintillator balloon.

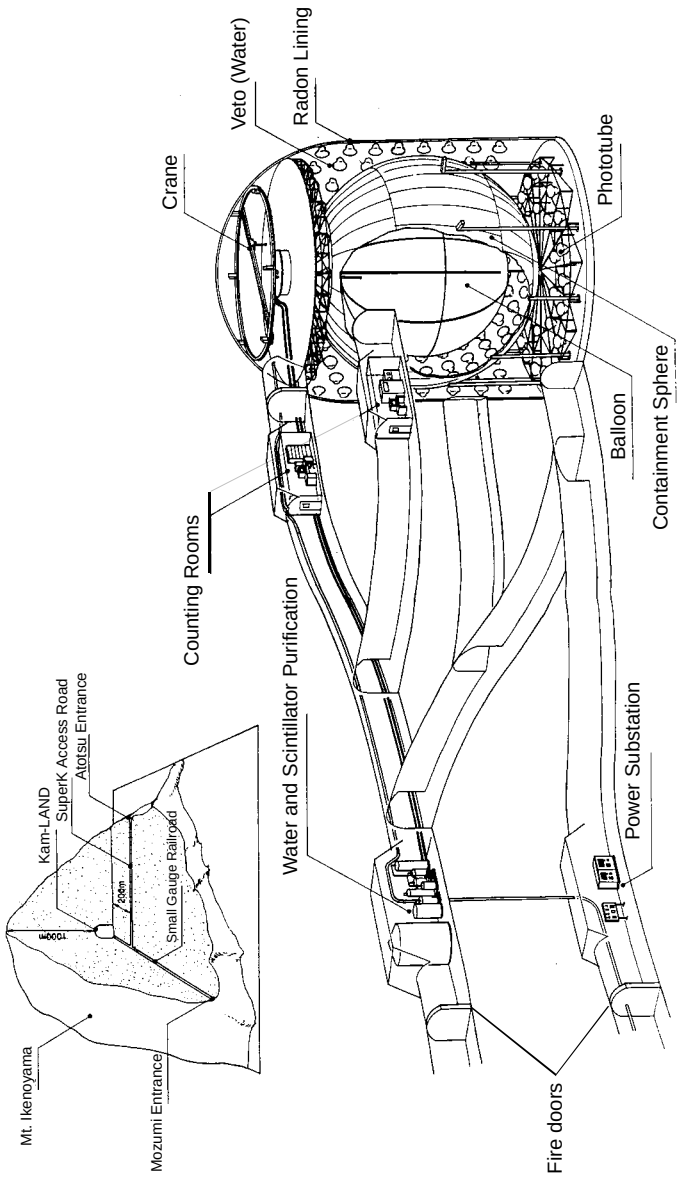

Figure 19: General view of the underground layout in the KamLAND detector region. Several enlarged tunnel sections will house the electronics, scintillator and water purification systems, ventilation system and electrical sub-station. Fireproof bulkheads will isolate the KamLAND area from the rest of the mine during scintillator handling.

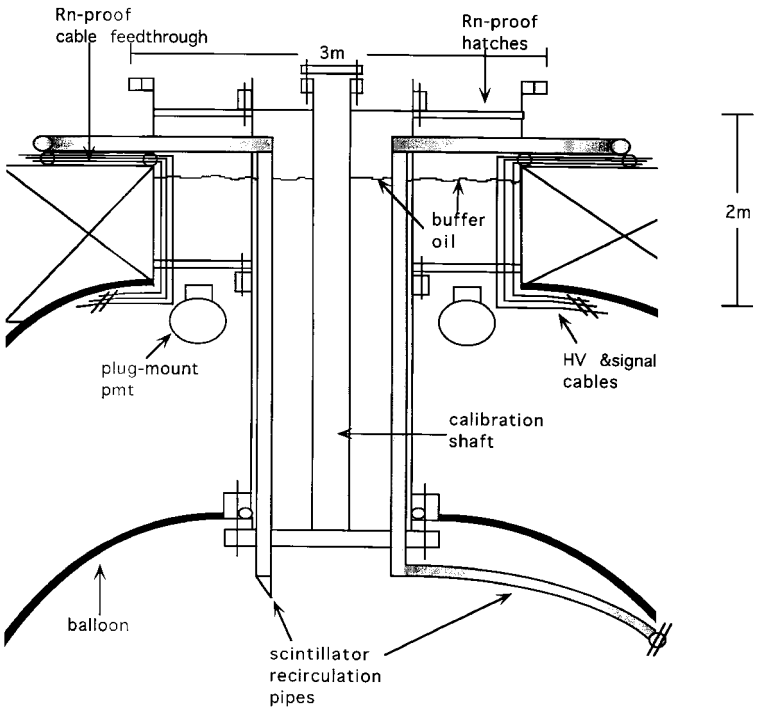

Figure 20: Schematic drawing of the detector chimney.

The balloon itself will be restrained by a set of cables connected to different positions on the inside surface of the sphere.

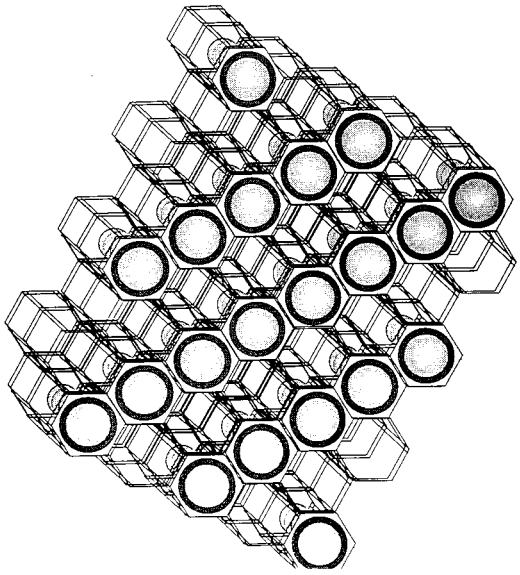

Figure 21: Mechanical structure holding photomultipliers in place inside the sphere.

Photomultipliers for the central detector will be mounted inside the sphere with an hexagonal lattice structure as shown in Figure 21. All surfaces except the photocathodes will be light absorbing so that only direct photons will be recorded. The support structure will be able to accommodate 1,922 20-inch photomultipliers, although we may chose to equip only half that many (as shown in the Figure).

The veto detector will register traversing cosmic-ray muons via the Čerenkov light deposited in the water layer surrounding the sphere. The total volume of 4,500 m^3 of pure water will be divided in three main sections and contained by the rock painted with water-resistant urethane coating impermeable to radon.

Veto photomultipliers (a total of 338 20-inch tubes from Kamiokande) will be supported by two disks made of aluminum truss framework for the top and bottom (Figure 22) and vertical aluminum hangers for the cylindrical side region (Figure 23). Each disk contains 89 tubes and is 1 m thick. While the bottom disk has to withstand the photomultipliers' buoyancy ($\sim$ 50 kg/pmt) the top disk also supports a sealed aluminum floor. The side hangers are arranged to support 20 vertical arrays of about 8 tubes each, for a total of about 160 tubes.

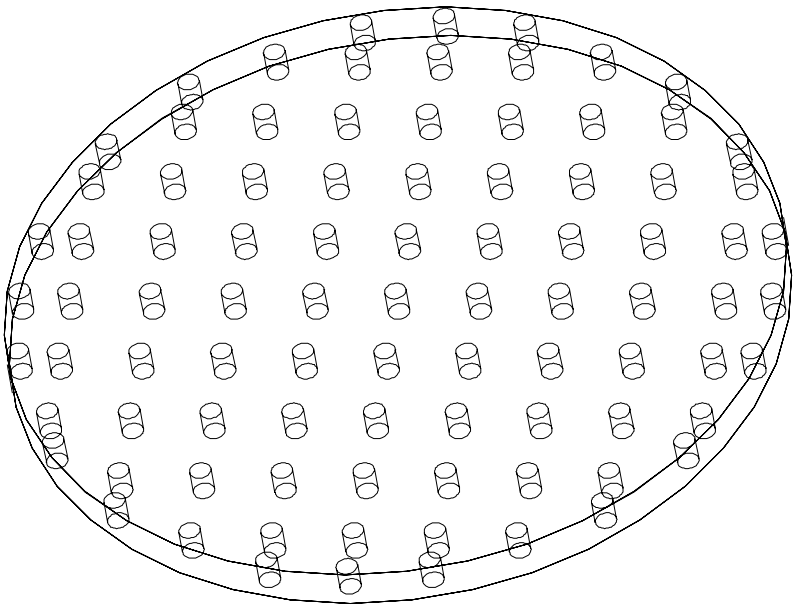

Figure 22: Arrangement of photomultipliers in the top and bottom veto detectors.

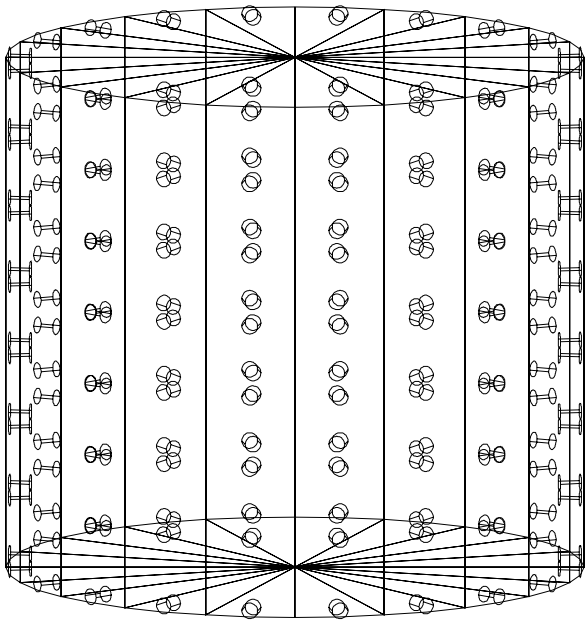

Figure 23: Arrangement of photomultipliers in the cylindrical side veto detector.

5.3 The Scintillator Balloon

The central balloon represents an extremely critical part of the detector. Its primary purpose will be to isolate the scintillator from the external oil. There are a number of reasons to have such a division. We want the scintillator to be shielded from the multitude of materials forming the sphere, photomultipliers, cables, and their mechanical and electrical support. These materials, although selected to be low in radioactive background, will be substantially "dirtier" than the scintillator itself. We also want to be in the position of choosing the scintillating fluid on the basis of its performance and safety, without having to worry about the chemical compatibility with the many aforementioned components. Finally and most importantly, the balloon, properly engineered, will represent the last radon barrier protecting the fiducial volume. We note here that it is correct to assume no shielding effect to radon migration from the different liquids. This is because radon transport is completely dominated by mixing (natural convection and artificial recirculation) that is much more efficient than simple diffusion.

The balloon will have to be radiologically pure, transparent for light in the 300 to 500 nm window, chemically inert and as impermeable as possible to radon. Since the exact formulation of scintillator is still under study we are designing the balloon to be able to withstand up to 20 tons of buoyancy force due to different densities between the buffer oil and the scintillator.

While it is hard to find all the above properties in a particular polymer film, great expertise on the engineering of multi-layer plastic films exists within the food packaging and scientific stratospheric balloon industries. At the present stage we are exploring a number of multiple layer sandwiches including films of polyamide (nylon), polyethylene, fluoropolymers, EVOH and PVDC. The last two are special polymers designed to be impervious to gases. Since precise measurements of radon permeability are not generally available, a special apparatus has been setup to perform these measurements. This apparatus is schematically shown in Figure 24.

Structural analysis for the balloon is being discussed with some of the firms building stratospheric balloons for the NASA Scientific Balloon Facility in Texas and with the Mitsui Company in Japan. We plan to restrain the balloon in its position by a web of plastic cables secured to the inside of the sphere. Obviously the filling of liquids inside and outside the balloon will have to be carefully carried out in parallel in order to avoid stresses to the membrane.

Since, as discussed in the background section, the main source of radon in our detector is expected to be in the uranium impurities in the (low activity) glass of the photomultipliers, we are also planning to individually bag or coat the phototubes with a transparent polymer impermeable to radon. This is a very important concept in the detector design as it relaxes the requirements for this barrier in terms of chemical compatibility and mechanical strength. However, since these developments are still at an early stage, we conservatively use for the backgrounds in this Proposal only one barrier (the balloon) made of 100μm thick nylon.

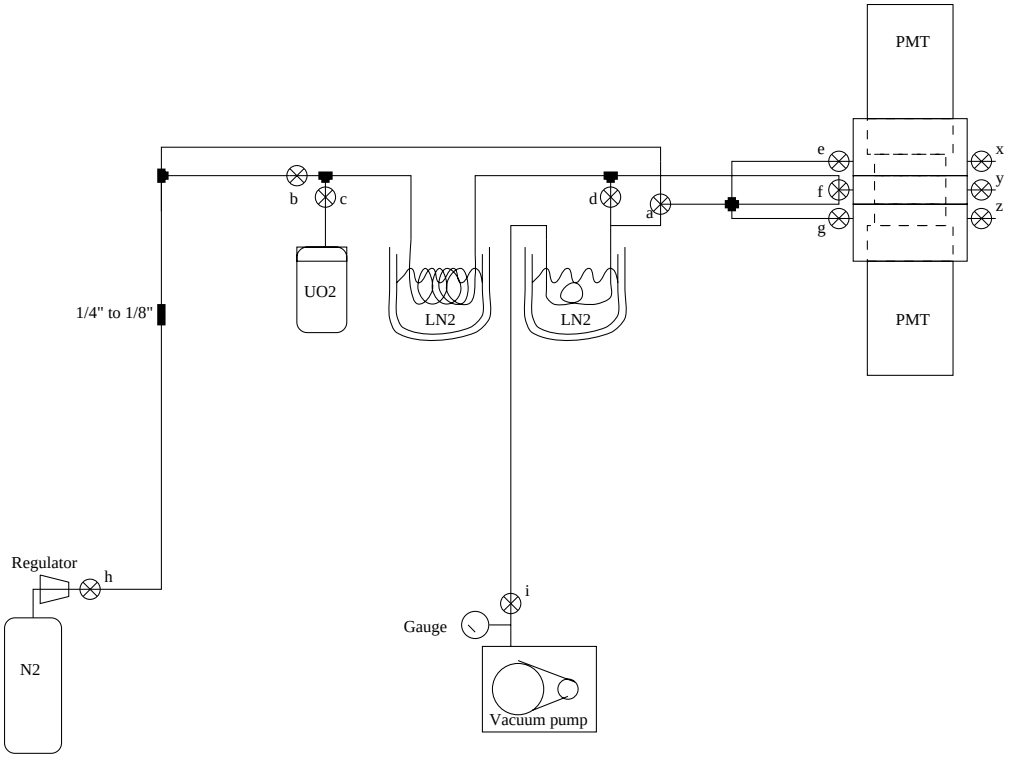

Figure 24: Schematic view of the radon permeability apparatus.

5.4 Liquid Scintillator and Buffer Fluid

The liquid scintillator confined by the balloon in the center of the detector is arguably the single most critical component of KamLAND. From the beginning of the experiment the scintillator will need to detect and reconstruct anti-neutrino events depositing energies as low as 1 MeV in a mass of 1 kton. This implies good light output and optical clarity. In addition we are planning to use pulse-shape discrimination (PSD) to statistically separate energy depositions due to direct ionization from the ones due to proton recoil. The regulations on the use of hazardous materials in the Kamioka mine and price and availability considerations further restrict the range of possible choices.

Other features, like the extremely high purity needed to count singles from solar neutrinos or the ability to observe Čerenkov rings in the "background" of scintillation light, will become important for future phases of the experiment.

As a consequence of this staged approach we are now formulating a relatively conventional scintillator for the first phase of the experiment, while laboratory R&D and the study of the behavior of the conventional scintillator in the full detector will indicate to us what improvements are needed in order to achieve the sensitivity required for the second phase. We believe that this approach is extremely desirable when dealing with ultra-low backgrounds and a liquid that is by definition easy to move for the purpose of purification, modification or even replacement.

In the following we will discuss separately our baseline formulation for the first phase, the purification system being designed for such scintillator and the R&D program planned for the second phase.

The choice of the buffer fluid closely follows the choice of the scintillator in order to match as closely as possible the specific gravity (and hence stresses on the balloon), index of refraction and radio-purity. Given the large quantity needed, cost is also an important consideration. Buffer fluids will be discussed together with scintillators in the following section.

5.4.1 Phase 1 Scintillator

The formulation of organic liquid scintillators[77] is based on a general scheme involving the ionization of a bulk solvent and the successive non-radiative energy transfer from the solvent molecules to fluorescent molecules (fluor) dispersed into the solvent at relatively small concentrations. The fluorescent molecules de-excite with emission of photons that are typically in the near-UV to green region of the spectrum. This two-step chain is essential since it allows one to use low concentrations of fluor resulting in small self-absorption and reasonable cost (the solvent being, in general, dramatically cheaper than the fluor). It is important to find solvents with long radiative lifetimes (so that direct de-excitation is not likely) and good ability to delocalize the excitation over large distance, so that a low-concentration fluor has still very high probability of being excited. It is well known that aromatic solvents are very efficient

in this respect and many liquid scintillators have been based on such materials.

For large size detectors like KamLAND the light attenuation length in the bulk liquid becomes a very serious issue and this parameter becomes essential in the optimization of the fluid. Since all practical solvents and fluors have absorption bands in the short wavelength region of the spectrum an obvious solution is to shift the wavelength towards longer wavelength. This is usually done within the tight limits of existing photocathodes. In practice only a narrow window is available between the absorption in the near-UV and the photocathode cutoff in the green. In addition purity, cost and chemical hazard considerations are extremely important in large underground detectors like KamLAND.

In the detection of anti-neutrino Gadolinium doped scintillators present the obvious advantages of faster neutron capture and large energy release. Indeed substantial expertise in this field is present in this group thanks to the experience with the Chooz and Palo Verde detectors. However the lower intrinsic background of a very large and deep detector substantially weakens the motivation for such exotic scintillators and considerations of cost, long term stability and difficulty of achieving very low radioactive contaminations make this option unpractical for a detector like KamLAND, at least for the first phase of data-taking.

For the initial phase of KamLAND we have conservatively chosen to use a scintillator of simple and well proven formulation. This scintillator will use Pseudocumene (1,2,4-Trimethylbenzene) as primary solvent with PPO (2,5-Diphenyloxazole) as primary fluor. In Figure 25 we show the light yield in arbitrary units as function of different concentrations of PPO in different aromatic solvents. At least for concentrations above 2g/l there is a very small difference of light yield between the various solvents. The flash-point is lowest for Toluene (4°C) than in Pseudocumene (48°C). The last solvent, DIN (Di-isopropylnaphtalene) is essentially non-flammable (flash point is 148°C) and it presents essentially no health hazard. The alternative use of this solvent is under study and will be briefly discussed later.

The low flash point forces us to study the possibility of diluting the primary solvent in a co-solvent like Isoparaffine. We have chosen to use Isoparaffine (IP), which has the same effect as mineral oil, except it is lighter (n$\sim$10-15), and has lower radioactivity due to the extra cracking and distillation during its production. Like mineral oil it has low vapor pressure, high flash point (90°C), and low toxicity. In Figure 26 we show how the light yield decreases for increasing dilution of the primary solvent in the Isoparaffine.

Choosing a 20% concentration of Pseudocumene in the oil retains most of the scintillator properties while substantially reducing flammability, toxicity and cost. The flash point of such cocktail is increased to (62.5°C), above the (60°C) limit mandated by the mine operations.

While some details of the formulation like the exact concentration of PPO and the possibility of adding a secondary shifter (bis-MSD) to better match the wavelength of the scintillation to the transparency of the liquid are still under study, the

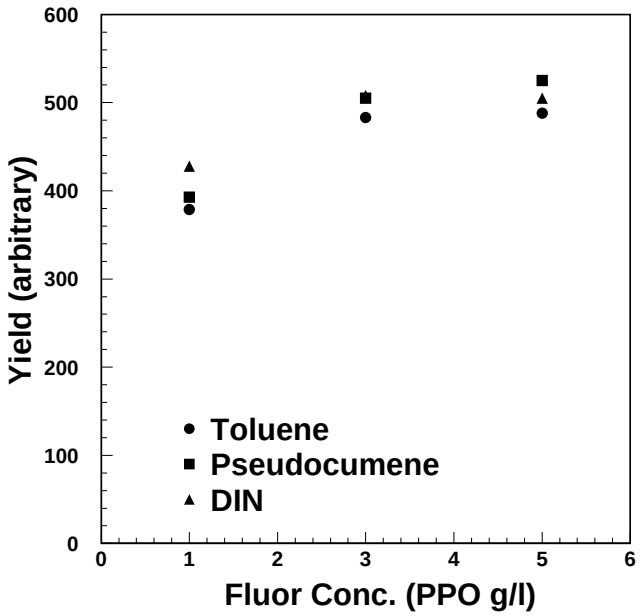

Figure 25: Light yield for different concentrations of PPO in Pseudocumene (squares). Also shown are the yields for the same fluor in Toluene and DIN.

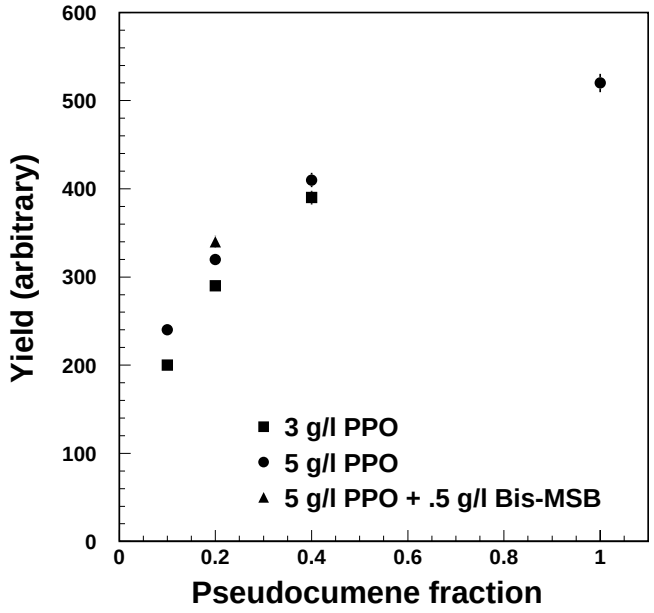

Figure 26: Light yield for different concentrations of primary solvent (Pseudocumene) in a co-solvent (Isoparaffine). Data for different fluor concentrations is shown. We also show (triangle), for one case, the effect of adding a secondary wavelength shifter bis-MSB to the cocktail.

cocktail described above has been demonstrated to achieve properties that are totally adequate to the physics to be performed in the first phase of Kamland. In particular it has a light yield of 50% of anthracene and attenuation length better than 12 m (at $\lambda = 440$ nm), resulting in an energy resolution $\sigma(E)/E = 10\%/\sqrt{E}$ (assuming 25% photocathode coverage, 20% photocathode quantum efficiency and 80% transmission from balloon and glass). For γs we have also measured a pulse FWHM of 9 ns that we expect, from simulation studies, to result in a position resolution $\sigma = 10$ cm at 1 MeV.

From laboratory tests we expect a quenching factor of about 10 for for scintillation produced by α particles (relative to γs). This factor is used in our Monte Carlo studies and it is very important in the suppression of backgrounds from radioactive decays. We have also measured good pulse-shape discrimination (PSD) between scintillation produced by neutron-induced recoils and γs. This is shown in Figure 27 where we show the measured ratio between the total charge in a pulse and the charge after 25 ns for γ events and neutron recoils. The three plots represent different Pseudocumene concentrations. It is clear that the 20% Pseudocumene concentration chosen for the KamLAND formulation still gives a substantial PSD. Since our detector is built in such a way that only direct photons from scintillation are detected (light is absorbed at the first scattering) PSD will also be functional in the full size bulk scintillator. However, while still investigating how to best use this property for background suppression, we have conservatively not used it in the simulations performed for this Proposal. PSD will be further studied at the Tohoku University Test Bench Facility briefly described below and it will be routinely measured in KamLAND by the standard detector calibration runs.

Since the hydrogen/carbon ratio is $\simeq 2$ for Isoparaffine (C_nH_{2n+2}) and 1.33 for Pseudocumene (C_9H_{12}) the cocktail described above will have a ratio of $\simeq 1.87$.

We are planning to use pure Isoparaffine as a buffer fluid for this scintillator. In this way the difference between densities inside and outside the balloon can be of about 2%, corresponding to a 20 ton downward force on the balloon. We are investigating the use of n Isoparaffine with slightly longer chains that should allow us to match better the two densities and minimize the stress on the balloon.

5.4.2 Scintillator Purification System

During the experiment lifetime both scintillator and buffer fluid will be continuously purified to reduce the background from internal radioactivity. While typical levels of U, Th and ^{40}K contamination in good quality Isoparaffine are 10^{-13} g/g, we are planning to reduce them to at least 10^{-14} g/g for the first phase of the experiment. The purification system will need to remove these "original" contaminations as well as the radioactive nuclei produced initially and during the lifetime of the experiment by cosmogenic activation (mainly ^{7}Be) and radon decay (^{210}Pb). As discussed in the section on backgrounds the requirements on purity for all these isotopes are within

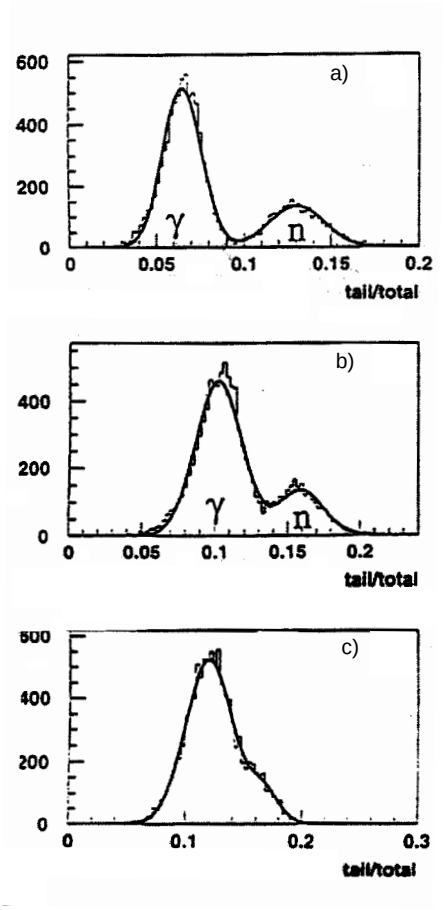

Figure 27: Pulse-shape discrimination in KamLAND scintillator. We use the ratio between the total charge and the tail charge (25 ns to ∞) as a variable to statistically discriminate between γ-like events and n-recoils. This variable is shown for 50%, 20% and 10% Pseudocumene concentration in the scintillator (respectively parts a), b) and c)). Neutron contamination for a cut preserving 90% of the γs is respectively 1.5%, 6.5% and 20%.

the present technology for the first phase of the experiment, while in the case of a later running with a low-energy single trigger, substantially more aggressive background reductions will be needed. We are confident that the experience gained with the first operation of the whole detector together with the R&D in progress in our labs and similar efforts done for BOREXINO will provide us with appropriate solutions.

Purification methods[78] have been developed by the BOREXINO group that needs, from the very beginning, contaminations of order 10^{-16} g/g. These methods are highly effective at removing U, Th, Pb, K and Be and purity levels below 10^{-15} have been reached for U, Th, at their test facility. The process, that serves to extract Pb and Be as well, is based on the higher affinity of metals for highly polar solvents like water. Water is first mixed with scintillator and then separated into two fluids by gravity. Metal ions prefer the (polar) water environment and are effectively removed from the scintillator. Nitrogen purging then removes the dissolved water as well as the radon (although the recirculation time in the purification process is too slow to serve as an effective Rn abatement tool). Since the efficiency for removing Be is several orders of magnitude lower than for U, Th, K, and Pb, vacuum distillation is then used to remove Be much more effectively and to improve the attenuation length by removing chemical compounds. In addition 0.05μ filtration is used to remove dust and other macroscopic contamination.

Although these techniques (developed for a pure Pseudocumene scintillator) cannot be directly employed on the KamLAND two-solvent scintillator, we are presently developing a similar purification system employing for the moment only the water extraction and ultra-filtration steps. A prototype of this system has been built to work with the scintillator Test Bench Facility at Tohoku, processing 20 l/hr of scintillator. With such detector we will be able to test the effects of purification down to 10^{-13} g/g of U and Th by detecting sequential decays in the decay chain. To achieve the greater sensitivity needed for our studies we are developing condensation and neutron activation analysis techniques as explained in a later section. In Figure 28 we show the 1 m^3 test bench now in operation at Tohoku University.

Finally a large water purification system will be built at KamLAND to treat the water of the veto counter and to provide ultra-clean water for the scintillator plant. The system will use water from the same springs under Mt. Ikenoyama that are already feeding SuperKamiokande and process it via ultra-filtering and ionic exchange in CR55 chelate resin. Great expertise on this topic is available in the group from the past experience at Kamiokande and SuperKamiokande.

5.4.3 Scintillator R&D for Phase 2

While the first phase of KamLAND will require only a scintillator that is well within the reach of today's technology, a possible use of the detector for measurements requiring single triggers and thresholds around or below 1 MeV poses formidable problems of background reduction. Although we plan to take full advantage from the

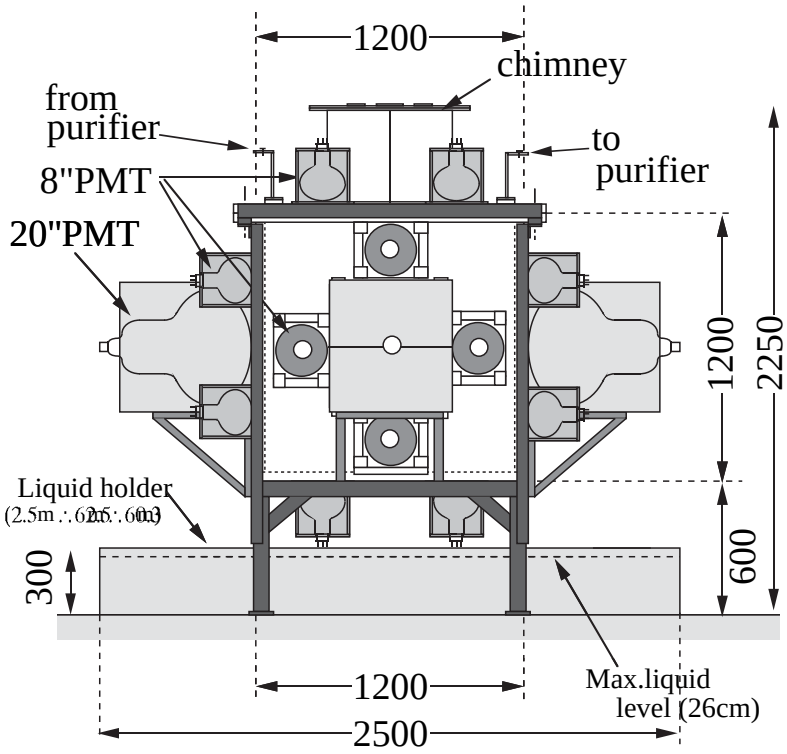

Figure 28: View of the test bench in operation at Tohoku University.

opportunity we have to study backgrounds in a full-size detector during phase 1, a successful R&D program in this field will also require considerable time and has to be started immediately.

As it is clear from previous sections the background for low energy singles will be dominated by internal radioactivity in the scintillator and by ^{222}Rn mainly produced outside the fiducial volume, drifting through the different liquids and plastic sheets.

We have selected three main directions for R&D on scintillator that address the problems of background in rather different and independent ways:

- Improve the purity of a conventional scintillator (probably very similar or identical to the one used in phase 1) at or below 10^{-16} g/g in U, Th and ^{40}K. Similarly improve the contamination from radon and cosmogenic nuclei keeping in mind the results obtained from the first phase of running. This activity is a natural continuation of the scintillator development efforts already under way both in Japan and in the US. It will also require the upgrade of trace element analysis equipments in part already available in some of our laboratories.

- Develop a novel scintillator based on different fluors and, especially, solvents in order to improve the intrinsic performance in terms of PSD, quenching factor and other particle identification techniques. This new scintillator might improve the experiment given its intrinsic ability to identify backgrounds.

  In this field we are now investigating heavier solvents like DIN and PXE that are available commercially (mainly as transformer oils) in large quantities. This solvents are substantially less flammable and hazardous, yet with light yields similar or higher than Pseudocumene. Since they can be used in pure form they can produce scintillators with substantially better PSD and higher yield. In addition, since their density is the same as water to within 1%, these scintillators can be used with water as a buffer fluid, with considerable saving and simplification. Although we are aware of the problems that some membranes like nylon present when soaked with water[81] at least one of our candidate barrier (fluorocarbon) does not have such problems.

- Develop a new scintillator that by its nuclear properties is able to produce physics phenomena that would not be observable otherwise. A relatively simple possibility would be represented by the idea of dissolving Xe (natural or isotopically enriched to ^{136}Xe) into the scintillator to study neutrinoless double-beta decay with a very large mass of candidate isotope. Xe is known to be soluble at least to few percent concentrations in liquid hydrocarbons. The possibility of dissolving other nuclei with more complex chemistry like Cd, Yb and Gd is also being evaluated with the goal of studying double-beta decay and solar neutrinos. Similar concepts are being explored by the LENS Collaboration [82]. Some of the nuclei of interest could also be used as active elements in non-organic fluors based on rare-earth chelates or CdS (Cadmium Selenite) nanocrystals [83].

Although some of these options may seem rather far-fetched they are nevertheless mentioned here to stress the fact that KamLAND is a very versatile detector concept and the experiment, after the first phase is completed, can be simply and relatively inexpensively reconverted for a broad range of new applications. A very active program on these topics has started in the collaboration. This program greatly benefits from the human and technical resources available at different institutions and private companies in the US and Japan.

5.5 Photomultipliers

The large size of the KamLAND detector and the need for large photocathode coverage clearly call for very large size photomultipliers. 20-inch diameter photomultipliers (R3602) have been manufactured by Hamamatsu in large quantities (over 10,000 units) for the SuperKamiokande detector and we plan to rely on a similar size tube for this experiment. However the SuperKamiokande tubes cannot be directly used in KamLAND since they do not have a good enough time resolution. The very large 20-inch photoelectron collection area and a short tube mechanics are obtained in the R3602 by using a large acceptance venetian-blind multiplier section. This design results in a relatively slow risetime (10 ns) due both to the intrinsic properties of venetian-blind multipliers and to the slower photoelectron collection at the periphery of the photocathode area. In order to improve the speed characteristics of the tube Hamamatsu has designed a new tube (R7250), replacing the old multiplier with a fast linear-focusing one in the glass envelope of a R3602. The photocathode diameter is limited to 17 inch, trading area for collection time. In Figure 29 we show the schematic design of the two tubes.

The tube has been designed and prototyped at Hamamatsu and from measurements of the first prototypes at Tohoku and Tennessee a preliminary set of parameters is being compiled as shown in Table 12. While mass production is about to start we are still evaluating envelopes from different glass manufacturers from China, Germany and Japan. A decision regarding the glass will be taken very soon.

The photomultiplier mechanical support structure can hold a maximum number of 1,922 tubes arranged on an hexagonal lattice. This would correspond to about 32% photocathode coverage. Studies are under way to establish whether a lower coverage, for instance 1280 tubes (22% coverage) is still acceptable from the physics standpoint. Care will be taken in absorbing any photon not hitting the photocathode, to preserve good spatial resolution and timing.

The veto part of the detector will be equipped with 338 20-inch photomultipliers from the old Kamiokande detector.

A set of compensating coils will be installed in the cavern to cancel the Earth's magnetic field ($\simeq$ 350mGauss) to a level well below the 50 mGauss limit necessary for proper operation of the photomultipliers. A similar technique is already in use at SuperKamiokande.

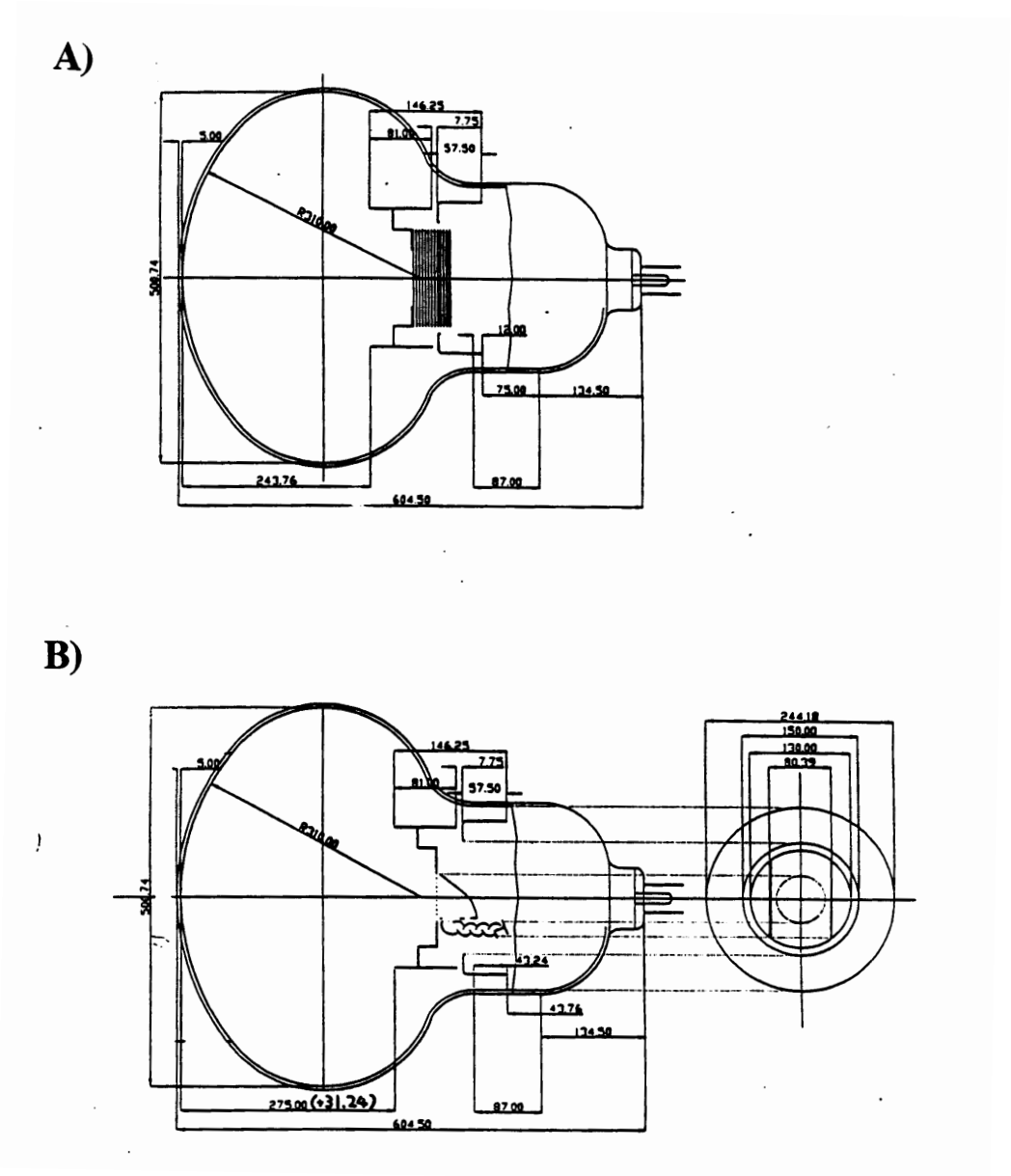

Figure 29: Schematic cross section of SuperKamiokande (A) and KamLAND (B) photomultipliers. The KamLAND tube will use the same glass envelope but will have a smaller photocathode and a substantially faster risetime.

Parameter	Min.	Typ.	Max.
Quantum Efficiency at 480nm	20%	22%	-
HV for 10^7 gain	1500V	-	2500 V
Dark current at 10^7 gain, 25°C	-	-	1μA
Dark rate above 0.25 p.e. at 10^7 gain, 25°C	-	-	80kHz
Time resolution at 10^7 gain, 25°C, full face	-	3.5ns	4ns
Rise time at 10^7 gain	-	7ns	9 ns
Transit Time at 10^7 gain	-	110ns	130 ns
Peak-to-Valley Ratio at 10^7 gain	1.8	2.5	-
Cathode uniformity	-	-	$\pm$10%
Afterpulse fraction (between 150ns and 30μs)	-	-	7%

Table 12: Preliminary characteristics of 20/17 inch Hamamatsu pmts for KamLAND. These characteristics are guaranteed for the first three years of life.

5.6 Electronics

As described above the KamLAND detector will be capable of covering a broad range of science. In order to preserve all its capabilities it is important to design adequate electronics, which allow all the essential details of the interactions to be measured in the entire energy range from a fraction of MeV to a few GeV. This ability will be even more important should new phenomena start to emerge from our measurements.

From the electronics point of view, all physics events in Kamland can be pictured as being composed of a sequence of the "simple" events separated in time. For example, reactor $\overline{\nu}_e$ absorbed in liquid scintillator will produce a simple event of positron followed by a (delayed) simple event of neutron. A simple event corresponds to an energy deposition of a single particle converted to an observable light signal. Single γ, e, μ, or p signals can be considered as simple events. In a multi-PMT detector, the simple event looks like an almost simultaneous set of signals from a large group of photomultipliers. The amplitude and shape of a minimal signal correspond to the single photo-electron (s.p.e.) response of the PMT. The maximum duration of a PMT signal is determined by the track length of the particle (muon, for example) in the scintillator volume, and by the speed of light propagation in the liquid scintillator. For a simple KamLAND event, the maximum difference between the arrival time of the pulses from different PMTs is ~ 80 ns, and maximum duration of the pulse in a PMT channel is ~ 110 ns.

The information contained in a simple event can be obtained by the measurements of the relative arrival time (spatial position), pulse width (track length), and the total charge (energy) of the PMT signals. In addition, the signal shape carries particle identification information from PSD in the scintillator or, possibly, Čerenkov light that is produced with much faster time-constants.

Real physics events will be composed of one or several simple events separated by time intervals ranging from tens of nanoseconds (as in case of $\pi \rightarrow \mu + \nu$ decay) to hundreds of microseconds (as in the neutron capture) and even to seconds or minutes (as with the lifetime of excited nucleus states). To fully use the information in a statistically limited sample of rare events (a situation typical for KamLAND) it is important to be able to clearly distinguish and identify all simple events in a physics event.

We have identified the following major requirements for the KamLAND front-end electronics:

- *Threshold:* The lowest possible simple event threshold is certainly an essential ability of KamLAND. With a light yield of $\sim$ 150 s.p.e. per MeV, and with a capability of PMTs to detect a single photoelectron the lowest energy trigger threshold will be determined by PMT thermal noise (ranging from 5 kHz to 90 kHz per PMT) and by low-energy γ background. Figure 30 shows the expected trigger rate in Kamland with 1280 PMTs, as a function of global threshold in s.p.e. From this point of view a global simple event threshold of $\sim$ 0.25 MeV ($\sim$ 40 s.p.e.) is well within the possibilities.

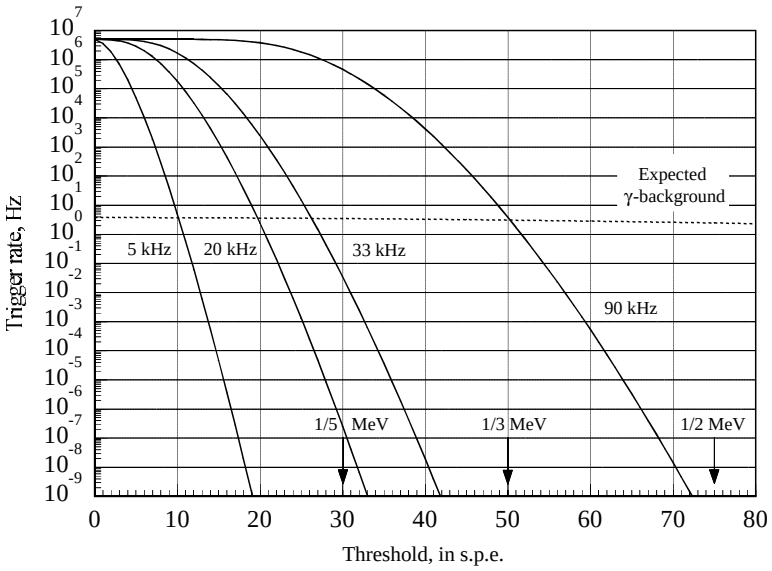

Figure 30: Trigger rate vs threshold in single photoelectrons for different assumptions on the average dark current noise per PMTs. We assume 1280 PMTs, overall light yield of 150 s.p.e./MeV, and trigger resolution time of 200 ns. Also shown is the γ-background rate for natural radioactivity.

- *Trigger rate and dead time:* One of the limitations of high trigger rates generally associated with low trigger threshold is an increase of the dead time due to

event conversion and readout. The specific type of front-end electronics used for signal processing and readout can reduce the dead time virtually to nil, even at trigger rates as high as a kilohertz. In particular, high trigger rate capability is also required for the efficient detection of supernova neutrino-events where the trigger rate can be as high as a kilohertz for a time interval of several seconds.

- *Multi-hit capability:* Multi-hit capability is required for the time and amplitude measurement of a sequence of simple events with a separation in time smaller than or comparable to the digitization and read-out time interval. Thus, the neutron following the positron signal in reactor anti-neutrino events will be detected within a $\sim 500\mu$s time interval (average capture time in liquid scintillator is $\sim 180\mu$s) comparable with the event read-out time. An extreme example of the multi-hit requirements is given by SUSY-preferred proton decay modes, such as the one shown below, where energy and space positions need to be measured for four simple events closely separated in time:

$$
\begin{aligned}
p \rightarrow K^+ + \overline{\nu}_\mu & \\
\downarrow\ & \text{12.4 ns} \\
K^+ \rightarrow \pi^+ + \pi^0 \rightarrow \gamma + \gamma & \\
\downarrow\ & \text{26 ns} \\
\pi^+ \rightarrow \mu^+ + \nu & \\
\downarrow\ & 2.2\ \mu\text{s} \\
\mu^+ \rightarrow e + \overline{\nu} + \nu &
\end{aligned}
$$

  The clear detection of these final states poses substantial requirements on the multi-hit ability of our electronics system.

- *Bandwidth:* Since the risetime of the PMTs is $\sim$ 7 ns and, in addition, $\sim$ 40 m of coaxial cable RG-303 between PMT and the processing electronics will be used, an overall risetime of $\sim$ 8 ns should be expected. This will imply that the bandwidth of the processing electronics does not need to exceed significantly $\sim$ 50 MHz.

- *Dynamic range of amplitude measurement:* The range of amplitude measurements is limited on the lower side by the necessity of s.p.e. detection (we assume that the s.p.e. signal will be digitized as $\sim$ 50 ADC counts above the pedestal) and on the higher side by the energy of the stopping muons ($\sim$ 1000 s.p.e. per PMT). We assume a maximum amplitude per PMT of 2000 s.p.e., which gives a conversion dynamic range of ADC of 100,000 and a maximum measurable energy in the detector at the global saturation level of $\sim$ 17 GeV. Energy deposits larger than 10 GeV in the detector are only possible from high-energy hadronic or electromagnetic showers originated by neutrinos or muons. To cover

the dynamic range of 100,000 (17 bit), one will need at least two 11-12 bit ADC conversions per PMT corresponding to high and low sensitivity range.

- *Time resolution:* Since the transit time spread (TTS) of a R7250 PMT is 3.5 ns FWHM and the fast decay time constant of the liquid scintillator is a few nanoseconds, an accuracy of the time measurement in each individual channel of ~ 0.5 ns should be adequate. Overall an off-line space point reconstruction accuracy of ≤ 10 cm FWHM (at 1 MeV) will result from averaging the timing information from several PMTs in an event.

- *Range of time measurements:* Within a simple event the required time interval range for measurements between different PMTs, as well as the signal length for individual PMTs, is in the range of 100 ns. For physics events, as was mentioned above, the required time intervals between simple events can be from tens of nanoseconds to minutes. It is important that for each simple event the amplitude, the arrival time, and the signal duration are recorded. This requires an electronics either with very fast conversion/readout, or with long-sustain-time analog memory, or with 2-3-fold split parallel processing of the signals. We note that from the electronics point of view, many types of background should be retained for later analysis. This is particularly relevant in order to reach the ultimate lowest global threshold for the experiment.

5.6.1 Preamplifiers

The anode current response of the Hamamatsu R7250 PMTs becomes non-linear above $\sim$ 10 mA in the pulse mode. The limitation occurs mainly due to space-charge effects in the last dynode-dynode and dynode-anode gaps. The maximum linear current corresponds to a signal of $\sim$ 500 mV for a 50 Ω cable load. With the essential requirement of the efficient detection of single photoelectrons and with a maximum detectable amplitude of $\sim 2,000$ s.p.e. per PMT, the s.p.e. signal at the end of a 40-m-long transmission line will be only ~ 0.25 mV. The corresponding charge of ~ 100 fC is somewhat small for reliable signal/noise separation. To extend the dynamic range of the anode signal of the PMT, we will use a buffer preamplifier at the anode. The connection scheme of such an amplifier is shown in Figure 31. The high input impedance and low capacitance of the buffer amplifier allows us to use a 1KΩ anode load instead of the conventional 50Ω. In this way the 10 mA current limit of the PMT will yield a signal of 10 V, and the single photoelectron signal will give a comfortable amplitude of ~ 5 mV, extending the dynamic range of the anode signals by a factor of 20.

There are several buffer amplifier chips available on the market. One of the possible compromises between speed and power is the LM6125[84]) with a 50 MHz bandwidth (rise time ~ 7 ns), and current-drive capabilities up to 300 mA into a 50Ω load. The input resistance of the LM6125 is 5MΩ, its input capacitance 3.5 pF, and the

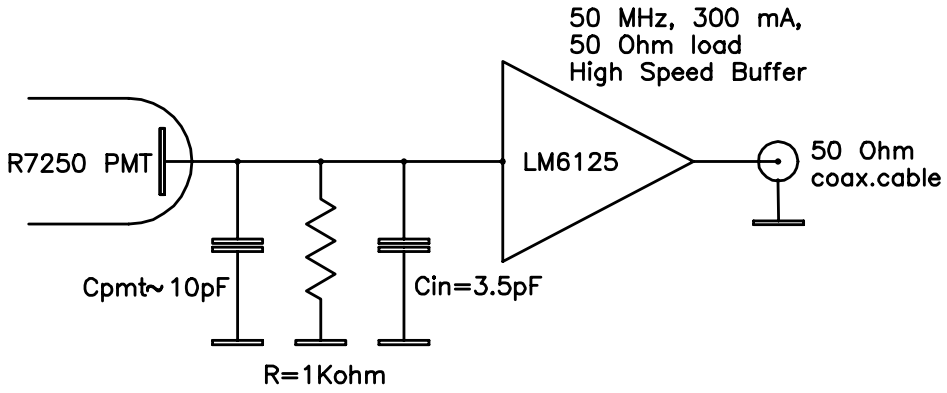

Figure 31: Amplifier-buffer mounted at the anode of PMT can extend the linear dynamic range of output signals up to ~ 10 V with a 50-ohm load.

maximum power dissipation of 0.4 W. The latter can be compared with the power dissipation of ~ 1 W for the regular resistive PMT voltage divider.

We expect the rise time of the anode pulse to be a convolution of the PMT rise time (~ 7 ns) and the buffer amplifier response time (~ 7 ns in case of LM6125). The fall time should be determined mainly by the discharge time of the anode capacitance (~ 10 pF + 3.5 pF input capacitance of the buffer) through the anode load resistor (1 KΩ), i.e., will be ~ 15 ns. The prototyping of the preamplifier at the anode of a R7250 PMT, in progress in our laboratories, will determine whether the actual speed of this system is sufficient or a faster amplifier will be needed.

5.6.2 Front-End Electronics

In order to fulfill the requirements discussed above, as well as the cost and schedule of the experiment, we are considering two options for the front-end electronics. Prototyping for both options is in progress and a final decision will be taken in the next several months.

The first option is built around conventional, commercially available ADC and TDC modules. Deadtime-less operation only for the first two simple events of a real event will be achieved by fast switching of the trigger controls between two banks of equivalent front-end electronics, as shown in Figure 32.

Additional flash-ADC readout is also envisaged for analog sums of groups of 8×8=64 PMTs. The trigger will be based essentially on the multiplicity of single hits. This approach to the front-end electronics has been very well tested in Kamiokande, Chooz, and Palo Verde and represents an excellent fall back, safe solution, although, for a very large multipurpose detector such as KamLAND it would limit the capabilities of the experiment, mainly in the important fields of supernova detection, nucleon decay and, in general, particle identification.

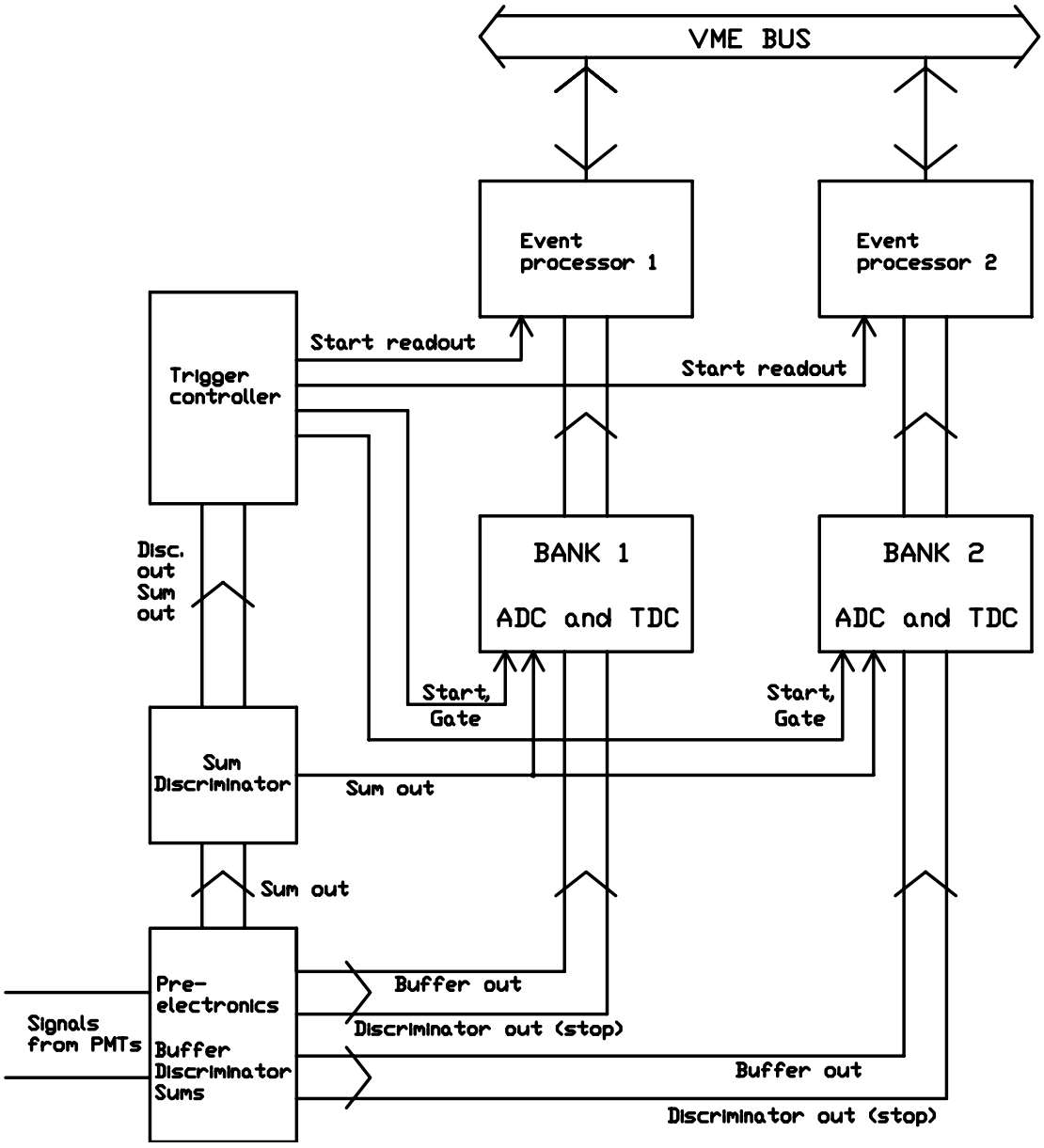

Figure 32: Option 1 front-end electronics with two banks of ADC and TDC can provide deadtime-less operation for the first two simple events.

The second front-end electronics option will have essentially none of the limitations of the first, but, being technologically more advanced, requires an aggressive design and prototyping effort.

The electronics concept in this second option is based on the novel approach [86] pioneered by some members of our Collaboration. The system uses a monolithic analog memory ASIC chip (AMU - analog memory unit)[87] including 32 channels of random-access precision analog memory, each with 64 storage cells (time slices). The sampling and recording frequency of the AMU chip is 10 MHz (or one measurement/storage every 100 ns). Each of 32 channels has a built-in ADC, which allows conversion of any or all of 64 stored analog measurements into 11 bits ($\sim$ 15μsec conversion time). Simultaneous read-write capability and the flexible memory address list manager (MALM) will allow deadtime-less data acquisition in KamLAND at trigger rates even above 1 kHz, and with built-in multi-hit performance.

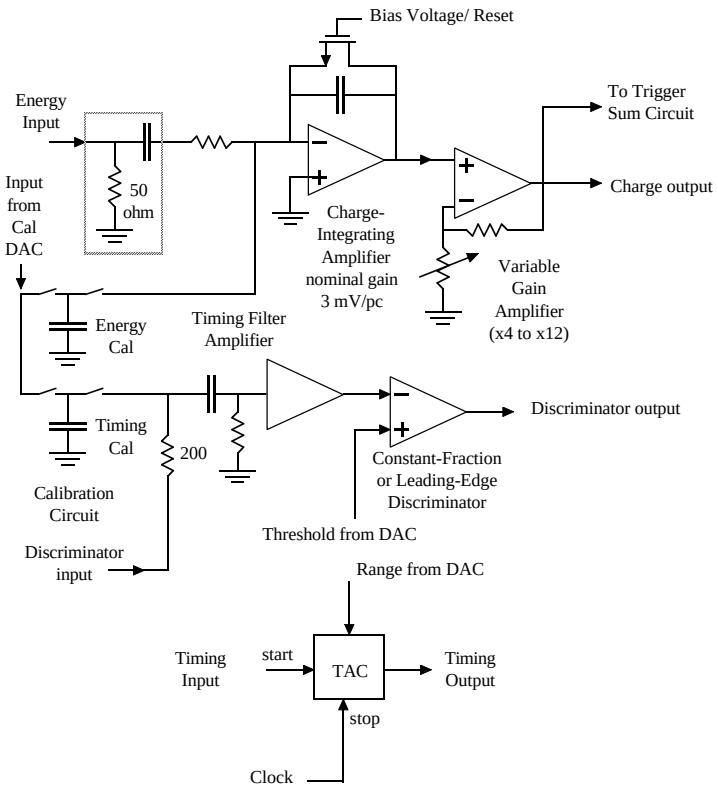

Figure 33: Concept of Kamland instrumentation chip in Option 2. One channel out of 8 in a chip is shown.

The second important component in this option is another monolithic ASIC, that we call "instrumentation chip". This device, shown schematically in Figure 33, con-

sists of 8 identical signal processing channels, each including constant fraction discriminator, charge-integrating amplifier (CIA), programmable gain amplifier, and time-amplitude converter (TAC). Each chip also has calibration circuitry, 2×4 analog sum outputs for triggering, and the serial controls. One instrumentation chip can provide an input for 16 AMU channels.

The principles of operation of this electronics for the measurement of amplitude, arrival time, and signal width are illustrated in Figure 34. The electronics operate with a stable free-running 10 MHz clock. The clock is synchronized with a "Universal Time Standard"and provides an absolute time stamp to the headers of digitized and recorded events. Fast PMT signals arrive via 50 Ω RG-303 cables $\sim$ 40 m long to the receiving buffer amplifier/analog splitter as shown in Figure 35. Various measurable parameters of the input signal (charge integral, arrival time, signal length, etc.) are formed and converted into amplitude information by the instrumentation chip. The various amplitudes are then sampled every 100 ns and stored in the AMU as a sequence of time slices.

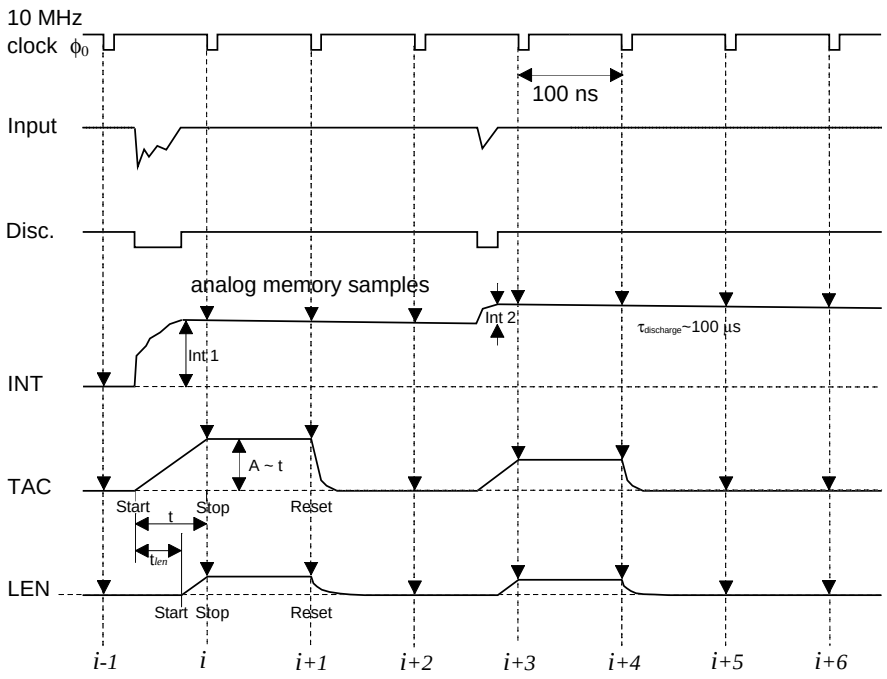

Figure 34: Simplified timing sequence of integrated charge, arrival time and pulse width measurements for readout option 2.

The PMT current signals are integrated by a charge-integrating amplifier in the instrumentation chip (INT time diagram in Figure 34). The charge-integrating am-

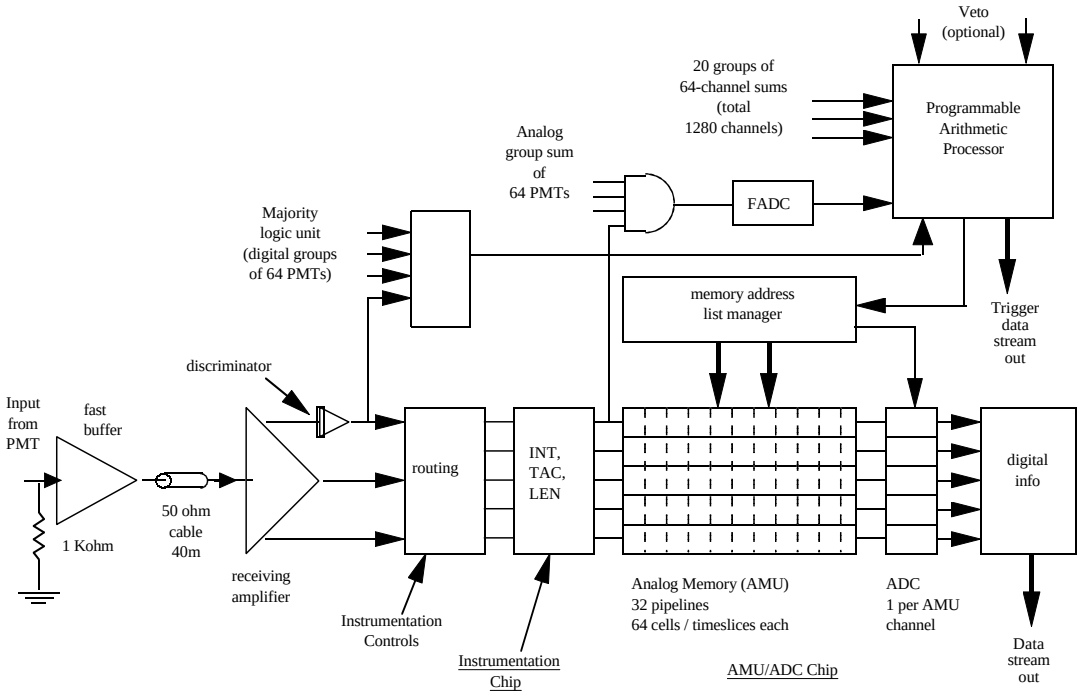

Figure 35: General concept of option 2 front-end electronics.

plifier is set to discharge the integrated signal with an RC of the order of a hundred μseconds, which should be chosen to match the average anode current of the PMT and to prevent the saturation of the integrated output. Several signals are allowed to be integrated and overlapped at the CIA output within a discharge time interval. The reading of any particular integrated signal corresponding to the i-th 100 ns time interval is obtained as an amplitude difference of i-th and (i-1)-th digitized samples .

The measurement of the arrival time is performed in the following way. An analog PMT signal triggers the discriminator (with the threshold corresponding to 0.2-0.3 s.p.e.). The leading edge of the discriminator output starts the integration of a constant current in a capacitor. This process lasts until the next clock cycle (TAC in Figure 34) so that the integrated amplitude is proportional to the time interval between the start of the signal and the next clock time signal. The integrated amplitude level is held for the next clock cycle, to allow the storage of its value in the AMU, and then resets during the following clock cycle. Thus, the arrival time measurement requires three clock cycles ($\approx$300 ns). The signal length can be measured similarly (LEN in Figure 34). In the latter case the integration is started by the trailing edge of discriminated PMT signal and stopped by the next clock signal. To provide time measurements for several simple events separated by the time intervals less than three clock cycles, up to four hits per PMT channel can be processed in parallel channels for leading and trailing edges of the PMT signals.

All time intervals will be measured with an electronic accuracy of $\sim$ 0.3 ns [86] which will not contribute significantly to the overall time measurement accuracy of $\sigma \sim 1.5$ ns determined by PMT time resolution.

Parallel to processing in the AMU, the integrated analog signals are also summed into 20 groups of 64 channels (see Figure 35) for fast flash ADC digitization. Flash ADC will provide an energy deposit signal (in the group of 64-PMTs) to be fed to the trigger processor. Discriminator outputs for individual channels will also be fed to the trigger processor for pattern recognition.

The trigger signal which originates with about 2 μs delay after the simple event in the detector will command the analog memory address list manager (MALM) to mark the time slices containing useful events for digitization. With 64 time-slices-deep AMU, 10 MHz clock, 2 μsecond trigger latency, and with 4 useful time slices per simple event, a trigger rate of up to 10-15 kHz should provide practically deadtime-less conversion/read-out operation in each channel of the system.

To cover the whole dynamic range of amplitudes from a PMT, two parallel integrator-AMU channels will be used with different sensitivity providing two ranges of conversion: 50 ADC counts/s.p.e. and 1 ADC count/s.p.e., respectively. If the high-sensitivity range is saturated the high-sensitivity integrator will be reset (see Figure 33) during the next 100 ns cycle.

As an example of the power of this system we show in Figure 36 the timing sequence deriving from the already mentioned $p \to K^+ + \overline{\nu}_\mu$ decay chain. We assume a very extreme case in which the K decays in 12 ns, the π after 26 ns and the μ earlier

than 2.2 μs. The entire event is reconstructed (including PSD) without any loss of information or pile-up effects unless the decay time interval will be too short to be separated by PMT pulse duration.

Signals from the PMTs in the veto system will be readout in a similar fashion. Since the counting rate of the veto-system is not expected to exceed a few Hertz, we anticipate that veto signals will not be used in the trigger decision but will be recorded in the general data stream with appropriate synchronization time stamp for the off-line correlations.

5.6.3 Trigger and Data Acquisition

The trigger in KamLAND could simply be based on a global threshold for the total energy deposit in the detector. A trigger rate below 10 Hz should be possible with a global threshold of ~ 0.3 MeV. A set energies from several large PMT patches and/or the hit pattern from small clusters of PMTs may be used in addition to accept or reject special categories of events.

Since the maximum duration of the PMT signals and the time difference between PMTs are both ~ 100 ns, a trigger resolution time of ~ 200 ns is appropriate. That means that all data required for the trigger of each simple event will be contained within a $\sim$200 ns time interval.

There are some differences in the trigger organization for two options of the front-end electronics which were discussed in the previous section.

For the first option, the trigger decision time should be as short as possible to save cable length in each PMT channel (used for compensation of the trigger delay). Trigger decisions here will be made by forming the local analog sums of the anode signals in groups of 16, and then by discriminating the integrated-in-time summed signal of all PMT groups (corresponding to 1280 PMTs). Readout dead-time will limit the trigger rate and might require adjusting the global threshold to the higher values or implying a specific coincidence between the first and second simple event triggers in a real event. In the latter case, the global trigger becomes non-universal, and some physics processes based on a single, simple event counting might be sacrificed. Trigger/read-out rate limitation may also affect the efficiency of events registration in supernova bursts.

For the second front-end electronics option, a trigger latency of $\sim 2-4\mu$s will be acceptable, and a universal trigger with lower threshold and with more sophisticated event recognition can be accomplished. Readout will be deadtime-less for trigger rates up to 1 kHz. Considerable experience exists in our collaboration with the design and implementation of the trigger processors [88].

Data acquisition (DAQ) is also somewhat different for the two front-end options, particularly due to the fact that the amount of information per simple event is larger by an order of magnitude in the second case. Here we will concentrate on this second, more demanding, system that will require some custom development. Experi-

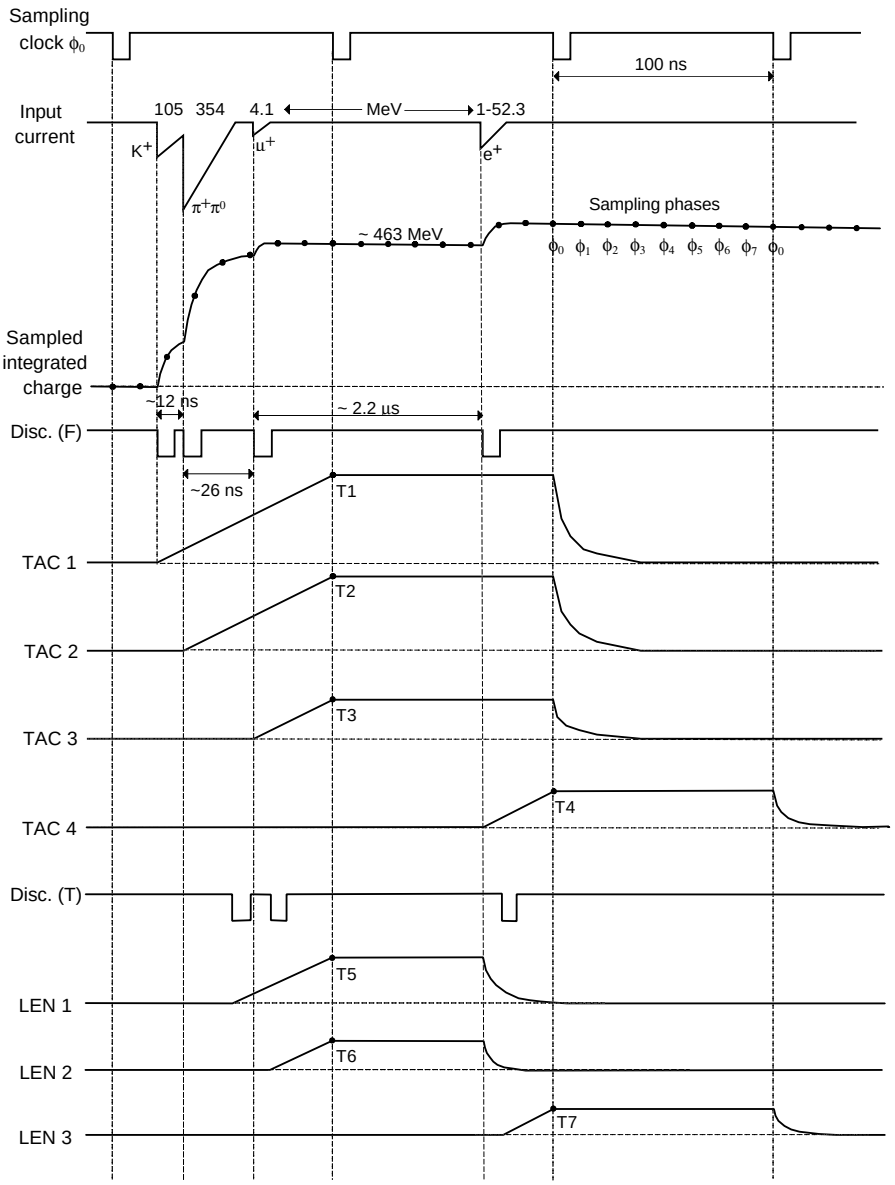

Figure 36: Example of detection of a proton decay chain $p \to K^+ + \nu$; $K^+ \to \pi^+ + \pi^0$; $\pi^0 \to \gamma + \gamma$; $\pi^+ \to \mu^+ + \nu$; $\mu^+ \to e^+ + \nu + \overline{\nu}$ in the option 2 of Kamland front-end electronics.

ence on design and implementation of DAQ systems of this type is available within collaboration[86]. One of the essential issues to be resolved here is the synchronization of the information used by the analog memory address list manager with absolute time provided by Universal Time Standard.

Figure 37 is a diagram showing the organization of the KamLAND electronics into crates. The crates will contain three types of cards. The first, called "front-end card", contains all the electronics necessary to process 16 PMT signals into various energy and timing values and to digitize them. This card includes 16 instrumentation chips and 16 AMU/ADC chips. Data from 16 front-end cards would travel on a data bus to the second type of card, the "data collection card". This card contains a FIFO memory to buffer the data received from the front-end cards before transfer to the next level of readout. It also contains the memory address list manager (MALM) which controls the reading and writing of the AMUs and the conversion process and readout of the ADCs. The third type of card is the "trigger card". Analog energy signals developed on the front-end cards pass over the trigger data bus segments and are summed by the trigger card. The trigger card completes the processing of trigger information for groups of 64 PMTs and passes that data to the next level of the trigger processor. The entire crate processes the signals from 256 PMTs, so approximately 6-7 crates would be required for all of KamLand FEE including veto PMTs.

Data from the data collection card would pass over several high-speed parallel busses to a VME-based processor. A similar arrangement was used for CERN experiment WA98 and data transfer rates up to 20 Mbyte/s were possible with a single bus. For a single physics event of a maximum complexity, there are 32 words of data from each energy channel (16 analog samples per 200 ns $\times$ 2 gain ranges) and 16 words from each timing channel (4 samples $\times$ 2 for leading and trailing $\times$ 2 for two clock phases). The total is 48 words per PMT-event, but that should be rounded up slightly in calculating total data rates to allow for headers and other incidental data. Assuming 64 words per PMT-event, two bytes/word and an average event rate of 10 Hz, the data rate for a single PMT comes to 1280 byte/s. For a 256-channel crate, the average data rate would then be 328 Kbyte/s (or 32.8 Kbyte per event). For a supernova, the event rate could potentially go to 1 kHz, and the data rate would increase to 32.8 Mbyte/s for perhaps one second. This data rate could be handled by using two of the 20 Mbyte busses or larger size FIFO memory on the data collection cards. Since the bulk rate of triggers will correspond mostly to the single γ background events with energy deposit $\leq$ 10 MeV (or average signal level $\leq$ 6 s.p.e. per PMT) a simple zero-channel read-out suppression algorithm can substantially reduce the size of the data stream.

5.7 Veto Counter

The water pool outside the sphere serves two important functions. As a passive shield it absorbs the radioactivity coming from the walls and degrades the energy of the fast

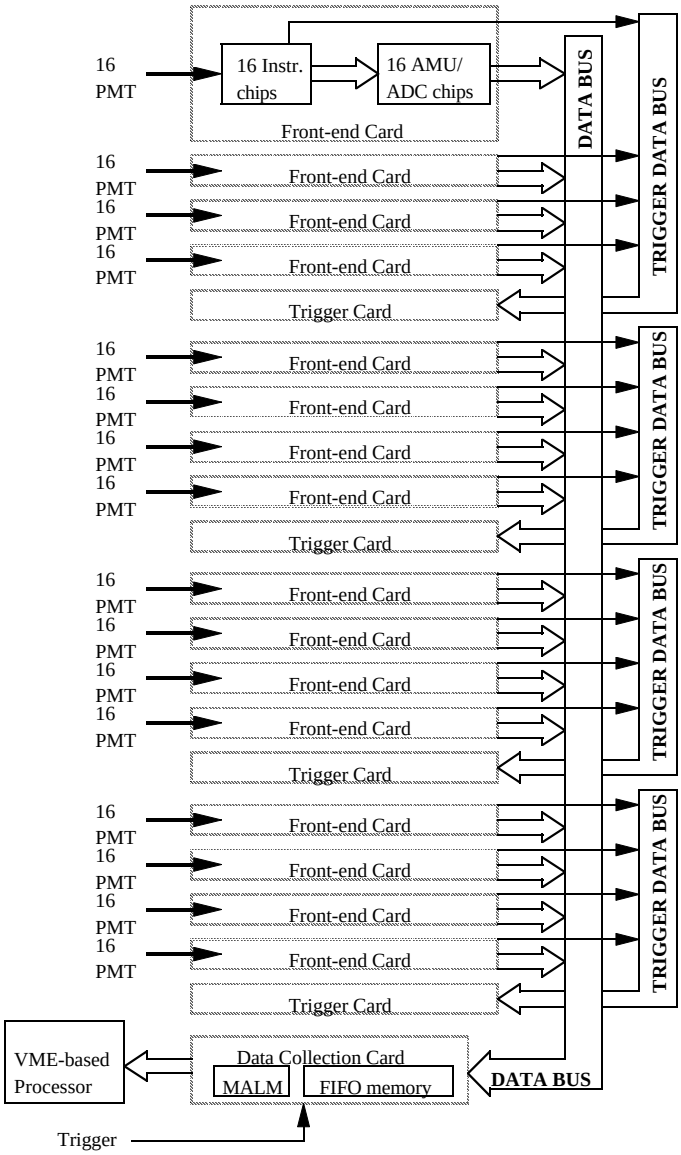

Figure 37: Organization of the front-end electronics into crates for option 2. One VME crate, shown in this Figure, will process data from 256 PMTs.

neutrons produced by cosmic rays in the rock. As an active veto it detects cosmic ray muons traversing it by their Čerenkov radiation.

Since the geometry of the veto detector is quite complex and anyway there is no need to extract precise information from the properties of the Čerenkov light, we are planning to randomize the light direction applying a white diffusing material to the sphere and walls of the cavern. This will eliminate potential "dead" zones of the detector from where mirror reflection could guide light systematically away from photomultipliers.

The veto will be readout using 20-inch photomultipliers recycled from the Kamiokande experiment. As shown in Figure 22 we are planning to cover each of the top and bottom "pancakes" with 89 tubes arranged in a square lattice. This corresponds to about 6% photocathode coverage of the top and bottom surfaces and, with a minimum water depths of 1 m would result in about > 230 photoelectrons directly collected for a high energy muon. In reality this figure will be increased by the diffusing material. A light gauge aluminum box around each of the tubes will produce a modest segmentation in the pancakes and allow for crude tracking of cosmic-ray muons. The situation is somewhat more complicated in the side veto, an option of which is schematically shown in Figure 23. In order to be conservative in shielding the active scintillator from the central detector photomultipliers, little space (50 cm) is left between the equator of the sphere and the rock. This space would not allow direct mounting of 20-inch PMTs, that would anyhow displace too much water shielding in this critical area. The simple scheme represented in Figure 23 consists of 20 vertical strings, each supporting 8 20-inch tubes and gives a photocathode coverage of 2.6%. Although this coverage is more than adequate for the long path lengths covered by most muons, only 50 direct photoelectrons would be detected for muons traveling horizontally through the equator. Monte Carlo studies with detailed geometry and cosmic-ray flux distributions as well as measurements in a small water pool will be performed in order to decide whether this scheme is sufficient for our purpose. We are studying three alternatives to improve the situation in the equatorial region:

- increase of the number of PMTs and hence of the light collection by providing more strings and mounting tubes also on the outside of the sphere. This would be inexpensive as plenty of tubes are available from Kamiokande, however it is possible that these tubes are indeed too large to effectively collect light from such a peculiar region of the detector;

- install about 100 8-inch tubes around the equator;

- use a fluorescent coating or hang very thin "curtains" of plastic scintillator in the equatorial region in order to shift some of the Čerenkov light from the UV to longer wavelengths visible from the photomultipliers.

Each PMT string will be optically isolated from the others (and from the top and bottom pancakes) using aluminum septa, to provide some segmentation.

Finally a plastic scintillator "roof" will be built above the system of chimneys that provide access to the central detector. This roof will be mounted on a cart so that it can be rolled away for calibrations or other support operations.

5.8 Calibration and Monitoring Systems

The calibration and monitoring system for the KamLAND experiment carries out measurements of the detector performance required to (a) convert observed pulse heights to energy depositions and their times and positions, (b) optimize the discrimination between signal and background, and (c) estimate detection efficiencies to an accuracy better than 3%, at least for efficiencies relevant to reactor anti-neutrino measurements. The system consists of overlapping techniques, so that cross-checks can be made and the calibration and monitoring program can be easily adapted to the detector needs based on actual running experience. In the description below, emphasis is placed on calibration and monitoring for detection of low–energy anti-neutrinos from reactors and terrestrial radioactivity and neutrinos and anti-neutrinos from supernovae. Such emphasis follows from the priority which these processes have in the KamLAND physics program and that their requirements on calibration and monitoring are representative of practically all processes which KamLAND will study in the 0.5–50 MeV energy range. Detector calibration for the study of higher–energy processes, e.g. nucleon decay and atmospheric neutrinos, is briefly described at the end.

5.8.1 Overview

As already discussed in detail, physics events can be decomposed, in our detector, in successions of simple events. The response of the detector to the signal and background processes can be understood from measuring its response to each of the relevant simple processes. For detection of $e^{\pm}$ and γ over the relevant energy range, it suffices to carry out calibrations with γ sources: energy depositions of $e^{\pm}$ and γ in scintillator are understood well enough so that detector simulation tuned to the γ calibration data reliably models the detector's response to $e^{\pm}$.

The calibration and monitoring system will consist of the following components, which are described in detail in the following sections:

1. **Gamma Sources**. Calibrated gamma sources, mono-energetic and point-like, spanning, for sake of simplicity, the energy range from 0.5 MeV to ∼6 MeV would be positioned at different locations within the detector volume. Data from such sources will be used to directly measure the energy response as a function of position and to tune/check the detector simulation program used to calculate the positron detection efficiency. In particular, the capability to place the source at any position will be exploited for understanding the effect of fiducial volume cuts on detection efficiency.

2. **Neutron Sources**. Similar to the γ sources, calibration data would be taken with neutron point sources positioned at various points in the active detector volume. These measurements would be used to estimate the neutron detection efficiency and to improve PSD as a way to suppress background.

3. **Alpha sources**. We will expose the detector to α sources in order to measure *in situ* the quenching factor and PSD.

4. **Light Flasher System**. Sources of short light pulses having the same spectral profile as scintillation light will be placed at different positions inside the detector. With a dynamic range of one to several thousand photoelectrons per PMT we will be able to study single photoelectron gain, PMT timing (including walk corrections), PMT gain linearity and scintillator stability on a rather frequent basis.

5. **Cosmics**. Cosmic-ray muons which stop in the detector and decay provide a well–known Michel spectrum with endpoint energy 52.8 MeV. The Michel electron energy spectrum will be used to measure the detector response at the higher energies relevant, for instance, to supernova neutrino detection. Although limited in statistics, stopping muons which are captured on nuclei provide another means of measuring the neutron detection efficiency.

5.8.2 Gamma Sources

The gamma sources are primarily intended for calibrating the response of the detector to gammas and positrons in the energy range 0.5–$\sim$6 MeV. The set of sources we plan to use is ^{137}Cs (0.662 MeV), ^{54}Mn (0.835 MeV), ^{65}Zn (1.116 MeV), ^{60}Co (2.506 MeV), Am–Be (4.43 MeV), and one additional source, yet to be selected, to provide a calibration point between 5 and 10 MeV. (One candidate source for the high energy point is Cf–Ni, which consists of a set of discrete gamma emission lines between 6.8 and 9 MeV.) Since Am–Be emits a 4–8 MeV neutron together with the 4.4 MeV gamma, the source should be surrounded by a moderator, e.g. paraffin, so that an appreciable fraction of the events are not contaminated by proton recoils. In principle, calibration data from one source combined with measurements from the light flasher system would be enough to calibrate the detector response, however, given the importance of accurately measuring the energy distribution of positrons in the 1–6 MeV range, we think it prudent to directly measure the detector response at several different energies. It should not be necessary though to perform detailed measurements with every source; for example, to determine position scaling and understand the effects of fiducial volume cuts, it should suffice to carry out measurements at many different locations only for two sources, a low–energy one and a high–energy one.

Several schemes for positioning the sources within the central volume are under consideration. A simple solution would be to use a boom system, comprised of folding and telescoping parts, supported from the chimney and which can be fully retracted

when not in use. The location of the source could be determined from positions of the cables used to manipulate the boom and/or it could be found by fixing an ultrasound generator to the source carriage and detecting its signal with pickups fixed at different locations around the periphery of the detector. This is schematically shown in Figure 38.

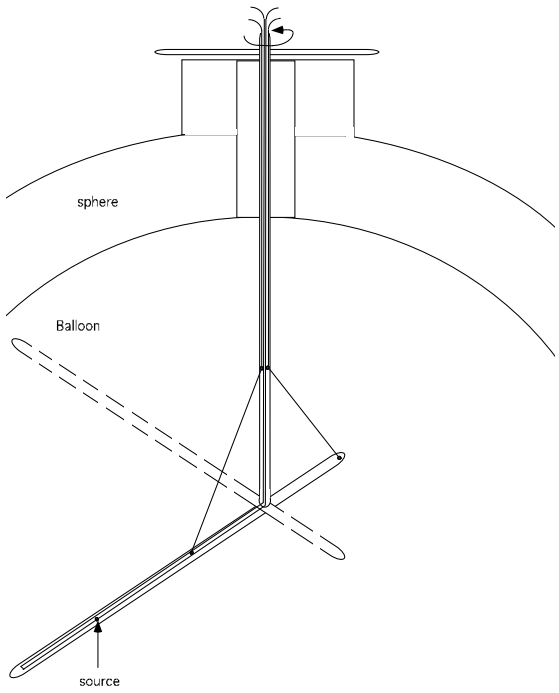

Figure 38: Telescoping boom and arm under consideration for positioning various sources inside the detector. This simple system could reach virtually any position inside the balloon by operating few cables on the outside. The system would be retracted during normal data-taking.

Another scheme would be to mount the sources onto a small, self-propelled, remotely controlled submersible with information on the position obtained by an ultrasound tracking system. This second option requires substantially better technology but it could improve our ability to reduce radon contamination during the insertion of the calibration hardware.

In either scheme care has to be taken while changing positions not to agitate the scintillator to the point that its optical properties are temporarily affected. We are also studying the possibility of automatizing the schemes described in view of the number of sources and the range of positions covered. Source positions will be known with an absolute accuracy better than 5 cm. The source data taken at different positions will also be used to cross–check the reconstruction of event location from

timing information.

The activity of the sources will be chosen to give an event rate which is well above the expected background event rate and yet below the rate at which uncertainties in DAQ deadtime corrections become significant. The activities of all sources will be calibrated to an accuracy of 1%.

The sources will be encapsulated so that any undesirable γs (e.g. 60 keV γs in the case of Am–Be), β's, and α's are ranged out. The capsule sizes will be kept as small as possible in order to minimize occlusion of scintillation light.

We plan to carry out the calibration with the gamma sources at the beginning and the end of the experiment. Additional calibrations will be carried out at intermediate times as needed based on monitoring results.

5.8.3 Neutron Sources

While we expect the neutron detection efficiency to be high and easy to simulate reliably for inverse beta decay events within the fiducial volume, a direct measurement is very important to minimize systematics in our measurements. Two neutron sources under consideration for this purpose are ^{252}Cf and Am–Be, both of which can be prepared and sealed in capsules as described above for the γ sources. ^{252}Cf is a fission source that produces about 20 gammas and 4 neutrons, on average, per fission. One may trigger on the prompt energy deposit from the gammas or a neutron capture and then measure the number of neutrons subsequently detected within a defined time window. The average number of neutrons detected and the mean time between captures can be folded with detector simulation to calculate the neutron detection efficiency. Am–Be is a somewhat simpler source in that for each 4.4 MeV gamma produced, one neutron is produced. One can then collect a sample of events triggered on the 4.4 MeV gamma (plus energy promptly deposited by the neutron) and then calculate the neutron detection efficiency from the subset of events in which there is a delayed coincidence with a 2.2 MeV gamma. To obtain events cleanly triggered by the 4.4 MeV gamma, we could attach a small NaI detector to the source and require that it detect the 4.4 MeV gamma.

A complication for both these sources is that the neutrons produced typically have energy of a few MeV and therefore will travel further before thermalization than the neutrons from the inverse beta decay induced by low–energy anti-neutrinos. Consequently, the detection efficiency for these neutrons must be scaled (by simulation) to take into account effects like position cuts between prompt and delayed events. Although the systematics due to these corrections will probably be very small we are also exploring the possibility of fabricating low–energy neutron sources. One candidate is Sb-Be, which emits neutrons whose average kinetic energy is on the order of 10 keV. Such a source, which emits only single neutrons, must be calibrated to an accuracy of a few percent for our purpose. These measurements can also be carried out with sources permanently installed in a smaller detector connected in the flow of

the scintillator through the purification system of the main detector. We are surveying other neutron sources with no or very low energy accompanying γ radiation for the purpose of PSD and quenching calibration.

The mechanics for positioning the neutron sources would be the same used for the gamma sources. We also envisage similar calibration intervals.

5.8.4 α sources

As already noted many backgrounds are related to decay chains including α emitters. For this reason it is quite important to understand well the the properties of energy depositions by α particles. Given the great danger involved in handling α sources with very thin sealing layers in our detector we are considering two independent ways to address this calibration.

One possibility would be to build a transparent container with walls of similar index of refraction as the scintillator, filled with scintillator sampled from the main detector. A small short-lived α source can then be dissolved in the scintillator (^{220}Rn, with a half-life of 56 s is a possible candidate). The container can then be moved through the KamLAND scintillator with the same system used for the other sources with no risk of contamination since the source is contained by a thick wall and anyway the isotope has a very short half-life.

In addition during the normal data-taking of the experiment α decays from ^{222}Rn contamination in the detector will also provide a source of calibration. Although its position is not known a-priori this "calibration source" is active during the entire life of the experiment and it can give valuable information once the coordinates of the decayed nucleus are extracted from the time of arrival information like it is done for neutrino events.

5.8.5 Light Flasher System

The purpose of the light flasher system is to calibrate the PMT timing, balance the gain of the PMTs and determine the linearity of the PMT response (including downstream readout chain). It will further be used to monitor scintillator transparency and it will be a useful tool for commissioning and checking the detector readout. To carry out these tasks, the light flasher system must have the same spectral profile as the scintillator light, short pulses, be variable in amplitude, and provide point sources which are at varying distances from the PMTs.

The burden of the above tasks will be mainly borne by a laser–based system similar to one being used by the Chooz experiment. In this system, UV light pulses (3 ns width) from a nitrogen laser are injected into a bulb of scintillator which is viewed by the detector as shown in Figure 39.

The wavelength of the laser light falls within the absorption band of PPO, hence light is emitted having the same characteristics as scintillator light. As shown in Figure 40, the laser light is transmitted to the scintillator bulbs via quartz fiber

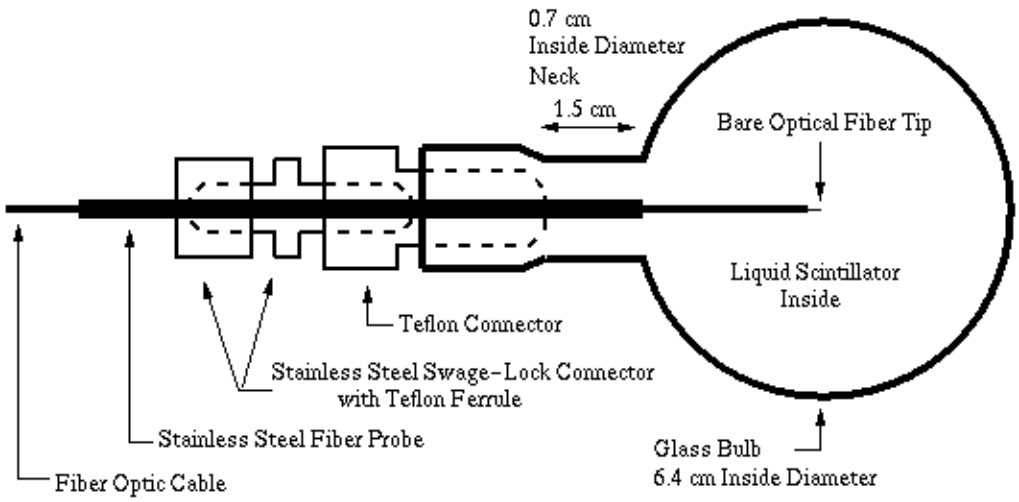

Figure 39: Fiber–scintillator assembly for injecting UV laser light via fiber into the scintillator cell to obtain a nearly isotropic source of scintillator light.

optics and its intensity is modulated with computer–controlled attenuator wheels and monitored using source–stabilized photodiodes and PMTs. We plan to locate 8 bulbs at regularly–spaced locations on the PMT support sphere to be used for daily monitoring of the scintillator transparency and to attach one bulb to the source positioning assembly in order to be able to flash the detector from the same position where the sources are during the occasional source calibrations. Since the extreme purity of the scintillator does not permit us to leave permanently objects in the central detector one more bulb will be mounted on a tether so that it can be easily deployed from its "parking" position in the chimney. This bulb will be used when it is important to emit light in the same optical configuration, e.g. with the same reflections from the balloon and PMT faces, of the scintillation light.

The laser flasher system is limited in rate to 20 Hz, and therefore, we will also install an LED system to carry out tasks for which accurate knowledge of light intensity is not required but would benefit from high repetition rate. These tasks include gain balancing the PMTs, debugging the detector readout, and monitoring the single photoelectron gains. A similar LED system will be also used to monitor the muon veto system.

5.8.6 Cosmic-Ray Muons

Michel electrons from the decay of muons at rest have a well–known energy spectrum which can be used to measure the detector response up to 50 MeV. The rate at which muons stop in the detector is of the order of 0.001 Hz and nearly all of the stopped

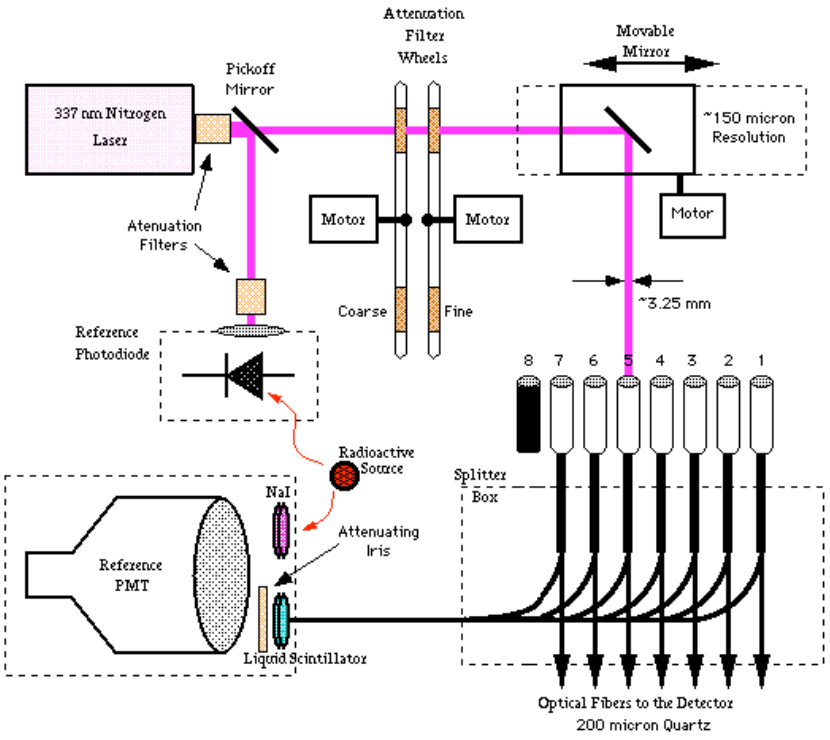

Figure 40: Schematic of system for controlling and monitoring the laser flasher system.

muons decay. Consequently, one has about 100 muon decay–at–rest events per day. This rate is clearly too low for dedicated runs, but event samples of useful size can be accumulated with a dedicated trigger for stopped muons that is OR'd with the other experimental triggers.

In addition about 8% of negative muons which stop in the KamLAND central detector are captured on ^{12}C nuclei through one of the following reaction channels:

$$\begin{aligned} \mu^- + {}^{12}\mathrm{C} &\rightarrow {}^{12}\mathrm{B} && (17\%) \\ &\rightarrow {}^{11}\mathrm{B} + \mathrm{n} && (78\%) \\ &\rightarrow {}^{10}\mathrm{B} + 2\mathrm{n} && (5\%) \end{aligned}$$

Triggering on the stopped muon, the latter two channels can be exploited to measure the neutron detection efficiency. Although the rate of useful events ($\approx$ 3/day) is quite modest, neutrons produced in this way and accumulated over two or three years have the potential of allowing a measurement of the time–averaged neutron detection efficiency with an accuracy of 2–3%. This technique has been demonstrated by the KARMEN [89] experiment by measuring its neutron detection efficiency with an accuracy of a few percent.

5.8.7 Detector Calibration at Higher Energies

The KamLAND physics program includes search for proton decay and other higher energy phenomena. For these processes, one must understand the detector response to gammas, electrons, muons, and hadrons in the energy range of several hundred MeV to a few GeV.

The detector response to higher–energy gammas and electrons can be extrapolated by simulation from data on sources and Michel electrons at energies below 50 MeV and measurements of PMT linearity with the light flasher system. Cosmic-ray muons passing through the detector provide data for reliably calibrating the detector response to muons up to energies of 1–2 GeV. For high energy hadrons, we will have to rely upon detector simulation and, if necessary, beam tests of prototypes.

5.9 High Sensitivity Radio-assay

The contribution of radioactivity to the Kamland detector background should be kept to a minimum in order to limit the uncorrelated background to the first stage of physics and to preserve the option of extending the experiment into the domain of ultra low background measurements. From the point of view of radio-purity most of the materials in the detector fall into two categories: on one side the massive shield of 2.5 m of oil and at least 0.5 m of water allow for relatively relaxed purity requirements on the photomultipliers, sphere, cabling, rocks and, in general, construction elements. At the same time the internal radioactivity of the scintillator, and, to a lesser extent

of the balloon and buffer liquid, has to be extremely low, especially if the detection of single low energy depositions is sought. For instance, as discussed elsewhere in this Proposal, we need to keep U and Th concentrations in steel below 1 ppb, while pushing, in the long run, the U and Th contamination in the scintillator at or below the 10^{-16} g/g level.

In the following we will discuss separately the facilities we envisage for the qualification of the external components and the plans we have to extend our trace analysis sensitivity to the extreme level required.

5.9.1 External Materials

External detector components will be measured in an existing low background Ge detector equipped with a passive lead-copper shield and an active cosmic ray veto system. Such detector, used until recently in material testing for the Palo Verde Reactor Neutrino Oscillation Experiment is currently installed in our laboratories at Caltech. The detector is a high purity p-type Ge detector with 29% relative efficiency and energy resolution FWHM=1.9 keV at 1332 keV. Its cryostat system has been custom build from selected low activity, thin materials in order to allow for low background measurements even at low energy. To reduce the ^{60}Co activity near the Ge crystal all screws are built from pre-World-War-I steel. A radon purging system, essentially to achieve the best sensitivity, is also built into the system. The background spectrum for the counter is shown in Figure 41. The background is dominated by cosmogenic activities and would be improved by installing the detector under some substantial cosmic-ray shielding. For this reason we are soon planning to move the detector to the Palo Verde underground laboratory where the 32 m.w.e. overburden will eliminate the hadronic component of the cosmic radiation and reduce the muon flux to $22\mu\mathrm{m}^{-2}\mathrm{s}^{-1}$.

The counting efficiency for different sample sizes and geometries are readily derived with a Geant-based full simulation of the setup. As an example we estimate the sensitivity of the detector to U and Th to be 2 mBq/kg or, respectively, 0.2 ppb and 0.5 ppb. At the time of writing (Jul 1998) a number of samples including glass, steel, cables and PPO are already being measured.

5.9.2 Internal Materials

The liquid scintillator and all materials close need to be surveyed to extremely tight activity limits. While the tolerable U and Th concentrations of 10^{-14} g/g are already difficult to test, levels near $< 10^{-16}$ g/g, required for the second phase of the experiment are at the limit of todays the sensitivity. While a simple calculation shows that γ spectroscopy is not a viable option, mass spectroscopy and neutron activation techniques offer interesting prospects, with the caveat that both techniques only probe the long-lived parents of the decay series, hence assuming radioactive equilibrium in the entire decay chains.

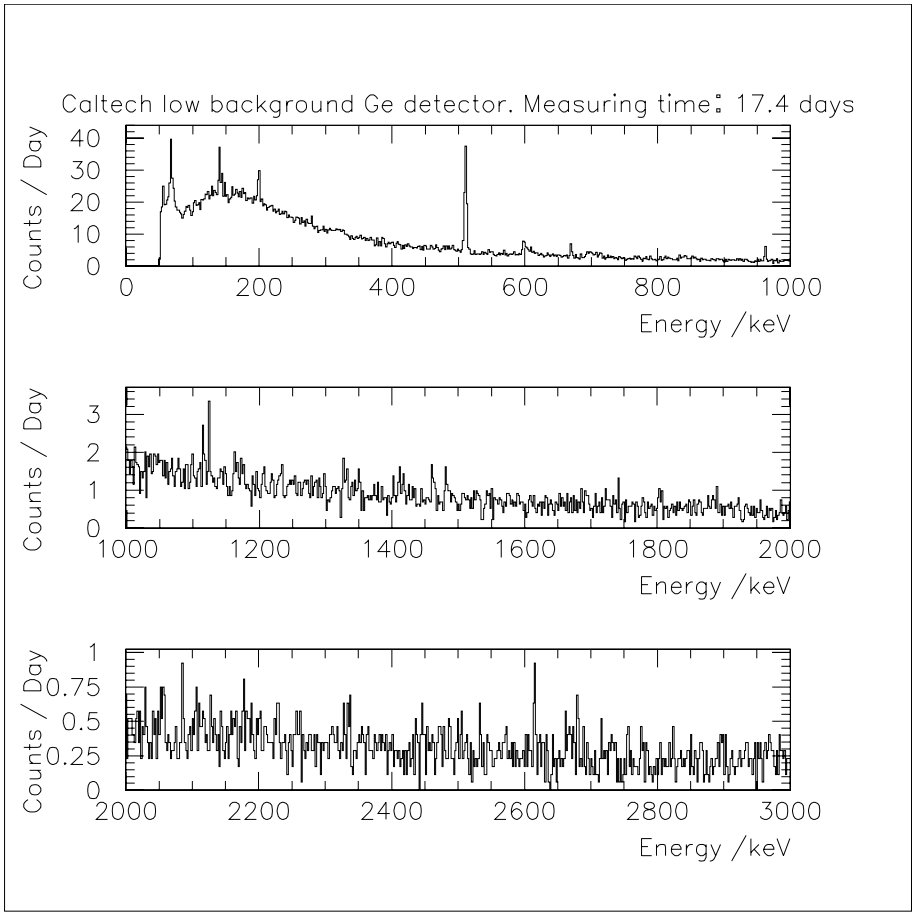

Figure 41: Background spectrum of our low activity Ge detector measured during 17.4 days. The energy range of the naturally occurring γ radiation is shown.

The first technique has been greatly refined for the study of geophysical sciences. In particular a group at Caltech reported[93] measurements of the ^{232}Th content of sea water (in 1 to 10 l samples) down to concentrations of 10^{-14} g/g with a background of 4×10^{-15} g/g (distilled water blank, the filament blank being 1/4 of this value) by means of Thermal Ionization Mass Spectrometry (TIMS). Using the same method this group reports[94] a U blank of 3×10^{-15} g/g for their mass spectrometer. To reduce the sample size the U/Th is precipitated quantitatively by using a small amount of Fe hydroxide. As this method is based on U/Th being in aqueous solution we would need to develop a method to quantitatively extract U/Th from an organic solvent into water in order to use it for the KamLAND experiment. This should be feasible by water extraction as U/Th generally have a higher solubility in polar solvents than in organic solvents. We are presently studying the methods to be used to calibrate the extraction efficiency. Careful choice of the chemicals used is needed to make sure that a measured value is in fact not due to a cross contamination. We are discussing this project with G.J. Wasserburg of Caltech and are exploring a possible cooperation in this field.

The BOREXINO collaboration has developed a very sensitive Neutron Activation Analysis (NAA)[95] for meta stable isotopes. In this technique the sample is irradiated in a high flux reactor, producing unstable isotopes from the nuclei in the impurities. The products of activation of ^{238}U, ^{232}Th and ^{40}K have short lifetimes and decay into ^{239}Np ($T_{1/2}$=2.4 d), ^{233}Pa ($T_{1/2}$=27.0 d) and ^{42}K ($T_{1/2}$=12.4 h) that are then dissolved in liquid scintillator. A $\beta-\gamma$ coincidence set-up, using a low background Ge detector, helps to selectively count the isotopes wanted with virtually no background. As none of the products of activation occurs naturally the purity requirements for the chemicals used in the sample preparation can be substantially relaxed compared to a TIMS analysis. Clean room handling and high purity vessels are however needed before and during the irradiation.

Although organic substances are well suited for NAA as the matrix doesn't produce long lived isotopes which could interfere with the analysis, the irradiation of these substances in a reactor is technically rather challenging as one has to deal with substantial pressure build-up due to radiolysis of the sample.

We are planning to start immediately an R&D program on these techniques in order to be able to develop the expertise needed to address the requirements for a very low background experiment.

6 Schedule

The construction of the KamLAND experiment is facilitated by the little work needed in civil engineering and by the fact that the technology used for the detector is in large part available. Since, as explained in detail above, the background requirements for the first round of physics topics are well within the present technology and even for single counting backgrounds are dominated by radon migration and radioactivity internal to the scintillator, we can immediately build a useful experiment, with a straightforward upgrade path towards possible new physics requiring ultra-low backgrounds. While reasonable steps will have to be taken to guarantee that construction materials will not impede future physics, the requirements are relatively simple and allow for a rapid construction of the detector.

Activity	Duration	Ready
Access Tunnel Enlargement	2 mo	Aug 4, 1998
Disassemble of Kamiokande steel tank	2 mo	Oct 1, 1998
Paint rock and prepare KamLAND pool	2 mo	Dec 8, 1998
Install electrical lines and permanent lighting	2 mo	Mar 1, 1999
Dome radon barrier coating	1 mo	Apr 1, 1999
Build Sphere	7 mo	Nov 8, 1999
Installation of PMT support structure	2 mo	Dec 8, 1999
PMT production	12 mo	Jul 1999
PMT installation	2 mo	Dec 12, 1999
Electronics hut	3 mo	Mar 1. 2000
Purification systems (Water, Buffer and Scint.)	6 mo	Mar 1, 2000
Veto installation	5 mo	Mar 1, 2000
Electronics production/installation/commissioning	12 mo	Jul 7, 2000
Balloon installation	1 mo	Aug 7, 2000
Scintillator/buffer filling	4 mo	Dec 6, 2000
Data taking begins	–	Jan 2001

Table 13: Simplified construction and commissioning schedule for KamLAND.

At the time of writing (July 1998) the Kamiokande detector has been emptied, PMTs dismounted and the access tunnel connecting KamLAND to the SuperKamiokande access road is being enlarged. We expect to have permanent electricity and lights in the cavern by Mar 1999, to start the construction of the large stainless sphere vessel. Scintillator will be filled in the second half of year 2000 and data-taking is expected to begin in January 2001.

A simplified list of milestones for construction and commissioning is given in Table 13.

7 Appendix: Selected Isotopes Decay Chains

^{238}U (4.5×10^9 y)	E_α	E_γ	per ^{238} U decays
|	4198	-	0.790
↓	4151	50	0.210
^{234}Th (24.1 d)	E_{β^-} Endpoint	E_γ	per ^{238} U decays
|	273	-	0.703
|	160	113	0.022
|	181	92	0.192
↓	136	137	0.083 *
^{234}Pa (1.2 m)	E_{β^-} Endpoint	E_γ	per ^{238} U decays
|	2197	-	0.982
|	1153	1001,43	0.009
↓	1099	1098	0.009 *
^{234}U (2.5×10^5 y)	E_α	E_γ	per ^{238} U decays
|	4775	-	0.714
↓	4722	53	0.286
^{230}Th (7.5×10^4 y)	E_α	E_γ	per ^{238} U decays
|	4688	-	0.763
↓	4621	68	0.237
^{226}Ra (1600 y)	E_α	E_γ	per ^{238} U decays
|	4784	-	0.944
↓	4602	186	0.056
^{222}Rn (3.8 d)	E_α	E_γ	per ^{238} U decays
↓	5490	-	1.000
^{218}Po (3.1 m)	E_α	E_γ	per ^{238} U decays
↓	6002	-	1.000
^{214}Pb (26.8 m)	E_{β^-} Endpoint	E_γ	per ^{238} U decays
|	1023	-	0.093
|	184	839	0.006
|	234	786,53	0.009
|	671	352	0.460
|	728	295	0.288
|	728	242,53	0.117
↓	511	512	0.027 *

^{214}Bi (19.9 m)	E_{β^-} Endpoint	E_γ	per ^{238} U decays
|	3272	-	0.199
|	790	1208,665,609	0.005
|	824	2448	0.015
|	824	1838,609	0.004
|	1068	2204	0.048
|	1153	1509,609	0.022
|	1153	2119	0.012
|	1255	1408,609	0.029
|	1261	1402,609	0.015
|	1278	1385,609	0.009
|	1382	1281,609	0.015
|	1425	1847	0.021
|	1425	1238,609	0.059
|	1508	1764	0.149
|	1508	1155,609	0.016
|	1542	1120,609	0.144
|	1542	1730	0.028
|	1729	934,609	0.027
|	1857	806,609	0.009
|	1894	1378	0.032
|	1894	768,609	0.040
↓	1636	1636	0.102*
^{214}Po (164 μs)	E_α	E_γ	per ^{238} U decays
|	6902	800	0.0001
↓	7687	-	0.9999
^{210}Pb (22 y)	E_{β^-} Endpoint	E_γ	per ^{238} U decays
|	64	-	0.160
↓	17	47	0.840
^{210}Bi (5.0 d)	E_{β^-} Endpoint	E_γ	per ^{238} U decays
↓	1163	-	1.000
^{210}Po (138 d)	E_α	E_γ	per ^{238} U decays
↓	5304	-	1.000
^{206}Pb (∞)			

Table 14: ^{238}U decays chain. Only decays with visible energy larger than 100 keV or branching ratio more than 0.5% are listed. Effects of internal conversion are not included as they have negligible effects on our calculations for a very large detector.

^{232}Th (1.4×10^{10} y)	E_α	E_γ	per ^{232} Th decays
|	4013	-	0.779
↓	3954	64	0.221
^{228}Ra (5.8 y)	E_{β^-} Endpoint	E_γ	per ^{232} Th decays
↓	46	-	1.000
^{228}Ac (6.1 h)	E_{β^-} Endpoint	E_γ	per ^{232} Th decays
|	2069	58	0.100
|	403	755, 911, 58	0.007
|	438	1631, 58	0.020
|	438	1502, 129, 58	0.006
|	444	1496, 129, 58	0.009
|	481	1588,58	0.031
|	481	1459, 129, 58	0.008
|	596	99, 463,911,58	0.015
|	596	99,463,969	0.011
|	596	99,409,965,58	0.008
|	596	563,911,58	0.016
|	596	563,969	0.009
|	596	509,965,58	0.010
|	959	772,338,58	0.012
|	959	840,270,58	0.005
|	973	322,774,58	0.005
|	973	322,503,328	0.005
|	973	322,503,270,58	0.006
|	973	1096,58	0.009
|	973	1154	0.010
|	1004	795,328	0.020
|	1004	795, 270,58	0.023
|	1104	965, 58	0.023
|	1104	836,128,58	0.007
|	1158	969	0.116
|	1216	911	0.191
|	1731	209,129,58	0.030
|	1731	338,58	0.086
↓	1063	1064	0.202 *

^{228}Th (1.9 y)	E_α	E_γ	per ^{232} Th decays
|	5423	-	0.715
↓	5340	84	0.285
^{224}Ra (3.7 d)	E_α	E_γ	per ^{232} Th decays
|	5685	-	0.949
↓	5449	241	0.051
^{220}Rn (56 s)	E_α	E_γ	per ^{232} Th decays
↓	6288	-	1.000
^{216}Po (0.145 s)	E_α	E_γ	per ^{232} Th decays
↓	6778	-	1.000
^{212}Pb (11 h)	E_{β^-} Endpoint	E_γ	per ^{232} Th decays
|	574	-	0.123
|	274	300	0.052
↓	335	239	0.825
^{212}Bi (61 m)	E_{β^-} Endpoint	E_γ	per ^{232} Th decays
|	2254	-	0.555
| 64%	634	1620	0.015
|	742	785,727	0.011
|	1527	727	0.044
↓	1127	1127	0.015*
^{212}Po (299 ns)	E_α	E_γ	per ^{232} Th decays
↓	8784	-	0.640
^{208}Pb (∞)			
^{212}Bi (61 m)	E_α	E_γ	per ^{232} Th decays
| 36%	6090	-	0.098
↓	6050	40	0.262
^{208}Tl (3.1 m)	E_{β^-} Endpoint	E_γ	per ^{232} Th decays
|	1040	763,583,2615	0.008
|	1292	511,583,2615	0.085
|	1525	861,2615	0.052
|	1525	277, 583, 2615	0.026
|	1803	583,2615	0.175
↓	2500	2501	0.014 *
^{208}Pb (∞)			

Table 15: ^{232}Th decays chain. Only decays with visible energy larger than 100 keV or branching ratio more than 0.5% are listed. Effects of internal conversion are not included as they have negligible effects on our calculations for a very large detector.

^{40}K (1.3×10^9 y)	E_{β^-} Endpoint	E_γ	per ^{40} K decays
$\downarrow$ 89.3%	1311	-	0.893
^{40}Ca (∞)			
^{40}K (1.3×10^9 y)		E_γ	per ^{40} K decays
$\vert$ 10.7%		1461	0.105
$\downarrow$		-	0.002
^{40}Ar (∞)			

Table 16: ^{40}K decays chain. Decays with visible energy less than 100 keV or branching ratio more than 0.5% are listed.

^{60}Co (5.3 y)	E_{β^-} Endpoint	E_γ	per ^{60} Co decays
$\downarrow$	318	1173, 1333	1.000
^{60}Ni (∞)			

Table 17: ^{60}Co decays chain. Decays with visible energy less than 100 keV or branching ratio more than 0.5% are listed.

References

[1] L. Wolfenstein, Phys. Rev. D 17 (1978) 2369; S.P. Mikheyev and A.Yu. Smirnov, Sov. J. Nucl. Phys. 42 (1985) 1441.

[2] B. Pontecorvo, Zh. Eksp. Theor. Fiz. 33 (1957) 549; 34 (1958) 247.

[3] K. Hoepfner *et al.* Nucl. Phys. Proc. Suppl. 65 (1998) 171.

[4] E. Pennacchio *et al.* Nucl. Phys. Proc. Suppl. 65 (1998) 177.

[5] J. Kleinfeller *et al.* (Karmen Collaboration) in Proceedings of "Neutrino 96", Helsinki, Finland, World Scientific June 1996, p. 193.

[6] C. Athanassopoulos *et al.* NIM A 388 (1997) 149.

[7] C. Athanassopoulos *et al.* e-print Archive nucl-ex/9709006, Submitted to Phys. Rev. Lett. (1997)

[8] E. Church *et al.* "A proposal for an experiment to measure $\nu_\mu - \nu_e$ oscillations at the Fermilab booster: BOONE" FERMILAB-P-0898, Dec 1997.

[9] E. do Couto e Silva *et al.* CERN-EP-98-081 (May 1998).

[10] M. Apollonio *et al.* Phys. Lett. B 420 (1998) 397.

[11] F. Boehm *et al.* (Palo Verde Collaboration) in Proceedings of "Neutrino 96", Helsinki, Finland, World Scientific June 1996, p. 248.

[12] E. Ables *et al.* (MINOS Collaboration) "A long-baseline ν oscillation experiment at Fermilab", FERMILAB-P-875, Feb 1995.

[13] Y. Oyama *et al.* (K2K Collaboration) KEK-Preprint 97-266 (Jan 1998).

[14] K. Schreckenbach *et al.*, Phys. Lett. B99 (1981) 251; B160 (1985) 325; F. von Feilitzsch *et al.*, Phys. Lett. B118 (1982) 162; A. A. Hahn *et al.*, Phys. Lett. B218 (1989) 365.

[15] See for example Y. Declais *et al.* Phys. Lett. B 338 (1998) 383, G. Zacek *et al.* Phys. Rev. D 34 (1986) 2621.

[16] G. Zacek *et al.* Phys. Rev. D 34 (1986) 2621.

[17] The Federation of Electric Power Companies, Japan, "Status of Electric Power Industry 1996-97", in Japanese.

[18] G. Eders, Nucl. Phys., 78 (1966) 657.

[19] G. Marx, Czech. J. of Physics B, 19 (1969) 1471;
G. Marx and I. Lux, Acta Phys. Acad. Hung., 28 (1970) 63;
C. Avilez *et al.*, Phys. Rev. D23 (1981) 1116.

[20] L. Krauss *et al.*, Nature 310 (1984) 191.

[21] J.S. Kargel and J.S. Lewis, Icarus 105 (1993) 1.

[22] R.S. Raghavan *et al.*, Phys. Rev. Lett. 80 (1998) 635.

[23] C.G. Rothschild, M.C. Chen, F.P. Calaprice, Submitted to Geophys. Rev. Lett.

[24] Borexino at Gran Sasso, ed. G. Bellini *et al.* INFN Milano 1992,
R.S. Raghavan, Science 267 (1995) 45.

[25] P. Vogel, Phys. Rev. D29 (1984) 1918.

[26] Review of Particle Properties, Phys. Rev. D54 (1996)

[27] H.A. Bethe, Rev. Mod. Phys. 62 (1990) 801.

[28] H.T. Janka *et al.* Astrophys. J. 433 (1994) 229.

[29] J. Engel, E. Kolbe, K. Langanke, and P. Vogel, Phys. Rev. C **54**, 2740 (1996).

[30] C. Athanassouploulos et al., Phys. Rev. C **56**, 2806 (1997).

[31] B. Zetnitz, Prog. Part. Nucl. Phys. **32**, 351 (1994).

[32] Y.-Z. Qian et al., Phys. Rev. Lett. **71**, 1965 (1993).

[33] A. Antonioli et al. , Nuovo Cim. C **14**, 631 (1991).

[34] E.Kh. Akhmendov, Sov. Phys. JETP 68 (1989) 690;
H. Minakata and H. Nunokawa, Phys. Rev. Lett. 63 (1989) 121;
C.S. Lim and W.J. Marciano, Phys. Rev. D37 (1988) 1368;
E.Kh. Akhmendov, Phys. Lett. B257 (1991) 163;
E.Kh. Akhmendov, 4th International Solar Neutrino Conference, Heidelberg, Germany, Apr 1997.

[35] J.N. Bahcall, N. Cabibbo and A. Yahill, Phys. Rev. Lett. 28 (1972) 316;
J.N. Bachall *et al.*, Phys. Lett. B181 (1986) 396;
Z. Berezhiani *et al.*, Z. Phys. C54 (1992) 351 and JETP Lett. 55 (1992) 151;
Z. Berezhiani, M. Moretti and A. Rossi, Z. Phys. C58 (1993) 423.

[36] M.B. Voloshin, M.I. Vysotskii and L.B. Okun, Soviet J. Nucl. Phys. 44 (1986) 440;
P.A. Sturrock, G. Walter and M.S. Wheatland, Ap. J. 491 (1997) 409.

[37] G. Fiorentini, M. Moretti, F.L. Villante, Phys. Lett. B413 (1997) 378.

[38] Y. Fukuda *et al.* e-print Archive hep-ex/9805021, May 1998.

[39] G.V.Domogatskii Sov.Astron. 28, 30 (1984) 30.

[40] T. Totani *et al.* in proceedings of the 17^th International Conference on Neutrino Physics and Astrophysics, Helsinki, Finland 1996; World Scientific.

[41] M. Ambrosio *et al.* Phys. Lett. B 406 (1997) 249.

[42] Y.Totsuka, *in the Proceedings of the 7th Workshop on Grand Unification/ICOBAN '86*, edited by J.Arafune (World Scientific, Singapore, 1986), p. 118.

[43] H. Ejiri, *Phys. Rev.* **C48** (1993) 1442.

[44] Yu. Kamyshkov, *in the Proceedings of the First International Conference on Particle Physics Beyond the Standard Model*, Castle Ringberg, Germany, June 1997; Editor H.V. Klapdor-Kleingrothous, IOP Publishing Co., 1997, p. 542.

[45] C. Berger *et al.*, Phys. Lett. B269 (1991) 227.

[46] Y.Fukuda et al., Super-Kamiokande Collaboration, Talk presented by T.Kajita at Neutrino-98 Conference, Takayama, June 1998.

[47] M. Nakahata *et al.*, Jour. of Jap. Phys. Soc. 55 (1986) 3786.

[48] M. Aglietta et al. Nuovo Cimento **C12**,467(1989).

[49] R. Hertenberger, M. Chen, and B. L. Dougherty, Phys. Rev. **C52**, 3449 (1995).

[50] J. Delorme, M. Ericson, T. Ericson, and P. Vogel, Phys. Rev. **C52**, 2222 (1995).

[51] E. A. Petterson, Neutrino-96, p.223, World Scientific, Singapore, 1997.

[52] J.N. Bahcall and M.H. Pinsonneault, Rev. Mod. Phys. **67**, 781 (1995).

[53] M. Fukugita and A. Suzuki, "Physics and Astrophysics of Neutrinos", Springer Verlag, 1994.

[54] L. Baudis et al., Phys. Lett. B 407 (1997) 219

[55] A. Staudt, K. Muto and H.V. Klapdor-Kleingrothaus, Euro. Phys. Lett. 13 (1990) 31

[56] R.S. Raghavan, Phys. Rev. Lett. 72 (1994) 1411

[57] H. Stephen and T. Stephen, Solubilities of Inorganic and Organic Compounds, (1963) 586

[58] F. Boehm, private communication, (1998)

[59] H.V. Klapdor-Kleingrothaus, Contribution to Neutrino 98, Takayama, Japan, Jun 98.

[60] O. Cremonesi, Contribution to Neutrino 98, Takayama, Japan, Jun 98.

[61] R. Brun et al., "GEANT 3", CERN DD/EE/84-1 (revised), 1987.

[62] P.A. Aarnio et al., "FLUKA user's guide", TIS-RP-190, CERN, 1990

[63] T.A. Gabriel et al., ORNL/TM-5619-mc, April 1977.

[64] F.F. Khalchukov*et al.*, Nuovo Cimento, 6C (1983) 320.

[65] K.V. Alanakyan*et al.*, Sov. J. Nucl. Phy. 34 (1981) 828.

[66] Bugaev *et al.*, Sov. J. Nucl. Phy. 41 (1985) 245.

[67] L. Oberauer, Private communication, scaled from the yield measured in a CERN test beam.

[68] K. Nakamura *et al.* in "Physics and Astrophysics of Neutrinos" M. Fukugita, A. Suzuki eds., Springer-Verlag, Tokyo 1996.

[69] J. Cugnon *et al.* Nucl. Phys. A 625 (1997) 729; A. Ferrari *et al.* Z. Phys. C 70 (1996) 413, Z. Phys. C 71 (1996) 75.

[70] G. Alimonti *et al.* Phys. Lett. B 422 (1998) 349.

[71] W.R. Webber *et. al*, Phys. Rev. C 41(1990)547.

[72] V. McLane *et. al*, "Neutron Cross Sections", Vol.2, Academic Press, Inc. 1988.

[73] N.C. Mukhopadhyay *et. al*, e-Print Archive Nucl-th/9802060, submitted to Phys. Lett. B.

[74] G.L. Cassiday *et al.*, Phys. Rev. D 7 (1973) 2022.

[75] R.B. Firestone, V.S. Shirley *et al.* "Table of Isotopes" Eighth Edition, Wiley Interscience 1996.

[76] SuperKamiokande Collaboration, Private Communication.

[77] J.B. Birks, "The Theory and Practice of Scintillation Counting", McMillan, New York, 1964; J.B. Birks, "Photophysics of Aromatic Molecules", Wiley and Sons, London, 1970.

[78] J. B. Benziger, *et al.*, "A Scintillator Purification System for a Large Scale Solar Neutrino Experiment", submitted to NIM; J. B. Benziger, *et al.*, "A Large Scale Low Background Liquid Scintillation Detector: The Counting Test Facility at Gran Sasso", submitted to NIM; G. Bellini *et al.*, Nucl. Phys. Proc. Suppl. 48 (1996) 363.

[79] J. Shirai, "Purification System", KamLAND-NOTE-97-06.

[80] G. Bellini *et al.*, Nucl. Phys. Proc. Suppl. 48 (1996) 363.

[81] See section 4.2 of G. Bellini *et al.*, Nucl. Phys. Proc. Suppl. 48 (1996) 363.

[82] R.S. Raghavan, "LENS", Talk at Neutrino 98, Takayama, Japan, June 1998.

[83] P. Alivisatos, Science 271 (1996) 933.

[84] see http://www.national.com

[85] T. Kajita et al., Super-Kamiokande Collaboration, *in the Proceedings of the XVIII-th International Conference on Neutrino Physics and Astrophysics, NEUTRINO-98*, June 4-9, Takayama, Japan.

[86] A.L. Wintenberg, et al., "Monolithic Circuits for the WA98 Lead Glass Calorimeter", in Proceedings of NSS 94; M.L. Simpson, et al., "An Integrated CMOS Time Interval Measurement System with Sub-nanosecond Resolution for the WA-98 Calorimeter", *IEEE Journal of Solid-State Circuits*, vol. 32, No. 2, 1997, pp 198-205; A.L. Wintenberg, et al., "A CMOS Integrating Amplifier for the PHENIX Ring Imaging Čerenkov Detector", in Proceedings of NSS 97; A.L. Wintenberg, et al., "The RICH Chip - A CMOS Integrated Circuit for the PHENIX Ring Imaging Čerenkov Detector", to be published in the *IEEE Transactions on Nuclear Science*.

[87] C.L. Britton, et al., "An Analog Random Access Memory in the AVLSI-RA Process for an Interpolating Pad Chamber", IEEE Transactions on Nuclear Science, vol. 42, No 6, Dec. 1995

[88] G. Gratta *et al.*, NIM A 400 (1997) 456.

[89] Karmen Collaboration, Private Communication.

[90] P. Anselmann *et al.* Phys. Lett. B 342 (1995) 440.

[91] J. Abdurashitov *et al.* Phys. Rev. Lett. 77 (1996) 4708.

[92] L. Mikaelyan and I. Machulin, "Artificial Anti-neutrino Sources for Anti-neutrino Detectors of the Next Generation," GNPI Preprint 50:05–17/9.

[93] M. Roy-Barman, J.H. Chen and G.J. Wasserburg, Earth and Planetary Science Letters 139 (1996) 351

[94] P.S. Andersson et al., Earth and Planetary Science Letters 130 (1995) 217

[95] T. Goldbrunner et al., Nucl. Phys. B 61B (1998) 176